To the graduate Council:

I am submitting herewith a thesis written by Brett Randall Starr entitled "Development of Finite Element Model for Approximating Composite Structures Crushing Characteristics." I have examined the final copy of this thesis for form and content and recommend that it be accepted in partial fulfillment of the requirements for the degree of Master of Science, with a major in Engineering Science.

R. Engels

Remi Engels, Major Professor

We have read this thesis and
recommend its acceptance:

John E. Carothers

Roy J. Schulz

Accepted for the Council:

Associate Vice Chancellor and Dean of
The Graduate School

Development of Finite Element Model for Approximating Composite Structures Crushing Characteristics

A Thesis
Presented for the
Master of Science
Degree
The University of Tennessee, Knoxville

Brett Randall Starr
May 1999

Acknowledgments

I would like to thank Lisa E. Jones of NASA Langley's Impact Dynamics Research Facility for making this research project possible and for providing me the opportunity to conduct research at NASA Langley. Lisa was instrumental in selecting me for an internship at Langley research center and provided the computer and test resources necessary to complete the project. I would also like to thank all the Impact Dynamics Research Facility staff for their support and the excellent work environment they provided with their friendliness and willingness to mentor. Special thanks to Ed Fasanella for his continued guidance after returning to campus through prompt email responses and to Rick Martin for his preparation of test coupons and help in conducting testing.

I would like to thank Dr. Remi Engels, major advisor, for the guidance given throughout my studies at UTSI, for his patience in teaching me new concepts and for the encouragement given while mastering difficult subject matter.

Most importantly I would like to thank my wife Melissa for enthusiastically supporting my decision to return to school to complete a Master's degree and for patently enduring the financial and emotion stresses of undertaking such a project. Melissa provided invaluable encouragement and companionship upon returning to school and faithfully endured a summer's separation while conducting the NASA internship for which I am especially grateful.

Abstract

A finite element model of a composite keel beam web was developed to approximate its crushing behavior and to provide estimates of its energy absorption characteristics. The model development was done as part of NASA Langley Impact Dynamics Research Facility development of an energy absorptive composite keel beam for use in general aviation aircraft subfloors intended to increase occupant survivability in crash impacts with vertical sink rates up to 30 $^{ft}/_{s2}$. The finite element model was developed by modeling the impact test of a block core keel beam web specimen referred to as B1.4 [8] and establishing correlation with energy absorption parameters measured during testing. SDRC Ideas® Master Series was used to generate the specimen geometry and finite element mesh. MSC/Dytran™was used to define the test kinematics and dynamics, the specimen material constitutive relationships and failure criteria and to solve the model. Initially the glass fabric/epoxy and kevlar fabric/epoxy material wrapping the foam core was modeled as an orthotropic laminate and assigned a Tsai-Wu failure criteria. The foam was modeled as crushable material with a stress-strain and failure relationship defined by the foam stress-strain curve. The impact dynamics was modeled as a free fall onto a rigidly supported specimen. This specimen/test representation resulted in premature failure of the laminate and collapse of the specimen model. The premature failure was due to unrealistically high accelerations and impact forces being generated by the free fall impact. The free fall

impact was eliminated and the impact acceleration was defined to be that of the actual acceleration pulse generated in the test. With this representation the model's crushing behavior similar to that of the test. However the energy absorption parameter magnitudes were low. The model crush initiation load was 2.8 kLb (12.5 kN) and its sustained crush load was .25 kLb (1.1 kN) which were 63.7% and 91.9% below recorded test values respectively. The low magnitudes were a result of the orthotropic constitutive relationship not representing the material nonlinear shear stress-shear strain behavior and the brittle failure mode of the Tsai-Wu failure criteria. A constitutive relationship and failure criteria that better approximates the glass fabric/epoxy and kevlar fabric/epoxy material are needed to improve the model's estimation of energy absorptive parameters. An approximation of these materials behavior was made by representing them as a laminate of isotropic elastic-plastic lamina with strain based failure criteria. With this representation the model crush initiation load was 6.7 kLb (30.0 kN) and its sustained crush load was 3.1 kLb (13.8 kN) which are within 5% and 1.5% of recorded test values respectively. Thus the model closely approximates the specimen crushing behavior and its energy absorptive parameters for the defined impact acceleration when constitutive/failure relationships similar to the material are used.

Table of Contents

Chapter		Page
1	Introduction	1
1.1	Background	1
1.2	Problem Statement	6
1.3	Approach	7
2	Theory	9
2.1	Equations of Motion	10
2.2	Finite Element Representation of Equation of Motion	14
2.3	Element Formulations	17
2.4	Constitutive Relationships	30
2.5	Solution Technique	37
3	Finite Element Model	40
3.1	Impact Test Simulated	40
3.2	Test Specimen Description	42
3.3	Modeling Technique	43
3.4	Model Kinematics	45
3.5	Model Dynamics	53

4 Material Properties 55

4.1 Standard Property Values 55

4.2 Material Property Testing 56

5 Model Solution, Results, Correlation and Modification 64

5.1 Model Solution 64

5.2 Model Results 65

5.3 Model Correlation 68

5.4 Model Modifications 68

6 Conclusions 79

References 83

Appendices 85

A 86

B 106

Vita 178

List of Tables

Table		Page
3.1	Box core specimen EA parameters	87
3.2	Block core specimen EA parameters	88
4.1	Isotropic Material Elastic Properties, Imperial	89
4.2	Orthotropic Material Elastic Properties, Imperial	89
4.3	Isotropic Strength Properties, Imperial	89
4.4	Orthotropic Strength Properties, Imperial	89
4.5	Isotropic Material Elastic Properties, mm/tonne/sec	90
4.6	Orthotropic Material Elastic Properties, mm/tonne/sec	90
4.7	Isotropic Strength Properties, mm/tonne/sec	90
4.8	Orthotropic Strength Properties, mm/tonne/sec	90
4.9	Glass/Epoxy Sheet 1 Coupon Measurements	91
4.10	Glass/Epoxy Sheet 2 Coupon Measurements	92
4.11	Kevlar/Epoxy Sheet 1 Coupon Measurements	93
4.12	Kevlar/Epoxy Sheet 2 Coupon Measurements	94
4.13	Glass/Epoxy Sheet 1 Longitudinal Properties	95
4.14	Glass/Epoxy Sheet 1 Transverse Properties	95
4.15	Glass/Epoxy Sheet 1 Shear Properties	96
4.16	Glass/Epoxy Sheet 2 Longitudinal Properties	97

4.17 Glass/Epoxy Sheet 2 Transverse Properties 97

4.18 Glass/Epoxy Sheet 2 Shear Properties 98

4.19 Kevlar/Epoxy Sheet 1 Longitudinal Properties 99

4.20 Kevlar/Epoxy Sheet 1 Transverse Properties 99

4.21 Kevlar/Epoxy Sheet 1 Shear Properties 100

4.22 Kevlar/Epoxy Sheet 2 Longitudinal Properties 101

4.23 Kevlar/Epoxy Sheet 2 Transverse Properties 101

4.24 Kevlar/Epoxy Sheet 2 Shear Properties 102

4.25 Fabric Lamina Averaged Elastic Properties, Imperial 103

4.26 Fabric Lamina Averaged Strength Properties, Imperial 103

4.27 Fabric Lamina Averaged Elastic Properties, mm/tonne/sec 104

4.28 Fabric Lamina Averaged Strength Properties 104

5.1 Time-Velocity Data Points Defining Support Platen Time History 105

List of Figures

Figure		Page
1.1	Subfloor attachment to fuselage	107
1.2	IDRF Full scale aircraft test fixture	108
1.3	Graphical depiction of EA parameters	109
1.4	Graphical representation of crush efficiency	109
1.5	Rectangular composite beam construction	110
2.1	Arbitrary volume subjected to surface tensions, body force and inertia force.	111
2.2	Simplified representation of finite element process	112
2.3	Isoparametric brick element	113
2.4	Linear variation of shape function	113
2.5	Relative motion of two particles	114
2.6	Co-rotational and element coordinate systems	115
2.7	Isotropic elastic-plastic yield surface	116
2.8	Crushable foam stress-strain curve	116
2.9	Crushable foam unloading stress-strain curve	117
2.10	Solution process flow chart	117
3.1	Crush fixture	118
3.2	Model representation of specimen and crush fixture	119

Figure **Page**

3.3 Knife edge cuts made into specimen 120

3.4 Refined master surface mesh penetration into coarse slave mesh 121

3.5 Slave node missing knife edge 122

3.6 Single surface contact surface 123

3.7 Inversion of solid element 124

3.8 Intermittent penetration of knife edge contact surface 125

4.1 PVC foam compressive stress-strain curve 126

4.2 PVC foam Poisson's ratio versus strain 127

4.3 Glass/epoxy sheet 1 coupon layout 128

4.4 Glass/epoxy sheet 2 coupon layout 129

4.5 Kevlar/epoxy sheet 1 coupon layout 130

4.6 Kevlar/epoxy sheet 2 coupon layout 131

4.7 Coupon measurement points 132

4.8 Tinius-Olsen coupon pull fixture 133

4.9 NEF 122 strain gage amplifiers 134

4.10 LabView™ data acquisition on MacIntosh P. C. 135

4.11 LabView™ graphical interface 136

4.12 Glass/epoxy sheet 2 failed longitudinal coupons 137

4.13 Glass/epoxy sheet 1 failed transverse coupons 138

Figure **Page**

4.14 Glass/epoxy sheet 2 failed shear coupons 139

4.15 Kevlar/epoxy sheet 1 failed longitudinal coupons 140

4.16 Kevlar/epoxy sheet 1 failed traverse coupons 141

4.17 Kevlar/epoxy sheet 2 failed shear coupons 142

4.18 Representative glass/epoxy longitudinal stress-strain curve 143

4.19 Representative glass/epoxy transverse stress-strain curve 144

4.20 Representative glass/epoxy shear stress-strain curve 145

4.21 Representative kevlar/epoxy longitudinal stress-strain curve 146

4.22 Representative kevlar/epoxy transverse stress-strain curve 147

4.23 Representative kevlar/epoxy shear stress-strain curve 148

4.24 Glass/epoxy stress-strain curve fit highlighting change in slope 149

5.1 Impact force time history of planar geometry specimen 150

5.2 Kevlar lamina stress distribution at .2 ms for planar geometry specimen 151

5.3 Stress time history of element at support platen interface for planar geometry specimen 152

5.4 Kevlar lamina stress distribution at .5 ms for planar geometry specimen 153

Figure **Page**

5.5 Perturbations in specimen sides 154

5.6 Impact force time history of perturbed geometry specimen 155

5.7 Kevlar lamina stress distribution at .2 ms for perturbed geometry specimen 156

5.8 Kevlar lamina stress distribution at .5 ms for perturbed geometry specimen 157

5.9 Static stress distribution of planar geometry specimen 158

5.10 Static stress distribution of perturbed geometry specimen 159

5.11 Nodal position time history of planar geometry specimen 160

5.12 Nodal position time history of perturbed geometry specimen 161

5.13 Impact mass acceleration time history of planar geometry specimen 162

5.14 Impact mass acceleration time history of perturbed geometry specimen 163

5.15 Test acceleration pulse and its approximation 164

5.16 Velocity profile assigned to support platen 165

5.17 Impact force time history of planar specimen with base acceleration 166

5.18 Kevlar lamina stress distribution at 2.5 ms for planar specimen with base acceleration 167

Figure **Page**

5.19 Stress time history of element at impact mass interface for planar geometry specimen with base acceleration 168

5.20 Kevlar lamina stress distribution at 3 ms for planar geometry specimen with base acceleration 169

5.21 Kevlar lamina stress distribution at 3.5 ms for planar geometry specimen with base acceleration 170

5.22 Stress time history of element in mid-section of planar geometry specimen with base acceleration 171

5.23 Displacement time history of support platen and impact mass of planar geometry specimen with base acceleration 172

5.24 Support platen acceleration time history for base acceleration 173

5.25 Support platen velocity time history for base acceleration 174

5.26 Test specimen crushing pattern 175

5.27 Impact mass acceleration time history for planar geometry with base acceleration 176

5.28 Impact force time history for specimen with elastic-plastic lamina, planar geometry and base acceleration 177

List of Abbreviations

ASTM	American Society for Testing and Materials
CIL	crush initiation load
EA	energy absorption
IDRF	Impact Dynamics Research Facility
MSC	MacNeal-Schwendler Corporation
NASA	National Aeronautics and Space Administration
SCL	sustained crush load
SDRC	Structural Dynamics Research Corporation

List of Symbols

δ_{ij}	Kronecker delta
ϵ	engineering normal strain
ϵ^{p}_{eff}	effective plastic strain
κ	plate shear factor from Mindlin plate theory
ν	Poisson's ratio
ξ	natural coordinate
ρ	material density
σ	stress vector
σ_*	traction vector
σ_i	stress vector component
σ_{ij}	stress tensor
σ_P	principal stress
σ_U	ultimate stress
σ_Y	yield stress
ϕ	constitutive failure function
ω^*	rotation vector of co-rotational coordinate system
Ω_{ij}	spin tensor
$\boldsymbol{a}$	acceleration vector
$\boldsymbol{b}$	body force vector

c	speed of sound in material
C_{ijkl}	material elastic tensor
D^*	element strain rate matrix in co-rotational coordinate system
D_{ij}	rate of deformation tensor
e	small strain vector
E	isotropic material Young's modulus
$\mathbf{e}^*$	co-rotational unit vector
E_1	orthotropic material youngs modulus in longitudinal (fiber) direction
E_2	orthotropic material youngs modulus in transverse direction
E_H	isotropic material hardening modulus
e_{ij}	small strain tensor
E_{ij}	finite strain tensor
E_P	isotropic material plastic modulus
f	Tsai-Wu failure criteria coefficent
f^*	nodal force in co-rotational sytem
F^{res}	residual element force in co-rotational system
J	Jacobian
k	element stiffness matrix
L_{ij}	velocity tensor
m	element mass matrix
m^*	nodal moment in co-rotational system

N	element shape function matrix
n_j	surface normal vector component
q	global generalized coordinate vector
q_e	generalized coordinate vector of element
Q_e	locator matrix for placing element generalized coordinate vector into global generalized coordinate vector
q_i	generalized coordinate vector component
S_{1C}	orthotropic material compressive strength in longitudinal (fiber) direction
S_{1T}	orthotropic material tensile strength in longitudinal (fiber) direction
S_{2C}	orthotropic material compressive strength in transverse direction
S_{2T}	orthotropic material tensile strength in transverse direction
s_{ij}	deviatoric stress tensor
S_U	isotropic material ultimate strength
S_Y	isotropic material yield strength
$\mathbf{u}$	displacement vector
u_i	displacement vector component
v	velocity vector
v^*	velocity in co-rotational coordinate system
v_i	velocity vector component
v_i^{*m}	nodal velocity component in co-rotational coordinate system at element mid-plane

x^* co-rotational coordinate system axis

Π system potential energy

ϖ natural frequency

Π_e elemental potential energy

Chapter 1

Introduction

1.1 Background

This thesis deals with the development of an energy absorbing keel beam for use in general aviation aircraft subfloors that will increase occupant survivability in crashes with vertical sink rates up to 30 ft/s. The work is done in cooperation with NASA Langley Research Center's Impact Dynamics Research Facility.

The crash characteristics of general aviation aircraft differ from those of transport aircraft. In general aviation aircraft there is no collapsible structure such as luggage compartments between the occupant seating and exterior fuselage as there is in transport aircraft. Instead, the subfloor is attached directly to the fuselage as shown in figure B-1.1[1]. In a crash situation, impact accelerations are transmitted into the subfloor and occupant seating without being attenuated by collapse of compartments beneath the seating. Current technology general aviation aircraft utilize a fiber reinforced composite fuselage with an aluminum subfloor. These configurations result in stiff structures that transmit unacceptably large accelerations into occupant seating. Energy absorbing seats have been developed to aid in reducing accelerations imparted to occupants. The seat legs are 'S'

[1] All figures are located in appendix B. All tables are located in appendix A.

shaped and bend under crash loading thereby absorbing energy and reducing impact accelerations. However these seats alone do not provide enough energy absorption. The Impact Dynamics Research Facility (IDRF) is working to increase occupant survivability by developing a composite subfloor keel beam that crushes under crash loads thereby absorbing energy and reducing accelerations/loads imparted to occupants. The goal of the program is to develop a subfloor comprised of composite keel beams that buckle under crash loads and crushes sufficiently to absorb enough energy to reduce occupant lumbar loads below a maximum allowable 1500 lb limit as outlined in Federal Aviation Regulations Part 23 while having enough strength to support flight loads. In addition, the keel beam must retain enough strength after crushing to maintain attachment to the seat and restrain the occupant from translation. Thus the design criteria are bounded i.e. the keel beam must be soft enough to buckle and collapse during crash loads but stiff enough not to buckle under flight loads. IDRF is developing an energy absorbing subfloor for a Learfan aircraft that will be retrofitted into an existing aircraft and tested to determine its effectiveness in reducing occupant loads. As part of IDRF's development a current technology full scale Learfan aircraft with carbon/epoxy composite fuselage and aluminum floor/subfloor was tested at the IDRF to provide baseline data against which energy absorbing subfloor results can be compared. The aircraft was tested by attaching it to a large gantry with a swing mechanism that swings the aircraft into a desired impact surface. The pitch/roll/yaw, vertical sink rate and impact angle are controlled by the swing's cabling system and release elevation. Instrumented test dummies are placed in

the occupant seating to measure various loads and accelerations acting on different portions of their body during the impact. NASA technical note TN D-8179 [12] describes the test facility in detail. A sketch of the test fixture is shown in figure B-1.2.

The results from the Learfan test showed that this combination of fuselage and subfloor has vertical seat rail accelerations of 200 g's and vertical lumbar loads in excess of the maximum allowable 1500 lb limit for both standard and energy absorbing seats, Jones and Carden [7]. Occupants would not have survived these crash loads or would have sustained serious injury. The large vertical acceleration and excessive lumbar load is a result of the aluminum keel beam's high buckling strength. By designing a composite keel beam to buckle at lower loads and to crush thereafter at a reasonably constant load the acceleration and occupant loads will be reduced to survivable levels.

In the design of the energy absorbing structures it is advantageous to define parameters that characterize their crushing and energy absorptive properties. NASA researchers have defined parameters such as crush initiation load (CIL), sustained crush load (SCL), crush efficiency and energy absorption (EA) as primary parameters to describe crushing and energy absorption characteristics. Crush initiation load is the load at which an initial failure occurs, typically buckling. Sustained crush load is the average load required to produce continuous crushing of the structure after the initial failure. Crush efficiency is the percent reduction in the structure's height at which crushing stops due to the structure becoming rigid or due to global failure. The crush load either increases dramatically or

decreases dramatically at the point crushing stops. Energy absorption of the structure is equivalent to the work done during crushing of the structure. These parameters are depicted in figures B-1.3 and B-1.4.

Previous research conducted by Cronhkite [3] found that the sustained crush load should be in the range of 200 to 300 Lb per linear inch of the keel beam for general aviation seating to keep occupant acceleration loads below the 1500 Lb limit. The SCL needed to limit occupant acceleration loads is a function of the seat type, subfloor and the type structure to which the subfloor is attached. Thus the optimal SCL varies between aircraft types such as general aviation and transport. No set value has been established for the crush initiation load but it should be well above the maximum in flight load while being low enough so as not to impart excessive loads to the occupant. The upper limit of CIL is a function of the initiation load duration. It is desired that the energy to initiate crushing be much smaller than the crushing energy thus the shorter the initiation load duration the larger the allowable force. A high crush efficiency such as 80% to 90% is desired since the energy absorption is proportional to the percent crushing in the beam.

IDRF has conducted research on various beam configurations to identify the most suitable for use as subfloor keel beams. Carden and Kellas [2] performed experimental studies on corrugated composite beam sections to determine if they had crushing characteristics similar to the desired values outlined above. Their work found that their SCL was 550

Lb/in, twice the desired level. Carden and Kellas were able to lower the corrugated section's sustained crush load by using a sandwich type construction consisting of a foam core sandwiched between kevlar face sheets. This type construction lowered the SCL to 237 Lb/in which is within the desired range. In addition to having the desired SCL this section had a good crush efficiency of 75% and had enough post-crush strength to properly restrain occupant seats. Unfortunately the manufacturability of the corrugated beam was not economically practical and thus had to be ruled out for possible use as a keel beam. Kellas continued the work by experimental characterization of various arrangements of more easily manufactured rectangular beam configurations, Kellas [8]. The beam sections consisted of low density PVC foam blocks wrapped in a glass/epoxy laminate joined side to side and sandwiched between kevlar/epoxy face sheets to hold the blocks together and increase buckling resistance. A sketch of the rectangular composite beam construction is shown in figure B-1.5. Kellas tested many different configurations by varying the foam block width, length, and wrapping laminate architecture and by varying the face sheet laminate architecture. The rectangular beam configurations exhibited the desired crushing characteristics with sustained crush loads between 135 Lb/in and 375 Lb/in, crush efficiencies of 30% to 83% and energy absorptions of 620 Lb/in to 1346 Lb/in. The test results indicate that the rectangular beam configuration is an excellent choice for subfloor keel beams.

Kellas tested a 12 in section of a rectangular composite beam web (no seat rail, seat foot

or cross braces included) to characterize the crushing behavior of the composite web and determine its suitability for use in keel beams. The results indicated that the rectangular foam block composite web is a good candidate for use in keel beams. However further analysis of the keel beam with the seat rail, seat foot and cross braces included are needed to tailor the beam's crushing performance so that the combined system will meet the desired crushing criteria. IDRF's goal is to optimize the keel beam crush performance by adjusting its parameters such as foam density, block size and laminate architecture so that the combined system gives the desired crushing characteristics. It is both time consuming and expensive to perform experimental optimization of the combined system. Thus IDRF is continuing development of the composite keel beam through computer modeling of the system.

1.2 Problem Statement

In order to optimize the keel beam crushing performance analytically a finite element modeling technique that approximates the physical phenomena occurring during the crushing event must be developed and validated using the test results obtained by Kellas [8]. Once an accurate modeling technique is established a system model can be created and keel beam parameters adjusted to optimize the energy absorptive (EA) properties. IDRF has selected MSC/Dytran™ as the finite element software in which impact simulations will be performed. The object of the thesis is to develop a finite element model within MSC/Dyrtran that accurately predicts the crushing characteristics and EA

parameters.

1.3 Approach

The crushing behavior of the keel beam test specimen and subfloor assembly will be determined analytically using a finite element model and explicit time integration solution algorithm. An outline of the approach used to construct and solve the finite element model is given below.

1) Theory

   a) structure's equation of motion.

   b) finite element representation of equation of motion.

   c) displacement and strain formulations of elements for use in finite element equation of motion.

   d) constitutive models used to represent material stress/strain relationship.

   e) failure models used to determine when material failure occurs.

   f) explicit solution technique used to solve equation of motion.

2) Finite Element Model Creation

   a) description of impact test to be modeled.

   b) description of impact test specimen.

   c) modeling technique used to represent the test sample and impact test fixture kinematics.

d) impact energy approximation.

3) Material Properties

a) summary of standard material properties.

b) testing of glass/epoxy and kevlar/epoxy lamina materials.

c) data reduction to determine lamina elastic and strength properties.

4) Model Solution, Results, Correlation and Modifications

a) type of results extracted from solution and time interval of extraction.

b) determination of crush performance parameters.

c) correlation to test values.

d) identify discrepancies and formulate modeling changes.

e) implement corrective changes until correlation is established.

Chapter 2

Theory

To develop an accurate model of a structure its physical behavior must be understood. This behavior is converted into a mathematical model using, for example, the finite element method. In the finite element method the physical structure is represented by a set of elements that approximate the structural behavior over their sub-domain. The structure's total response is then taken as the superposition of all elemental responses. Mathematical formulations are used to represent field variables over the element sub-domain. In structural analyses the field variable is often taken to be displacement. The formulations contain assumptions in the representation of the displacement field and the strain-displacement relationship. Examples of such assumptions are: linearly varying displacement over the element and small strains. These assumptions lead to limitations on the usage of the elements. It is critical that the assumptions and limitations of the elements are clearly understood so that they are used correctly in the representation of the physical structure.

A theoretical derivation leads to the structure's equations of motion. These equations are then cast into the form of finite element equations where displacements and strains are represented via element shape functions. The element formulations available in the

structural analysis software MSC/Dytran™ used by NASA Langley to simulate impact will be reviewed to highlight the involved assumptions and the limitations.

Once the equations of motion are put into the finite element format the solution of the equations is examined to highlight any limitations and caveats. The solution of the equations of motion will give elemental nodal displacement results, from which, strain, stress, and failure conditions can be determined. Thus constitutive relationships for composite materials will be developed that enable stress, onset of plasticity, and failure to be determined from the calculated strains. Lastly, failure models will be developed in order to determine which model best describes the failure characteristics in the materials.

2.1 Equations of Motion

The equations of motion are developed for an arbitrary volume over which surface tractions and body forces act to produce acceleration and strain energy. The volume with the applied forces is shown in figure B-2.1 . The principal of virtual work is used to develop the equations of motion. The principal of virtual work states that the work done by all the applied forces (surface traction and body forces) and the inertia forces over a virtual displacement δu_i is equivalent to $\int_V \sigma_{ij}\, \delta u_{i,j}\, dV$ where the standard index notation is used in combination with Einstein's summation convention. The quantity σ_{ij} is the stress tensor and $\delta u_{i,j}$ are the displacement gradients. To prove this principle, consider the equations of motion at a point in the structure:

$$\sigma_{ij,j} + b_i = \rho u_{i,tt} \tag{2.1}$$

Where u_i is the displacement vector, t is time, ρ is the material density, and b_i is the body force per unit volume. The comma "," stands for "partial derivative with respect to". The virtual work done by all external forces acting over a virtual displacement δu_i is given by:

$$\int_V b_i \delta u_i dV + \int_S \sigma_i \delta u_i dS \tag{2.2}$$

where σ_i is the applied traction vector. Note that δu_i must be triply differentiable but need not remain within the material's elastic range provided an appropriate constitutive relation is used. The externally applied traction components can be written as:

$$\sigma_i = \sigma_{ij} n_j \tag{2.3}$$

where n_j is a unit vector outwardly normal to the surface S. Substituting 2.3 into 2.2 yields:

$$\int_V b_i \delta u_i dV + \int_S \sigma_{ij} n_j \delta u_i dS \tag{2.4}$$

The surface integral can be transformed into a volume integral using the divergence theorem which states that for a function $v(x_1, x_2, \cdots, x_n)$ with continuous first derivatives:

$$\int_S v_i n_i dS = \int_V v_{i,i} dV \tag{2.5}$$

Using 2.5 to convert the surface integral gives:

$$\int_s \sigma_{ij} n_j \delta u_i dS = \int_V (\sigma_{ij} \delta u_i)_{,j} dV \tag{2.6}$$

Expanding the partial derivative in the volume integral gives:

$$\int_V (\sigma_{ij}\delta u_i)_{,j} dV = \int_V \sigma_{ij,j}\delta u_i dV + \int_V \sigma_{ij}\delta u_{i,j} dV \tag{2.7}$$

Substituting 2.7 into 2.4 gives:

$$\int_V b_i \delta u_i dV + \int_V \sigma_{ij,j}\delta u_i dV + \int_V \sigma_{ij}\delta u_{i,j} dV \tag{2.8}$$

The partial derivative of the stress tensor, $\sigma_{ij,j}$ can be expressed in terms of the body force and inertia force by rearranging 2.1 .

$$\sigma_{ij,j} = \rho u_{i,tt} - b_i \tag{2.9}$$

Substituting the rearranged 2.1 into 2.8 gives:

$$\int_V b_i \delta u_i dV + \int_V (\rho u_{i,tt} - b_i)\delta u_i dV + \int_V \sigma_{ij}\delta u_{i,j} dV \tag{2.10}$$

Canceling the body force terms gives:

$$\int_V \rho u_{i,tt}\delta u_i dV + \int_V \sigma_{ij}\delta u_{i,j} dV \tag{2.11}$$

Therefore the original statement of virtual work in 2.2 reduces to an equivalent form of virtual work in 2.11 . These two forms can be equated to give:

$$\int_V (b_i - \rho u_{i,tt})\delta u_i dV + \int_S \sigma_i \delta u_i dS = \int_V \sigma_{ij}\delta u_{i,j} dV \tag{2.12}$$

This is a rather general form of the principle of virtual work valid for non-linear constitutive relationships as well as for large strains. A different form can be obtained

by expressing $\delta u_{i,j}$ in terms of the small strain tensor which is defined as:

$$e_{ij} = \frac{1}{2}\left(\frac{\partial u_i}{\partial x_j} + \frac{\partial u_j}{\partial x_i} \right) = \frac{1}{2}(u_{i,j} + u_{j,i}) \tag{2.13}$$

Because the stress tensor is symmetric it follows that $\sigma_{ij} = \sigma_{ji}$ and therefore:

$$\sigma_{ij} u_{i,j} = \sigma_{ji} u_{j,i} = \sigma_{ij} u_{j,i} \tag{2.14}$$

Then

$$\sigma_{ij} \delta u_{i,j} = \frac{1}{2}\sigma_{ij}(\delta u_{i,j} + \delta u_{j,i}) + \frac{1}{2}\sigma_{ij}(\delta u_{i,j} - \delta u_{j,i}) \tag{2.15}$$

Using 2.14 in 2.15 yields:

$$\sigma_{ij} \delta u_{i,j} = \frac{1}{2}\sigma_{ij}(\delta u_{i,j} + \delta u_{j,i}) = \sigma_{ij} \delta e_{ij} \tag{2.16}$$

Therefore:

$$\int_V \sigma_{ij} \delta u_{i,j} dV = \int_V \sigma_{ij} \delta e_{ij} dV \tag{2.17}$$

Substituting 2.17 into 2.12 and rearranging gives:

$$\int_V (b_i - \rho u_{i,tt}) dV + \int_S \sigma_i \delta u_i dS = \int_V \sigma_{ij} \delta e_{ij} dV \tag{2.18}$$

This is a an alternative form of the variational equations of motion in terms of the small strain tensor. It states that the work done by body forces, inertia forces and surface tractions equals the work done in producing strains in the volume, $\int_V \sigma_{ij} \delta e_{ij} dV$. Note that

this form is still valid for non-linear materials and large strains. However, even if the strains are large, it is still the small strain tensor that must be used in 2.18.

2.2 Finite Element Representation of Equation of Motion

The solution to the variational equation of motion is approximated using the finite element technique where the structure is discretized into sub-domains called finite elements. The technique employs the assumed modes method to approximate the field variable over the element sub-domains in terms of the of the field variable at the element nodes using a set of chosen shape functions. Figure B-2.2 shows a simple finite element representation of an arbitrary volume. The total response of the structure is then approximated as the superposition of all elemental responses. The response is approximated over the element due to the near impossibility of postulating an assumed mode that would represent the overall response. The response over an element sub-domain is much simpler and can often be represented using linear assumed modes. The assumed mode method approximates the field variable as a linear combination of shape functions of position only. The coefficients are the values of the field variable at the element nodes and are functions of time only. The elements in MSC/Dytran™ employ a quadratic shape function to represent the field variable of displacement. The trade-off of simplifying the assumed mode to a linear shape function is that the volume must be divided into smaller sub-domains to accurately represent the field variable and its gradients. In general the simpler the element shape function the more elements required

to model the structure.

Using assumed modes a displacement in the variational equation of motion for an element is approximated as:

$$u_i(x_j,t) = u_i(x_j(\xi_k),t) = \sum_{j=1}^{n} N_{ij}(\xi_k)\, q_j(t) \tag{2.19}$$

where $N_{ij}(\xi_k)$ is the shape function associated with node j and the i coordinate direction, expressed in terms of the parametric coordinates ξ_k of the element. It is a function of ξ_k only. The $q_j(t)$ $(j=1,2,\cdots,n)$ are n generalized coordinates for the element and are functions of t only. In matrix form 2.19 can be written as:

$$\mathbf{u} = N\mathbf{q} \tag{2.20}$$

where

$$\mathbf{u} = \begin{Bmatrix} u_1 \\ u_2 \\ u_3 \end{Bmatrix}, \quad \mathbf{q} = \begin{Bmatrix} q_1 \\ q_2 \\ \cdots \\ q_n \end{Bmatrix}, \quad N = \begin{bmatrix} N_{11} & N_{12} & \cdots & N_{1n} \\ N_{21} & N_{22} & \cdots & N_{2n} \\ N_{31} & N_{32} & \cdots & N_{3n} \end{bmatrix} \tag{2.21}$$

and $\mathbf{u}$ is called the displacement vector, $\mathbf{q}$ the generalized displacement vector, and N the shape function matrix. Equation 2.18 can also be written in matrix form:

$$\delta\Pi \equiv \int_V (\mathbf{b}^T - \rho\ddot{\mathbf{u}}^T)\,\delta\mathbf{u}\, dV + \int_S \sigma_*^T \delta\mathbf{u}\, dS - \int_V \sigma^T \delta\mathbf{e}\, dV = 0 \tag{2.22}$$

where Π is the potential energy of the system and $\delta\Pi$ is a small variation of its potential

energy and where:

$$\mathbf{b}=\begin{Bmatrix} b_1 \\ b_2 \\ b_3 \end{Bmatrix}, \quad \ddot{\mathbf{u}}=\begin{Bmatrix} \ddot{u}_1 \\ \ddot{u}_2 \\ \ddot{u}_3 \end{Bmatrix}, \quad \sigma_*=\begin{Bmatrix} \sigma_{*1} \\ \sigma_{*2} \\ \sigma_{*3} \end{Bmatrix}, \quad \sigma=\begin{Bmatrix} \sigma_{11} \\ \sigma_{22} \\ \sigma_{33} \\ \sigma_{12} \\ \sigma_{23} \\ \sigma_{31} \end{Bmatrix}, \quad \mathbf{e}=\begin{Bmatrix} e_{11} \\ e_{22} \\ e_{33} \\ 2e_{12} \\ 2e_{23} \\ 2e_{31} \end{Bmatrix} \tag{2.23}$$

Note that **b** is called the body force vector, $\ddot{\mathbf{u}}$ the acceleration vector, σ_* the traction vector, σ the stress vector, and **e** the small strain vector. Also note that the subscript $(\ )_*$ is used to distinguish the traction vector from the stress vector. Also, the small strain tensor is related to the regular engineering strain as follows:

$$\epsilon_x = e_{11},\ \epsilon_y = e_{22},\ \epsilon_z = e_{33},\ \gamma_{xy} = 2e_{12},\ \gamma_{yz} = 2e_{23},\ \gamma_{zx} = 2e_{31} \tag{2.24}$$

Next, 2.13 can also be written in matrix form as:

$$\mathbf{e}=B\mathbf{u}, \quad B=\begin{bmatrix} \frac{\partial}{\partial x_1} & 0 & 0 & \frac{\partial}{\partial x_1} & 0 & \frac{\partial}{\partial x_1} \\ 0 & \frac{\partial}{\partial x_2} & 0 & \frac{\partial}{\partial x_2} & \frac{\partial}{\partial x_2} & 0 \\ 0 & 0 & \frac{\partial}{\partial x_3} & 0 & \frac{\partial}{\partial x_3} & \frac{\partial}{\partial x_3} \end{bmatrix}^T \tag{2.25}$$

Using 2.20 and 2.25 in 2.22 yields for a particular element *e*

$$\delta\Pi_e = \delta\mathbf{q}_e^T\left[\int_{V_e}\rho_e N_e^T N_e \ddot{\mathbf{q}}_e dV_e + \int_{V_e} N_e^T B_e^T \sigma_e dV_e - \int_{V_e} N_e^T \mathbf{b}_e dV_e - \int_{S_e} N_e^T \sigma_{e*} dS_e\right] = 0 \tag{2.26}$$

Now, letting $\mathbf{q}$ be the global generalized coordinate vector, it follows that for every element e

$$\mathbf{q}_e = Q_e \mathbf{q} \tag{2.27}$$

where Q_e is a locator matrix with elements 0 and 1 which place the element vector $\mathbf{q}_e$ into the global vector $\mathbf{q}$. Substituting 2.27 into 2.26, summing over all elements e, and assuming all generalized coordinates to be independent yields the global equations of motion

$$\sum_e Q_e^T \left[\int_{V_e} \rho_e N_e^T N_e \ddot{\mathbf{q}}_e dV_e + \int_{V_e} N_e^T B_e^T \sigma_e dV_e - \int_{V_e} N_e^T \mathbf{b}_e dV_e - \int_{S_e} N_e^T \sigma_{e*} dS_e \right] = 0 \tag{2.28}$$

Note that in the process all the inter-element reactions are eliminated and that the inter-element displacement compatibility (continuity of displacement between elements) is satisfied.

2.3 Element Formulations

The limitations of an element arise from its formulation. Thus it is beneficial to review the element formulation before applying it to a particular problem to ensure that it can accurately approximate the expected solution. The element types used to model the composite beam are the 8-noded solid or brick and the 4 noded quadrilateral thinshell. The 8-noded brick element is used to represent the foam material in the composite beam while the 4- noded quadrilateral thinshell is used to model the laminate that wraps the foam. The formulations of these elements are reviewed in the following sections. This

will allow for the determination of the N and B matrices and their validation for the impact problem.

2.3.1 Eight Noded Hexahedron Element

The isoparametric 8-noded hexahedron (or brick) element is shown in Figure 2.3. This is the generic version relative to the natural coordinate system (ξ_1, ξ_2, ξ_3). Note the ordering of the nodes relative to the natural coordinate system. This order must be adhered to for all brick elements in a structure. The nodes 1, 2, 3, and 4 and the nodes 5, 6, 7, and 8 must be ordered in counter clockwise fashion as seen from the positive axis.

The generalized coordinates are taken as the 24 translational displacements at the corners of the brick. The continuous displacement vector **u** within the element is given by equation 2.29

$$\mathbf{u} = N\mathbf{q} \tag{2.29}$$

where

$$\mathbf{q} = \begin{bmatrix} q_1 & q_2 & q_3 & \cdots & q_{22} & q_{23} & q_{24} \end{bmatrix}^T \equiv \begin{bmatrix} u_{11} & u_{21} & u_{31} & \cdots & u_{18} & u_{28} & u_{38} \end{bmatrix}^T \tag{2.30}$$

and

$$N = \begin{bmatrix} N_{11} & N_{12} & N_{13} & \cdots & N_{122} & N_{123} & N_{124} \\ N_{21} & N_{22} & N_{23} & \cdots & N_{222} & N_{223} & N_{224} \\ N_{31} & N_{32} & N_{33} & \cdots & N_{322} & N_{323} & N_{324} \end{bmatrix} = \begin{bmatrix} N_1 & 0 & 0 & \cdots & N_8 & 0 & 0 \\ 0 & N_1 & 0 & \cdots & 0 & N_8 & 0 \\ 0 & 0 & N_1 & \cdots & 0 & 0 & N_8 \end{bmatrix} \tag{2.31}$$

with

$$N_j = \frac{1}{8}\prod_i \left(1+\xi_i\xi_{ij}\right) \equiv \frac{1}{8}\left(1+\xi_1\xi_{1j}\right)\left(1+\xi_2\xi_{2j}\right)\left(1+\xi_3\xi_{3j}\right), \quad j=1,2,\cdots,8 \tag{2.32}$$

Note that u_{ij} is the u_i displacement at the node j and ξ_{ij} are the natural coordinates of node j. Also note that the shape functions for the brick element are written in terms of the ξ_i coordinates. Natural coordinates are such that they have the values at the corners as shown in figure B-2.3. These coordinates are related to the x_i coordinates in the same way the continuous displacements are related to the nodal displacements, i.e.,

$$u_i = \sum_{j=1}^{8} N_j u_{ij}, \quad x_i = \sum_{j=1}^{8} N_j x_{ij} \tag{2.33}$$

In other words the brick element is an isoparametric element. The shape functions N_i in equations 2.32 and 2.33 are determined in such a way that $N_i = 1$ at the i node and zero at all other nodes. This ensures satisfaction of the displacement requirements at the nodes, i.e., at the nodes the continuous displacements are equal to the nodal displacements. The shape functions have a linear variation between nodes as shown in figure B-2.4 To determine the strain in terms of the nodal displacements we first write (via the chain rule)

$$\frac{\partial u_i}{\partial \xi_j} = \sum_{k=1}^{3} \frac{\partial u_i}{\partial x_k}\frac{\partial x_k}{\partial \xi_j}, \quad i,j = 1,2,3 \tag{2.34}$$

and then solve (2.34) for $\frac{\partial u_i}{\partial x_k}(k = 1,2,3)$

$$\frac{\partial u_i}{\partial x_k} = \frac{1}{\det J}\sum_{l=1}^{3} a_{kl}\frac{\partial u_i}{\partial \xi_l}, \quad a_{kl} = \sum_{m=1}^{3}\sum_{n=1}^{3} \epsilon_{lmn}\frac{\partial x_p}{\partial \xi_m}\frac{\partial x_q}{\partial \xi_n}, \quad k,p,q \text{ cyclic} \tag{2.35}$$

where J is the Jacobian matrix and k, p, q take on the values (1,2,3), (2,3,1), and (3,2,1). From (2.33) we have

$$\frac{\partial x_s}{\partial \xi_t} = \sum_{j=1}^{8} \frac{\partial N_j}{\partial \xi_t} x_{sj} \tag{2.36}$$

and

$$\det J = \sum_{i=1}^{3} a_{1i} \sum_{j=1}^{8} \frac{\partial N_j}{\partial \xi_1} x_{ij} \tag{2.37}$$

The $\partial u_i / \partial x_k$ are now known because the x_{ij} and N_j are known as functions of the ξ_i. From (2.32) we have

$$\frac{\partial N_j}{\partial \xi_1} = \xi_{j1}(1+\xi_2\xi_{j2})(1+\xi_3\xi_{j3}), \frac{\partial N_j}{\partial \xi_2} = (1+\xi_1\xi_{j1})\xi_{j2}(1+\xi_3\xi_{j3}), \frac{\partial N_j}{\partial \xi_3} = (1+\xi_1\xi_{j1})(1+\xi_2\xi_{j2})\xi_{j3} \tag{2.38}$$

For the 8-noded brick we have

$$m = \left[\frac{1}{8}\delta_{ij}\rho \int_{-1}^{1}\int_{-1}^{1}\int_{-1}^{1} |\det J| d\xi_1 d\xi_2 d\xi_3\right], \; k = \left[\int_{-1}^{1}\int_{-1}^{1}\int_{-1}^{1} B^T C B |\det J| d\xi_1 d\xi_2 d\xi_3\right], \; i = 1,2,3 \tag{2.39}$$

where m is the element mass matrix, k is the element stiffness matrix, δ_{ij} is the Kronecker delta (i.e. =1 when $i=j$ and =0 when i≠ j) and C is the material elasticity matrix. Furthermore, the strain components ϵ_{ij} and the displacement components u_i are related as

$$\epsilon_{11} = \frac{\partial u_1}{\partial x_1}, \; \epsilon_{22} = \frac{\partial u_2}{\partial x_2}, \; \epsilon_{33} = \frac{\partial u_3}{\partial x_3}, \; \epsilon_{12} = \frac{\partial u_1}{\partial x_2} + \frac{\partial u_2}{\partial x_1}, \; \epsilon_{23} = \frac{\partial u_2}{\partial x_3} + \frac{\partial u_3}{\partial x_2}, \; \epsilon_{31} = \frac{\partial u_3}{\partial x_1} + \frac{\partial u_1}{\partial x_3} \tag{2.40}$$

so that from (2.33 and 2.35) and the definitions

$$\epsilon_{11} \triangleq \epsilon_1 \ , \quad \epsilon_{22} \triangleq \epsilon_2 \ , \quad \epsilon_{33} \triangleq \epsilon_3 \ , \quad \epsilon_{12} \triangleq \epsilon_4 \ , \quad \epsilon_{23} \triangleq \epsilon_5 \ , \quad \epsilon_{31} \triangleq \epsilon_6$$
$$U_{3(i-1)+j} \triangleq u_{ij} \ , \quad i = 1,\cdots,8 \text{ and } j = 1,2,3 \tag{2.41}$$

we have

$$\epsilon_i = \sum_{j=1}^{24} B_{ij} U_j \tag{2.42}$$

with the nonzero B_{ij} given as

$$B_{j,3(i-1)+j} = \frac{1}{|J|} \sum_{k=1}^{3} a_{jk} \frac{\partial N_i}{\partial \xi_k} \ , \quad j = 1,2,3 \quad B_{4,3i-2} = B_{2,3i-1} \ , \ B_{4,3i-1} = B_{1,3i-2} \ ,$$
$$B_{5,3i-1} = B_{3,3i} \ , \ B_{5,3i} = B_{2,3i-1} \ , \ B_{6,3i-2} = B_{3,3i} \ , \ B_{6,3i} = B_{1,3i-2} \ , \quad i = 1,\cdots,4 \tag{2.43}$$

Because both the B_{ij} and the N_i are functions of the natural coordinates ξ_i, it is necessary to use numerical integration in (2.39) Dytran™ uses single Point Gaussian Quadrature Formula

$$m \approx \frac{1}{8} \delta_{ij} \rho \, |\det J(0)| \ , \quad k \approx B^T(0) \, C \, B^T(0) \, |\det J(0)| \tag{2.44}$$

Note that no higher order derivatives are included in the operator matrix B, i.e., the small strain assumption is used. This assumption is considered suitable since MSC/Dytran™ uses incremental plasticity theory to determine the large strain effects rather than using a finite strain approach. In incremental plasticity the strain and strain rates are determined by solving the elemental equation of motion using explicit time integration with time steps on the order of 10^{-6} to 10^{-9} seconds. Over this time interval the second order displacement gradient terms are negligible compared to the first order terms. Constitutive

equations in conjunction with a yield criteria such as that of Tresca or Von Mises are used to determine the effective plastic strain at each time step. The plastic strains are summed from time step to time step thus approximating large strain over time.

A stress divergence vector is calculated as

$$\mathbf{F} = \int_V N^T B^T \sigma \, dV \tag{2.45}$$

The element force vector is computed as a combination of the body and traction force integrals.

$$\boldsymbol{P} = \int_V N^T \boldsymbol{b} \, dV + \int_S N^T \boldsymbol{t} \, dS \tag{2.46}$$

2.3.2 Shell Element

The Belytschko-Tsay four noded quadrilateral shell element [1] is used to model the kevlar /epoxy and glass /epoxy laminate wrapping the foam cells. Its formulation was developed specifically for the analysis of large deflections and material non-linearities. The element uses a co-rotational coordinate system and rate of deformation formulation. Using a co-rotational coordinate system avoids the difficulties of non-linear mechanics while using the rate of deformation facilitates evaluation of plasticity constitutive relationships typically expressed in terms of strain rate and the usual Cauchy stress tensor. A development of the rate of deformation tensor that closely follows Malvern [10] is

given to highlight its applicability to strain rate.

The relative motion of two particles can be described using their relative velocities. Consider two particles at P and Q. These particles move from P to p and from Q to q respectively as shown in figure B-2.4. The velocity of the particle at q relative to the particle at p is:

$$dv_k = v_{k,m}\, dx_m \tag{2.48}$$

Note that the increment dx_m is the increment at the present time, not the initial or reference increment. The change in velocity components with respect to the coordinate directions can be represented in a spatial gradient of velocity tensor L where:

$$L_{km} = v_{k,m} \tag{2.49}$$

so that the relative velocity becomes:

$$dv_k = L_{km}\, dx_m \tag{2.50}$$

The velocity gradient tensor can be written as the sum of a rate of deformation tensor (stretching tensor) D_{ij} and a vorticity tensor (spin tensor) Ω_{ij}

$$L_{ij} = D_{ij} + \Omega_{ij} \tag{2.51}$$

where

$$D_{ij} = \frac{1}{2}(L_{ij} + L_{ji}) = \frac{1}{2}(v_{i,j} + v_{j,i}), \quad \Omega_{ij} = \frac{1}{2}(L_{ij} - L_{ji}) = \frac{1}{2}(v_{i,j} - v_{j,i}) \tag{2.52}$$

Therefore the relative velocity of the two points can also be written as:

$$dv_k = D_{km} dx_m + \Omega_{km} dx_m \tag{2.53}$$

The rate of deformation tensor is related to the Lagrangian finite strain rate by:

$$\frac{dE_{ij}}{dt} = \frac{\partial x_m}{\partial X_i} D_{mn} \frac{\partial x_n}{\partial X_j} \tag{2.54}$$

In the Lagrangian description the position vector x_i at time t is described in terms of the reference position X_i and the displacement vector u_i as follows:

$$x_i = X_i + u_i \tag{2.55}$$

Substituting 2.55 into 2.54 gives:

$$\frac{dE_{ij}}{dt} = (\delta_{mi} + \frac{\partial u_m}{\partial X_i}) D_{mn} (\delta_{nj} + \frac{\partial u_n}{\partial X_j}) \tag{2.56}$$

For small displacement gradients, $\frac{\partial u_i}{\partial X_j} \ll 1$, 2.56 reduces to:

$$\frac{dE_{ij}}{dt} \approx D_{ij} \tag{2.57}$$

Thus, the strain rate occurring in the element can be approximated by the rate of deformation tensor if the displacement gradients are small.

The mid-surface or reference surface of the Belytschko-Tsay quadrilateral shell element is defined by its four corner nodes. A co-rotational coordinate system that moves with the element (i.e., the coordinate system is embedded in the element) is defined in terms of the

nodal coordinates and is used to transform quantities expressed in the element local coordinate system into the global coordinate system. The co-rotational coordinate system and element coordinate system are shown in figure B-2.6. The co-rotational coordinate system origin is taken at node 1. A superscript * is used to indicate the co-rotational coordinate system. The unit vector $\mathbf{e}_3^*$ along the x_3^* axis is defined from the element diagonals as

$$\mathbf{x}_3^* = \mathbf{r}_{13} \times \mathbf{r}_{24}$$
$$\mathbf{e}_3^* = \frac{\mathbf{x}_3^*}{|\mathbf{x}_3^*|} \tag{2.58}$$

If the four nodes are co-planar then $\mathbf{e}_3^*$ is normal to the mid-plane of the element. When the element deforms an angle can develop between $\mathbf{e}_3^*$ and the mid-plane normal $\mathbf{e}$. This misalignment can be characterized as

$$|\mathbf{e}_3^* \cdot \mathbf{e} - 1| < \delta \tag{2.59}$$

Belytschko recommends that δ be on the order of 0.01. This will ensure that the difference between the rotation of the co-rotational coordinate system and the rotation of the material is small. Because misalignment results from element warping or twisting it must be said that the element is sensitive to warping and twisting. Next, the x_1^* axis lies approximately along the element 1-2 edge and is defined as

$$\mathbf{x}_1^* = \mathbf{r}_{12} - (\mathbf{r}_{12} \cdot \mathbf{e}_3^*)\mathbf{e}_3^*, \quad \mathbf{e}_1^* = \frac{\mathbf{x}_1^*}{|\mathbf{x}_1^*|} \tag{2.60}$$

This representation makes the x_1^* axis more perpendicular to the x_3^* axis when warping

is present. The x_2^* axis is defined as

$$\mathbf{e}_2^* = \mathbf{e}_3^* \times \mathbf{e}_1^* \tag{2.61}$$

A transformation matrix between the global and co-rotational coordinate systems is defined using the above component vectors

$$\begin{aligned} X_i &= e_{ij}^* x_j^* \\ x_j^* &= e_{ji}^* X_i \end{aligned} \tag{2.62}$$

where the e_{ij}^* are the coordinates of the $\mathbf{e}_i^*$ vectors with respect to the global coordinate system X_i. This transformation allows for the element nodal velocity vector, the mass and stiffness matrices, and the force vector to be written with respect to the global coordinate system. These global quantities can then be substituted into the equation of motion (2.47) to solve for the acceleration, velocity and displacement vectors. The element geometry is then updated in the global system. Also, the unit vectors and transformation matrix are updated after each time step. The spin of the element about the its x_3^* axis is given by

$$\omega_{21}^* = \frac{1}{2}\left(v_{2,1}^* - v_{1,2}^*\right) \tag{2.63}$$

and is used to update the attitude of the x_1^* and x_2^* axes. The spin rate is integrated over the time step to determine the rotation amount and the axes orientations are updated accordingly. Confining the rotations to be about the x_3^* axes seems to be a limitation since rotations can occur about the x_1^* and x_2^* axes due to folding of the specimen sides that occur during crushing.

The shell is considered to be in a state of plane stress, i.e., all quantities are functions of x_1^* and x_2^* only. The deformation occurring in the element is determined from its velocity gradients using the rate of deformation tensor D_{ij}. D_{ij} is taken to be equivalent to the strain rate since displacement gradients must be kept small to keep the co-rotational coordinate system axes aligned with the material, Hallquist [6]. Belytschko uses Mindlin plate theory to describe the velocity of an arbitrary point in the shell. The velocity is the sum of the mid-plane translational velocity and the element rotational velocity.

$$v_i^* = v_i^{*m} - x_3^* \epsilon_{ijk} e_{j3}^* \omega_k^* \tag{2.64}$$

This velocity relationship is substituted into the rate of deformation velocity relationships given by equation 2.52 to give the following velocity strains:

$$\begin{aligned} D_{11}^* &= v_{1,1}^{*m} + x_3^* \omega_{2,1}^* \\ D_{22}^* &= v_{2,2}^{*m} - x_3^* \omega_{1,2}^* \\ 2D_{12}^* &= v_{1,2}^{*m} + v_{2,1}^{*m} + x_3^* \left(\omega_{2,2}^* - \omega_{1,1}^* \right) \\ 2D_{23}^* &= v_{3,2}^{*m} - \omega_1^* \\ 2D_{13}^* &= v_{3,1}^{*m} + \omega_2^* \end{aligned} \tag{2.65}$$

Note that $D_{33}^* = 0$. The mid-plane position, translational velocity, and rotational velocity are described in terms of the element nodal positions and velocities through the use of shape functions. The element has an isoparametric formulation where the same shape functions are used to describe the geometry and velocity. The element nodes are assumed to lie in the mid-plane so that the mid-plane location and the above velocities are given by:

$$\begin{aligned} x_i^{*m} &= N_I(\xi_1, \xi_2)\, x_{iI}^*(t) \\ v_i^{*m} &= N_I(\xi_1, \xi_2)\, v_{iI}^*(t) \\ \omega_i^{*m} &= N_I(\xi_1, \xi_2)\, \omega_{iI}^*(t) \end{aligned} \tag{2.66}$$

where the x_{iI}^* are the coordinates of node I, v_{iI}^* are the velocity components of node I and ω_{iI}^* are the rotational velocity components of node I in the co-rotational coordinate system. Note that no superscript m is used with the I nodal values since the nodes lie on the mid-plane. Shape functions are taken in all three directions. The element uses the standard quadrilateral bilinear shape functions given below:

$$\begin{aligned} N_1 &= \frac{1}{4}(1-\xi_1)(1-\xi_2) \\ N_2 &= \frac{1}{4}(1+\xi_1)(1-\xi_2) \\ N_3 &= \frac{1}{4}(1+\xi_1)(1+\xi_2) \\ N_4 &= \frac{1}{4}(1-\xi_1)(1+\xi_2) \end{aligned} \tag{2.67}$$

Equations 2.66 and 2.67 are substituted into 2.65 to give the strain rate in terms of nodal velocities as shown below:

$$\begin{aligned} D_{11}^* &= B_{1I}v_{1I}^* + x_3^* B_{1I}\omega_{2I}^* \\ D_{22}^* &= B_{2I}v_{2I}^* - x_3^* B_{2I}\omega_{1I}^* \\ 2D_{12}^* &= B_{2I}v_{1I}^* + B_{1I}v_{2I}^* + x_3^*(B_{2I}\omega_{2I}^* - B_{1I}\omega_{1I}^*) \\ 2D_{23}^* &= B_{2I}v_{3I}^* - N_I\omega_{1I}^* \\ 2D_{13}^* &= B_{1I}v_{3I}^* + N_I\omega_{2I}^* \end{aligned} \tag{2.68}$$

where $B_{1I} = N_{I,1}$ and $B_{2I} = N_{I,2}$. The evaluation is done at the center of the element, i.e., at $\xi = \eta = 0$. Strain rates resulting from the above equation are integrated over the time step using the trapezoid rule to give incremental strain. Incremental strains are summed over time to give total strain. The total strain is used in the constitutive relation to determine the resulting stress. A check is made to determine if the material yield function

has been exceeded, i.e., if the incremental strain causes plasticity. The strain is partitioned into elastic and plastic strain and the stress adjusted back to the yield stress. The details of the constitutive relation will be discussed in the next section.

Letting

$$\begin{aligned} \boldsymbol{\sigma}^* &= \left[\sigma_{11}^* \;\; \sigma_{22}^* \;\; \sigma_{12}^* \;\; \sigma_{13}^* \;\; \sigma_{23}^*\right]^T \\ \mathbf{D}^* &= \left[D_{11}^* \;\; D_{22}^* \;\; 2D_{12}^* \;\; 2D_{13}^* \;\; 2D_{23}^*\right]^T \end{aligned} \tag{2.69}$$

be the stress vector and the velocity strain vector, the principal of virtual power for the shell element can be written as

$$\delta\omega_{iI}^* m_{iI}^* + \delta v_{iI}^* f_{iI}^* = \int_V \boldsymbol{\sigma}^{*T} \delta\mathbf{D}^* \, dV \tag{2.70}$$

where the f_{iI}^* are the nodal forces and the m_{iI}^* are the moments. The index I takes on the values 1 through 4 while i takes on the values 1 through 3. Applying the standard Mindlin plate theory, equation (2.70) can be written as

$$\delta\omega_{iI}^* m_{iI}^* + \delta v_{iI}^* f_{iI}^* = \int_V \left(\boldsymbol{\sigma}^{*\prime T} \delta\mathbf{D}^{*\prime} + \kappa\, \boldsymbol{\sigma}^{*\prime\prime T} \delta\mathbf{D}^{*\prime\prime}\right) dV \tag{2.71}$$

where

$$\begin{aligned} \boldsymbol{\sigma}^{*\prime} &= \left[\sigma_{11}^* \;\; \sigma_{22}^* \;\; \sigma_{12}^*\right]^T, \quad \boldsymbol{\sigma}^{*\prime\prime} = \left[\sigma_{13}^* \;\; \sigma_{23}^*\right]^T \\ \mathbf{D}^{*\prime} &= \left[D_{11}^* \;\; D_{22}^* \;\; 2D_{12}^*\right]^T, \quad \mathbf{D}^{*\prime\prime} = \left[2D_{13}^* \;\; 2D_{23}^*\right]^T \end{aligned} \tag{2.72}$$

Substituting 2.68 into 2.71, recognizing that the variations of the generalized coordinates

are independent, and using single point quadrature on the integral, the element forces and moments are determined to be:

$$f_{1I}^{*}=\overline{B}_{1I}F_{11}^{*}+\overline{B}_{2I}F_{12}^{*},\quad f_{2I}^{*}=\overline{B}_{2I}F_{22}^{*}+\overline{B}_{1I}F_{12}^{*},\quad f_{3I}^{*}=\kappa(\overline{B}_{1I}F_{13}^{*}+\overline{B}_{2I}F_{23}^{*})$$
$$m_{1I}^{*}=\overline{B}_{2I}M_{22}^{*}+\overline{B}_{1I}M_{12}^{*}-\frac{A\kappa}{4}F_{23}^{*},\quad m_{2I}^{*}=-\overline{B}_{1I}M_{11}^{*}-\overline{B}_{2I}M_{12}^{*}+\frac{A\kappa}{4}F_{13}^{*},\quad m_{3I}^{*}=0 \tag{2.73}$$

where A is the element area and

$$F_{ij}^{*}=\int_{-t/2}^{t/2}\sigma_{ij}^{*}\,dx_3^{*},\quad M_{ij}^{*}=-\int_{-t/2}^{t/2}x_3^{*}\sigma_{ij}^{*}\,dx_3^{*},\quad \overline{B}_{iI}=\int_{A}B_{iI}\,dA \tag{2.74}$$

The forces and moments acting at the nodes are resolved into global components using the co-rotational coordinate system transformation matrix. These are then combined with the traction forces and substituted into the element equation of motion along with the element mass and stress divergence vector to obtain the solution of the nodal accelerations, velocities, and displacements.

2.4 Constitutive Relationships and Failure Models

2.4.1 Orthotropic Constitutive Relation and Failure Model

A plane stress orthotropic constitutive relation was initially used to represent the kevlar/glass/epoxy laminate. The orthotropic relation describes a linear elastic behavior up to a brittle type failure. The in-plane stress-strain relationships are given by :

$$\sigma = C\epsilon, \quad \sigma = \left[\sigma_{11} \;\; \sigma_{22} \;\; \sigma_{12}\right]^T, \quad \epsilon = \left[\epsilon_{11} \;\; \epsilon_{22} \;\; \epsilon_{12}\right]^T$$

$$C = \frac{1}{1-\nu_{12}\nu_{21}} \begin{bmatrix} E_{11} & \nu_{21}E_{11} & 0 \\ \nu_{21}E_{11} & E_{22} & 0 \\ 0 & 0 & G_{12} \end{bmatrix} \tag{2.75}$$

The strains in an element are evaluated at time $t+\frac{\Delta t}{2}$ by integrating its strain rate components from $t-\frac{\Delta t}{2}$ to $t+\frac{\Delta t}{2}$ using the trapezoidal rule. The strain is summed over the time steps to obtain the total strain. Using these strains, the element elastic stresses are calculated from 2.68. After determining the stresses, the failure criterium is evaluated to determine if the element has reached the point of failure. MSC/Dytran™ offers six (6) failure models for orthotropic materials, all stress based. The Tsai-Wu criteria was chosen since it is based on a tensor representation of strength components that is invariant with respect to coordinate transformation, it allows for differences in tensile and compressive strengths, it accounts for interaction between normal stresses, and it is computationally efficient. For the plane stress problem the Tsai-Wu failure criteria is:

$$f_1\sigma_{11} + f_2\sigma_{22} + f_{11}\sigma_{11}^2 + f_{22}\sigma_{22}^2 + f_{66}\sigma_{12}^2 + 2f_{12}\sigma_{11}\sigma_{22} \geq 1 \tag{2.76}$$

where

$$f_1 = \frac{1}{S_{1T}} - \frac{1}{S_{1C}}, \quad f_2 = \frac{1}{S_{2T}} - \frac{1}{S_{2C}}, \quad f_{11} = \frac{1}{S_{1T}\,S_{1C}}$$
$$f_{22} = \frac{1}{S_{2T}\,S_{2C}}, \quad f_{12} = -\frac{1}{2}f_{11}f_{22}, \quad f_{66} = \frac{1}{S_S^2} \tag{2.77}$$

and

S_{1T} = longitudinal tensile yield strength

S_{1C} = longitudinal compressive yield strength

S_{2T} = transverse tensile yield strength

S_{2C} = transverse compressive yield strength

S_S = shear strength

If the failure criteria is met then the element fails and its elastic properties are reduced to zero (0) over a specified time or number of time steps.

The use of an orthotropic constitutive relation proved to be unfeasible due to its brittle failure characteristics. The failure criteria is met during the crush initiation load which results in element failure. Large sections of elements fail due to the uniformity of the model geometry and element properties. Once the laminate elements fail the foam becomes unconstrained and is free to flow. Thus the model essentially shatters at impact and collapses. An elastic-plastic constitutive relationship had to be used in place of the orthotropic relationship to prevent this type failure.

2.4.2 Elastic-Plastic Constitutive Relationship

An elastic-plastic constitutive relationship is used to represent the laminate stress-strain relationship due to problems with premature failure of the orthotropic representation. MSC/Dytran™ only offers an elastic-plastic relationship with isotropic hardening thus it is used rather than kinematic hardening. The stress-strain relationship is the same as 2.75

except that is C given by:

$$C = \frac{E}{1-\nu^2}\begin{bmatrix} 1 & \nu & 0 \\ \nu & 1 & 0 \\ 0 & 0 & \frac{1-\nu}{2} \end{bmatrix} \tag{2.78}$$

The element strain and elastic stress is calculated as described for the orthotropic relation. The plastic behavior is based on a von Mises yield function shown below:

$$\phi = J_2 - \frac{\sigma_Y^2}{3} \tag{2.79}$$

where J_2 is expressed in terms of the deviatoric stresses

$$J_2 = \frac{1}{2} s_{ij}\ s_{ij} \tag{2.80}$$

and the yield stress σ_Y is a function of the effective plastic strain ϵ^p_{eff} and the plastic hardening modulus E_p:

$$\sigma_Y = \sigma_{Y0} + E_p \epsilon^p_{eff} \tag{2.81}$$

where σ_{Y0} is the initial yield strength. Yielding is produced by deviatoric stresses only. Hydrostatic stresses do not contribute to yielding. The von Mises yield function is a cylindrical surface in principal stress space with its radius equal to the yield stress. In isotropic hardening the yield surface center does not move relative to the principle stress hydrostat (line of $\sigma_{p1} = \sigma_{p2} = \sigma_{p3}$) due to plastic strain effects. Thus the yield surface axis lies along the hydrostat. A sketch of the yield surface is shown in figure 2.7 .

The deviatoric stresses are computed from the stress tensor as :

$$s_{ij} = \sigma_{ij} - \frac{1}{3}\sigma_{kk} \tag{2.82}$$

The plastic hardening modulus is given by:

$$E_p = \frac{E E_H}{E - E_H} \tag{2.83}$$

E is the slope of the elastic stress-strain curve while E_H is the slope of the post yield stress-strain curve. E and E_H are shown on a typical stress-strain curve in figure B-2.8 . The effective plastic strain is taken as the integral of incremental plastic strain over time.

$$\epsilon^p_{eff} = \int_0^t d\epsilon^p_{eff} \tag{2.84}$$

For small strain increments and proportional straining the incremental effective plastic strain can be determined from incremental plastic strain components, Malvern [10].

$$d\epsilon^p_{eff} = \sqrt{\frac{2}{3} d\epsilon^p_{ij}\, d\epsilon^p_{ij}} \tag{2.85}$$

The incremental strain that occurs over a time step is initially assumed elastic. The stress tensor at $t + \Delta t$ is computed as

$$\sigma^{t+\Delta t}_{ij} = \sigma^t_{ij} + C_{ijkl}\, \Delta\epsilon^{t+\Delta t/2}_{kl} \tag{2.86}$$

The deviatoric stresses are computed using this stress tensor. The yield function is then evaluated with s_{ij} assumed to be elastic. If $\phi \leq 0$ then yielding does not occur and the incremental stress and strain are added to the previous time step stress and strain. If

$\phi > 0$ yielding occurs and the incremental strain is taken as being plastic. The incremental effective plastic strain is calculated from 2.85 . The incremental effective plastic strain is added to any previous effective plastic strain to give the total effective plastic strain. The yield stress is updated using 2.81 and the deviatoric stress components are scaled back proportionally to the updated yield stress value.

2.4.3 Crushable Foam Constitutive Relationship

The foam material used in the composite beam is represented by an isotropic crushable foam constitutive relation. Its Poisson's ratio is taken to be zero thus σ_{11}, σ_{22}, and σ_{33} are not coupled. Therefore a uniaxial tension/compression test stress-strain curve and a volumetric compression test pressure-relative volume curve are the same. The yield behavior is assumed to be determined by either of these curves and a strain rate factor, MacNeal-Schwendler Corporation, [9]. The foam does show sligth orthotropic behavior and has a Poisson's ratio of .2, however, the orthotropic effects are small and the isotropic representation is considered adequate. The stress-strain curve for foam is highly non-linear and cannot be described by elastic and plastic moduli. A typical foam stress-strain curve is shown in figure B-2.8. MSC/Dytran™ uses a bulk modulus along with a stress-strain table to describe the stress-strain curve. At small strains the stress is related to strain linearly through the bulk modulus. However as the strain increases the foam yields in a non-linear fashion thus pairs of strain and corresponding stress values are entered into a table to define the stress-strain curve.

The yield surface is taken as a sphere in principal stress space. Thus the yield function without strain rate effects is given as:

$$\sigma_{ii}^2 - \sigma_Y^2 = 0; \quad \sigma_Y = f_1(R_e), \quad R_e^2 = \epsilon_{ii}^2 \tag{2.87}$$

The strain components are calculated for the solid element using the element equation of motion at $t = t + \frac{\Delta t}{2}$. The foam is assumed to behave elastically and the stress components are calculated using the bulk modulus. The principal strains are used to calculate R_e which is essentially a measure of effective strain. The stress-strain table is taken as f_1 and is used to determine R_s for the given R_e. The yield function is then evaluated using the elastic principal stresses and R_s to determine if yielding occurs. If yielding does occur the stresses are scaled back proportionally according to:

$$\sigma_j = \frac{\sigma_j}{\sqrt{\sigma_{ii}^2}} \sigma_Y \tag{2.88}$$

When unloaded, the stress-strain curve follows a nonlinear hysteresis loop that is constructed such that the ratio of dissipated energy (area between compressive loading and unloading curves) to total energy (area under loading curve) is equal to the energy dissipation factor, MacNeal-Schwendler Corporation [9]. Linear, quadratic and exponential unloading options are available. A plot of the unloading curves is shown in figure B-2.9 .

A failure stress in tension can be defined for the foam. Once the unloading curve reaches the origin and the load becomes tensile the stress-strain relationship is elastic and is

defined by the bulk modulus. The stress increases elastically until it reaches a specified maximum tensile stress. At that point the foam fails and the element stress returns to zero. This element can no longer carry tensile loads but can support compressive loads.

2.5 Solution Technique

The element formulation distributes the element mass, tractions, body forces and stress divergence to the element nodes. This results in element equations of motion in terms of nodal values. These equations of motion are solved using explicit time integration. The equation of motion is put into the following form:

$$\boldsymbol{a}_n = M^{-1} \boldsymbol{F}_n^{res} \tag{2.89}$$

where $\boldsymbol{a}_n$ is the nodal acceleration vector at time step n, M is the diagonal mass matrix and $\boldsymbol{F}_n^{res}$ is the residual force vector. The residual force is comprised of the elemental traction forces, body forces and stress divergence as shown below.

$$\boldsymbol{F}_n^{res} = \int_{S_e} N_e^T \sigma_e^* dS_e + \int_{V_e} N_e^T \boldsymbol{b}_e dV_e - \int_{V_e} N_e^T B_e^T \sigma_e dV_e \tag{2.90}$$

Nodal accelerations are determined directly from 2.90 using prescribed initial conditions and the sum of masses and residual forces acting at the node . Note that the element mass matrices must be in a lumped form so that uncoupled equations result that can be solved directly. Also note that the force and mass components are in terms of the global coordinate system. A central difference time integration is performed to solve for nodal velocities and displacements as shown below:

$$v_{in+\frac{1}{2}} = v_{in-1} + a_{in}\frac{\left(\Delta t_{n+\frac{1}{2}} + \Delta t_{n-\frac{1}{2}}\right)}{2}$$
$$u_{in+1} = u_{in} + v_{in+\frac{1}{2}}\Delta t_{n+\frac{1}{2}} \tag{2.91}$$

The elemental strain rates are determined using the nodal velocities. The nodal velocities are substituted into the element shape functions and operated on by the element gradient operator B matrix. Element strain rates are integrated over the time step to give element strains. The elemental constitutive relations are evaluated next to determine the elemental stresses. The element geometry is updated in the global coordinate system using the nodal displacement vector:

$$x_i = x_{io} + u_{in+1} \tag{2.92}$$

The residual forces acting at the nodes are then updated based on the new element stresses, body forces and traction forces. The updated geometry and residual forces are taken as the staring point of the next iteration and the process is repeated. A flow chart from the Dytran™ manual, MacNeal-Schwendler Corporation [9], showing the solution process is shown in figure B-2.10 .

2.5.1 Solution Stability

The stability of the central difference integration technique is determined by the stability of the linear system, Hallquist [6]. By applying the central difference integration formula to the equation of motion in modal coordinates it can be determined that a stable time step size is related to the highest natural frequency as:

$$\Delta t \leq \frac{2}{\varpi_{max}} \tag{2.93}$$

A modal analysis isn't performed at each time step to determine an appropriate step size. Instead an approximate method known as the Courant Criteria is used to estimate the time step size, MacNeal-Schwendler Corporation [9]. The criteria estimates the time step size as:

$$\Delta t = \frac{SL}{c} \tag{2.94}$$

where L is the smallest element dimension, c is the speed of sound in the element material and S is a timestep scale factor. For structural analyses S can be assigned a value up to .9.

As the elements deform and distort due to impact L becomes smaller which results in smaller time steps. To prevent time steps from becoming unacceptably small, elements in high deformation areas should be as square as possible. MSC/Dytran™ by default allows the timestep to be reduced by 90% of the initially specified time step. In the event that elements compress or distort to the point of reducing the time step to unacceptable levels MSC/Dytran™ offers the option of failing an element based on a user specified minimum time step and removing it from the calculation. This allows the simulation to proceed.

Chapter 3

Finite Element Model

3.1 Impact Test Simulated

Kellas performed EA tests on rectangular composite beam web sections with improved manufacturability to identify an architecture that would give desired EA characteristics, Kellas [8]. The primary EA parameters of interest were CIL, SCL, crush efficiency and energy absorbed. CIL, SCL and crush efficiency were derived from acceleration measurements taken during dynamic impact tests.

Dynamic impact tests were conducted using a drop tower with a crush fixture constrained to move vertically along guide rods. A drawing of the fixture is shown in figure B-3.1 . The fixture consisted of a platen that served as a rigid base support during crushing, an impact mass that rested atop the specimen and provided a crushing force during impact and knife edge supports to support the specimen during crushing. The fixture was attached to a fixture carrier that ran vertically along guide rods in the drop tower. The specimen were placed in the crush fixture and elevated to a height that would give a desired impact velocity and released. The fixture accelerated downward until it impacted with a pulse generator that decelerated the fixture according to a programmed deceleration profile. The deceleration profile was based on sub-floor acceleration measurements taken during the baseline test of the Learfan aircraft. The mass resting atop the test specimen

provided a crushing force during the deceleration. Test specimen were constrained to maintain a vertical orientation during crushing by the knife edge supports. These supports roughly simulate stanchions that run transversely between the keel beams. The stanchions are nominally twelve (12) inches apart in the sub-floor to provide resistance to out of plane bending and axial torsion in the keel beam.

Two accelerometers were used to derive the EA parameters. One accelerometer was located on the impact mass resting atop the specimen. Another accelerometer was located on the fixture platen that supported the specimen. The accelerometer on the impact mass provided a measure of crush force acting on the specimen through the relation $F = ma$. The CIL and SCL were calculated using this accelerometers measurements and the known impact mass. The difference between the impact mass and support platen accelerometer measurements was integrated twice to provide a measure of crush displacement. The crush displacement and crush force was used to produce crush force versus crush displacement curves. The crush displacement was also used to measure crush stoke (reduction in specimen height during crushing) which in turn was used to compute crush efficiency. The energy absorption was determined from the crush force versus crush displacement curve. Energy absorption was computed as the area under the curve up to the point where the slope begins to change rapidly due to the specimen becoming rigid or collapsing.

3.2 Test Specimen Description

Test specimen were twelve (12) inches long and eight (8) inches tall. Widths varied from one (1.0) to two (2.0) inches. The test specimen consisted of rectangular laminated cells joined side to side and contained with a face sheet as shown in figure 1.5. Cell size varied from 1.5 to 3.0 inches. Both empty cells and foam filled cells were tested to determine the foam's effect on energy absorption. Foam filled cells were filled with 1.87 Lb/ft^3 rigid PVC foam. The sides of each cell were wrapped with .01 inch thick $\pm 90^0$ or $\pm 45^0$ satin weave E-glass/epoxy lamina. The lamina fiber volume ratio was not specified. Face sheets were placed on the sides of the wrapped cells consisting of .01 inch. thick $\pm 45^0$ satin weave kevlar/epoxy lamina. The number of lamina in the lay-up was varied from one (1) to two (2) to determine the effect of laminate thickness. The beam variations and their corresponding EA characteristics are given in tables B-3.1 and B-3.2.

From the tabulated results it can be seen that the specimen with foam filled cells had better EA characteristics as more of the foam filled specimen had SCL values within the desired 200 to 300 Lb/in range while providing more energy absorption than the empty cells. Of the foam filled specimen it was concluded that the specimen with 2.4 X 1.0 inch cell configurations (B1.3 through B1.5 in table A-3.1) provided the best overall EA characteristics and are the best candidates for use in a keel beam web. For this reason this configuration was chosen to be modeled and. Of these configurations specimen B1.4 with a $0/90^0$ glass cell lamina and a $\pm 45^0$ kevlar face sheet lamina had a SCL of 252 Lb/in and

a CIL of 593 Lb/in. The SCL is in the midrange of desired SCL values while the CIL is large enough to support a maximum 3 to 4 g inflight load. Since its EA characteristics fall in the midrange of desired values it was chosen to be modeled first.

3.3 Modeling Technique

The B1.4 specimen and crush fixture geometry were created using SDRC Ideas Master Series® software to facilitate automatic meshing. The test specimen was drawn as a 12. X 8. X 1. in. [305. X 200. X 25. mm] solid. The solid was partitioned into five (5) 2.4 X 8. X 1. [60. X 200. X 25. mm] volumes. The volumes were used to create the foam mesh while the surfaces on the sides of the volumes were used to create the laminate mesh surrounding the foam.

A simplified geometry was used to represent the crush fixture in order to simplify meshing and reduce solution cost. The guide rods were eliminated since they could be represented with nodal restraints. The impact mass, support platen and knife edge supports were simplified to surfaces that were used to create planar elements. These parts could be reduced to surfaces since their planar elements could be specified to have equivalent mass and stiffness characteristics. The size of the impact and support platen surfaces only needed to be large enough so that the specimen did not deform beyond its edges as this would have allowed the specimen to 'flow' around it. The specimen and crush fixture geometry is shown in figure B-3.2 . Eliminating the guide rods and using

surfaces to represent the impact mass, support platen and knife edges not only simplified meshing but also resulted in computational time savings of the impact simulation since fewer, simpler elements are used.

The PVC foam filling the cells was modeled as an isotropic solid. To represent the foam's isotropic solid behavior the cell volumes were meshed with iso-parametric 8 noded solid elements with a standard brick element formulation as presented in chapter 2. The glass/epoxy lamina wrapping the foam and the kevlar/epoxy lamina used as face sheets were modeled as a laminate. To represent the glass/kelar/epoxy laminate the surfaces on the sides of the cell volumes were meshed with iso-parametric 4 noded quadrilateral laminate elements with the Belyschko-Tsay formulation [1] discussed in chapter 2. The elements lay-up specification was varied as necessary to represent the glass/kevlar/epoxy face sheet laminate and all glass/epoxy laminate between the foam filled cells.

The laminate elements were joined to the solid elements through shared nodes to enforce displacement continuity and strain compatibility. The laminate mesh was made identical to the solid mesh so that the nodes could be merged forcing the elements to share common nodes.

The impact mass, support platen and knife edge supports were modeled with iso-

parametric 4 noded quadrilateral elements. These elements were assigned properties of steel. Due to steel's higher modulus the support platen, knife edge supports and impact mass behaved rigidly in comparison to the specimen. The only response of interest for these parts was their rigid body movement. The impact mass movement should be vertically downward while the others remained stationary. This was accomplished through nodal restraints applied to the element nodes.

The specimen and crush fixture mesh was transported into MSC/Dytran™ software where the element formulations, material constitutive relations, failure models, test kinematics and impact dynamics were defined and the impact simulation performed. The solution results were postprocessed in MSC/Patran® and MSC/X-dexter®.

3.4 Model Kinematics

Only the impact event and subsequent crushing of the specimen was simulated with the finite element model. The free fall portion of the test was not simulated to save computer solution time. To simulate the impact event without free fall, the impact mass was modeled as being .002 in (.05 mm) above the specimen with a velocity of 92.5 ft/s (28.2 m/s).

The kinematics of the test specimen at impact and during crushing was controlled by its interaction with the crush fixture's support platen, impact mass and knife edges. The

support platen restrained the specimen from vertically downward motion after impacting the pulse generator. Friction between the specimen and platen also provided some lateral and longitudinal restraint at their interface. The knife edges provided lateral restraint but allowed the specimen to slide downward along their edge. This forced the specimen to maintain a vertical orientation during crushing. The knife edges cut into the specimen skin due to folding that occurred during crushing thereby providing some longitudinal restraint as well. Figure B-3.3 show cuts into the folded skin made by the knife edges. Fixture guide rods constrained the impact mass to strike the specimen square and restrained it from rotating thus forcing it to crush the specimen through vertical movement only. The specimen was free to flare outward and slide along the impact mass face as crushing occurred.

The interaction of the specimen with the support platen, knife edges and impact mass was represented with contact surfaces in the model. The representation of contact between the specimen and these supports required definition of master surfaces and slave nodes. The thinshell elements representing the support platen, knife edges and impact mass were defined as master faces through which slave nodes could not pass. The element master faces of each part were grouped together to comprise a master surface for that part. The specimen laminate and solid mesh nodes adjacent to these surfaces were defined as slave nodes. The master surface produced a normal restoring force and an in-plane friction force when a slave node penetrated the surface defined by its master faces. This

accurately represented the fixture kinematics as the support platen, knife edges and impact mass constraint forces acting on the specimen were normal to their surface and the frictional forces acted in the plane of their surface. The direction of the contact surface friction forces were opposite in direction of the nodal displacement vector's projection onto the master face with a value equal to its coefficient of friction (user specified) times the restoring force. The coefficient of friction was not known for kevlar on steel thus a value of .2 was used to approximate the friction force acting between the specimen and fixture.

The mesh comprising the master surfaces was made much more coarse than the slave mesh to prevent the slave mesh from penetrating the master surface. The Dytran's contact algorithm checks for slave node penetration into the master surface only. A slave surface that could be checked for master node penetration does not exist. As a result the slave mesh could penetrate the master surface if it is more coarse than the master mesh. This is illustrated in figure B-3.4 .

The knife edge supports could not be modeled as line contacts due to the master/slave relation mentioned above. Ideally the knife edge would be modeled as a mesh perpendicular to the specimen and identified as a master surface with specimen nodes near the knife edge specified as slaves to the master surface. However due to the thinness of the knife edge where it contacts the specimen, slave nodes would miss the portion of

the contact surface facing the specimen due to small longitudinal displacements that occur during crushing. This is illustrated in figure B-3.5 . Alternately the specimen sides could be specified as the master surface and knife edge nodes identified as slaves. However in this configuration the folds of the specimen developed during crushing would penetrate the knife edge as shown in figure B-3.4 since the master nodes are not checked for penetration into the slave mesh. If the knife edge mesh was made extremely fine to minimize such penetration the restoring forces for this configuration would be normal to the folded specimen faces thus producing upward and downward restoring forces rather than forces normal to the knife edge. As a result, the knife edges had to be modeled as elements parallel to the specimen. These elements were specified as master faces and grouped to construct the master surface. A mesh width of .31 in (8.0 mm) was arbitrarily specified to provide sufficient width for nodal contact. To ensure the specimen nodes contacted the knife edge surface, the specimen was meshed such that rows of nodes were located across from the centerline of the knife edge master surfaces. These nodes were identified as slaves to the knife edge master surfaces.

To reduce computational cost, contact was defined to occur on one side of the master surface only as was the case for the crush fixture supports. This allowed the software to monitor nodal displacement only on one side of the contact surface. In Dytran the element normal defines a top side of the element and is used to identify on which side contact would occur. All support plates, knife edge and impact elements were defined

such that their normals pointed away from the specimen. Thus contact was defined to occur on the element's bottom side. Damping was also applied to the slave node high frequency response to reduce vibrations due to impact. Damping is based on the relative velocity of a slave node with respect to the master surface. This damping force reduces high frequency vibrations that result from impact and smooths solution force/acceleration results for easier interpretation.

The rigid support provided by the support platen and knife edges were simulated by restraining translations and rotations of the master surfaces representing them. Their master surfaces were restrained by applying nodal restraints in the X, Y, Z translations and X, Y, Z rotations to the element nodes that define their master faces. In the test the support platen did have some vertical movement after striking the pulse generator in order to produce the desired acceleration profile, however it was small. Thus, the support platen was approximated as being fixed in the model. The impact mass guide rods that allowed only vertical movement were also simulated by nodal restraints. Nodal restraints in X, Y translation and X, Y, Z rotation were applied to nodes of elements making up the impact mass master surface to prevent it from translating laterally or longitudinally and to prevent it from rotating about any axis. These restraints forced the impact mass to maintain an orientation parallel to the support platen and crush the specimen through vertical movement only as in the test fixture.

Nodal restraints were applied to the test specimen as well to prevent it from being unconstrained prior to contacting the contact surfaces. The contact surface definitions required that a gap exist initially between the slave nodes and master surfaces or that they be coincident. This resulted in the specimen being unconstrained and free to translate or rotate at the start of the solution. Translational restraints in the X, Y and Z directions were applied to the specimen's four lower corner nodes to stabilize it until contact was made with the support platen and knife edges. The initial gaps between the specimen and all contact surfaces were specified as being .002 in (.05 mm). With a gap this small the Z restraints used to initially stabilize the specimen had little effect on the force distribution along the bottom of the specimen during crushing.

The folding of the specimen sides that occurred during crushing forced the sides of the specimen to come in contact with itself. This contact provided a force path into the uncrushed portion for further crushing. Folding contact was represented by Dytran's single surface contact. For single surface contact, the specimen laminate mesh was defined as slave segments with no master surface. The slave segments could not penetrate themselves once folding resulted in contact. Preventing the mesh from penetrating itself provided a force path through the folds and into the uncrushed material as in the specimen. A sketch of the single surface contact surface is shown in figure B-3.6 .

Obtaining an accurate simulation of the specimen kinematics with Dytran's contact

surfaces was difficult to achieve. Friction had to be specified between the specimen mesh slave nodes and impactor master surface for numerical stability. Initially, no friction was specified since it represented a negligible portion of the energy absorption. However without friction the top layer of solid element nodes moved laterally inward significantly as they moved downward from the impact. This motion essentially flattened and then turned the element 'inside out' as shown in figure B-3.7 . The reason for such pronounced lateral movement was not known. The impact mass was constrained to strike the specimen square; thus no lateral velocity components should have been imparted. In addition, Poisson's effect should have forced the nodes outward. A numerical instability arising from the impact was concluded to have caused the problem. Specifying friction between the impact mass master surface and slave nodes corrected the problem. Static and sliding friction coefficients of .2 were used.

Another difficultly in obtaining proper kinematic response involved the knife edge contacts. The knife edge contact surface did not restrain the specimen as defined initially. The specimen laminate mesh nodes specified as slaves to the knife edge contact surfaces had to be restrained from X translation in order to prevent them from missing the contact surface. The .31 in (8.0 mm) width of the contact surface and .002 in (.05 mm) initial gap between the slave nodes and master surface were thought to be sufficient to ensure contact. However, upon running the simulation, the specimen passed through the knife edge contact surfaces after impact and essentially fell over on its side. It was surmised

that the laminate nodes were translating longitudinally; thus, restraints were added to all knife edge slave nodes to ensure that they did not miss the contact surface. The restraints did force the slave nodes to come into contact with the master surfaces, however intermittent penetration of contact surfaces occurred. Figure B-3.8 shows intermittent penetration occurring. Factors effecting the contact surface restoring force were manipulated in an effort to prevent penetration. By default the contact force is multiplied by a weight factor of:

$$M_{scale} = \frac{M_m M_s}{M_m + M_s}$$

where M_{scale} is the restoring force mass scale factor, M_m is the mass of master surface elements and M_s is the mass of slave node elements. Due to the low mass of the foam and laminate it was changed to

$$M_{scale} = M_m$$

This improved the surface performance but some penetration still occurred. To prevent any penetration from occurring an overall scale factor for the contact force was also increased. Dytran's default value of .1 was increased to the maximum allowable value of .5. Again, penetration occurred. The knife edge contact surfaces had to be specified as being rigid rather than having properties of steel in order to prevent penetration by the specimen.

The support platen contact worked well as initially defined. Once the impact mass and

knife edge contact surfaces were modified as described, the model properly simulated the kinematics of the specimen during crushing.

3.5 Model Dynamics

The energy stored in the impact mass from its free fall in the drop tower was simulated in the model by assigning a kinetic energy to the impact mass equal to 1342 ft-Lb (1820 J). With properties of steel the mass of the impact mass mesh was 10.09 Lb_m (4.57 kg), thus a velocity of 92.5 ft/s (28.21 m/s) was assigned to it at $t = 0$ as initial conditions. The impact mass traversed the .002 in (.05 mm) gap and impacted as the solution progressed through time. The velocity of the impact mass was reduced to zero over time as the specimen absorbed its energy through strain energy, kinetic energy and permanent deformation energy.

Note that the impact mass mesh was a dummy mesh to provide a surface against which to crush the specimen. It was arbitrarily modeled as a 13.25 x 2.75 x1.0 in (335 x 70 x 25 mm)volume and was assigned properties of steel which gave it a mass of 10.08 Lb_m (4.57 kg). The mass of the impact mass mesh could have just as easily been specified by solving for a density that would give a kinetic energy equivalent to the absorbed energy for the test impact velocity of 28.3 ft/s (8.63 m/s). This approach wasn't used since the mass is used in scaling the contact force. An arbitrarily high mass would result in large contact forces. The velocity does have some effect on crushing behavior but rate effects

are small. Farley studied rate effects and found that the velocity effects are only significant if the crushing material has rate dependent elastic properties and significant damping, Farley [5]. The velocity should, however, be kept within an order of magnitude of the actual impact velocity to prevent large inertia forces from developing that artificially increase the specimen crushing force.

Chapter 4

Material Properties

4.1 Standard Property Values

Standard steel elastic properties were used for the impact mass, knife edge supports and support platen. These properties are listed in tables A-4.1 and A-4.5 . The PVC foam mass and elastic properties were available from NASA Langley researchers and are also listed in tables A-4.1 and A-4.5. The foam's compressive stress-strain relationship and Poisson's ratio as a function of strain are shown in figures B-4.1 and B-4.2 respectively.

The elastic and mass data for the $0/90^0$ glass/epoxy and $0/90^0$ kevlar/epoxy fabric lamina were not available from NASA researchers when the specimen was initially modeled at Langley Research Center. Elastic and mass values for unidirectional .55 fiber volume glass/epoxy and .60 fiber volume kevlar/epoxy lamina were obtained from Daniel and Ishai [4] and used in their absence. Their unidirectional elastic values are listed in tables A-4.1 and A-4.2. The $0/90^0$ fabric was represented as two unidirectional lamina oriented at 0^0 and 90^0 in the laminate definition of the elements. Dytran's orthotropic constituitive relation does not distinguish between tensile and compressive moduli, but rather assumes them to be equal. It does distinguish between tensile and compressive strengths. Dytran's orthotropic strength values are stress based rather than strain based. Values for tensile

and compressive strengths in the longitudinal (1) and transverse (2) directions were also obtained from Daniel and Ishai [4] for .55 fiber volume glass/epoxy and .60 fiber volume kevlar/epoxy for initial use in the model. These strengths values are listed in tables A-4.4 and A-4.8. Model results showed that the CIL and SCL differed from test values by 190% and 48% respectively. The elastic properties of unidirectional lamina were thought to be partially responsible, thus, testing to determine the fabric properties was performed.

4.2 Material Property Testing

Uniaxial tensile stress/strain testing to determine the actual glass/epoxy and kevlar/epoxy $0/90^0$ fabric elastic properties was conducted in an effort to improve the modeling accuracy. Two 16 x 16 in sample sheets, each of the glass/epoxy and kevlar/epoxy material, used in the specimen were fabricated at Langley's composite layup shop from which coupons were cut. The sample sheets consisted of four .01 in $0/90^0$ satin weave fabric lamina (harness count not given) laminated together through a wet layup technique like that used in constructing the specimen. No target fiber volume ratio was given for the layup, but their appearance indicated a 'dry' layup. The glass appeared to have a .55-.60 fiber volume while the kevlar appeared to have a fiber volume of .65-.70. No tests were conducted to determine fiber volume. Coupons were cut from the sheets in the longitudinal, transverse and 45^0 directions. The fiber direction in the sheet was not perfectly straight, but had some waviness as is typical in hand lay-up. The major fiber directions in the sheets were identified by "eye average" and used to lay out the coupons

on the sheet. Since the fabric was a $0/90^0$ weave, the choice of longitudinal and transverse direction was arbitrary. 1.0 x 7.0 in coupons were laid out on the sheets in a pattern to give approximately 5 longitudinal coupons, 5 transverse coupons and as many 45^0 shear coupons as possible. Figures B-4.3 through B-4.6 illustrate the coupon layout on the sheets and identify areas of lay-up inconsistency. The shear coupons were laid out at $+45^0$ and -45^0 directions when possible to account for any biasing in fiber direction that may have arisen from fiber misalignment/variation in the lay-up. ASTM test standard D3039 specifies a coupon size of 1.0 x 10.0 in. However, 1.0 x 7.0 in coupons were used on the recommendation of NASA test engineers to get as many coupons as possible. Note that this reduced the ASTM recommended gage length. The coupons were cut from the sheets using a diamond wheel cutter in the NASA machine shop. This gave a straight, clean cut for the glass/epoxy samples. However, due to the toughness of the kevlar fiber, the kevlar/epoxy coupons had slight fiber fraying along the edges. Tabs for transferring the test machine grip clamp force into the specimen were not epoxied to the coupon ends as specified in ASTM D3039. NASA test engineers instead recommended an emery cloth wrap on the ends. With this arrangement the coupons had a gage length of 4.38 in.

ASTM D3039 specifies that the coupon dimensions be measured in several places and used to determine the minimum area. The kevlar/epoxy and glass/epoxy coupon dimensions were measured at their center and ± 1.0 inch from the transverse centerline. Figure B-4.7 shows the layout of a coupon and the points at which measurements were

taken. The measurements and computed areas for glass/epoxy and kevlar/epoxy coupons are listed in tables A-4.9 through A-4.12.

ASTM D3039 specifies that the variation in coupon width be within ±1% of the nominal value and the thickness be within ±2 % of the nominal value. From the tabulated coupon dimensions it was determined that the variation in coupon width was around .2 % which was well within the limit. The coupon thickness had a variation of 2.5% which is slightly greater than the limit. The thickness variation was attributed to variation in the fiber volume ratio. In a wet hand lay-up the fiber volume ratio can vary depending on how well the fiber mat is saturated with the matrix during lay-up.

The coupons were instrumented with longitudinal and transverse strain gages to measure strain as a function of stress. Micro-Measurements type CEA-06-250UW-350 strain gages were used. The strain gages were 350 ohm gages with gage factors of 2.08. Strain gages were bonded to coupons using Micro-Measurements M-Bond 200. The gages had a linear strain range of 5% strain when bonded with this adhesive. The strain gages had a regulated 2.0 volts applied across them supplied by a Lambda power supply. The strain output was amplified by an NEF 122 strain gage amplifier. A gain of 20 was used for longitudinal gages while a gain of 50 was used for the transverse gage. A higher gain was used for the transverse gage due to transverse strains being much smaller than longitudinal strains. The coupons were tested under uniaxial loading in a Tenius-Olsen 10.0 kLb

tension/compression test fixture. The Tinius-Olsen fixture was equipped with a load cell that measured applied load and a micrometer that measured displacement. The load value along with the coupon area was used to calculate a stress-strain relationship. The load cell range was set to 5.0 kLb for longitudinal and transverse coupons and 2.0 kLb for shear coupons. Coupons were pulled at a constant crosshead speed of 1.0 in/min. The displacement range was set to 2.5 inch for longitudinal and transverse coupons and 5.0 inch for shear coupons. Figures B-4.8 through B-4.10 show the test apparatus setup.

Data acquisition was performed by National Instruments LabView™ software running on a Macintosh PC at a sampling rate of 100 samples per second. LabView™ processed and manipulated the load and strain data in real time using programming referred to as virtual instruments. The virtual instrument has a graphical interface where the coupon area, load cell range, displacement range, gage factor and calibration voltage (Rcal) are entered. These values are used in the program to compute stress, longitudinal strain, transverse strain and Poisson's ratio from the test equipment voltage signals at each sampling. Computed values are stored in an ascii text file for later manipulation. Figure B-4.11 shows the LabView™ interface. Figures B-4.12 through B-4.17 show longitudinal, transverse and shear failures representative of glass/epoxy and kevlar/epoxy coupons.

Corel® Quattro® Pro was used to read the coupon data files, put the data in spreadsheet form and plot stress-strain curves. Figures B-4.18 through B-4.23 show typical

longitudinal, transverse and shear stress-strain curves for the glass/epoxy and kevlar/epoxy coupons. All longitudinal and transverse glass/epoxy coupons showed a linear stress-strain response to 10 kpsi. Beyond 10 kpsi the stress-strain curve showed a slight but continuous decrease in slope until failure occurred near 2% strain. This behavior is highlighted by curve fits in Figure B-4.24. The change in modulus was caused by fiber failures beginning to occur near 10 kpsi and continuing until catastrophic failure near 2% strain. All longitudinal and transverse glass/epoxy coupons exhibited a brittle type failure near 2% strain. The glass/epoxy shear coupons exhibited a linear stress-strain curve to approximately 1.75 kpsi followed by a pronounced continuous drop in slope until failure occurred. Their failure strains exceeded the strain range of the gages thus the stress-strain curve is not accurate in the area of failure. From the graph the stress-strain curve appears to be accurate up to 6% strain. The pronounced drop in shear modulus occurred due to the weaker epoxy matrix failing which allowed the fibers to slide relative to one another and become more aligned with the load. The angle between the fibers was reduced thus producing shear strain as the fibers aligned themselves with the load. This effect is sometimes referred to as fiber scissoring.

The kevlar/epoxy longitudinal and transverse coupons showed a very slight bilinear behavior. The slope of the stress-strain curve changed slightly around 16 kpsi, but unlike the glass/epoxy coupons, the slope remained linear until failure around 1.75 % strain. The slight change in longitudinal and transverse modulus may have been caused by fiber

failure along the coupon edges due to fraying during cutting or due to surface fibers failing from damage resulting from tabs not being used to evenly distribute the load into the coupon. All the longitudinal and transverse kevlar/epoxy coupons exhibited a brittle type failure around 1.75% strain. The kevlar/epoxy shear coupon behavior was very similar to the glass/epoxy shear coupons. The coupons exhibited a linear shear stress-shear strain response to around 1.5 kpsi followed by a continuous and pronounced drop in shear modulus. Their behaviors are similar since the failure mode is the same, i.e., epoxy matrix failure allowing fiber scissoring. As with the glass/epoxy coupons the shear stress-shear strain curve is only accurate to around 6% strain due to the gage strain range being exceeded and gage debonding due to fiber scissoring.

The coupon stress-strain data was curve fit using first order least squares fits. The glass/epoxy longitudinal and transverse coupons stress-strain response was represented as being bilinear with straight line fits from 0 to 10 kpsi and 10 kpsi to failure. The slope of their stress-strain curves was continuously decreasing above 10 kpsi, but the decrease was small enough that straight line fits were sufficient. The kevlar/epoxy longitudinal and transverse coupon stress-strain bilinearity was so slight that they were represented as being linear with straight line fits from 0 kpsi to failure. The glass/epoxy and kevlar/epoxy shear coupons shear stress-shear strain response was represented over their linear portion only with straight line fits. No attempt was made to curve fit the data once fiber scissoring began. The slope coefficient of each longitudinal and transverse coupon curve

fit was taken as its longitudinal and transverse modulus of elasticity. In the case of a coupon with bilinear response, the intersection of the two curve fits was computed and identified as its yield strength and the slope coefficient for each region was taken as the modulus over that region. The initial linear response from 0 to 10 kpsi was designated as region A and the response from 10 kpsi to failure was designated as region B. The slope coefficient of each shear coupon curve fit was taken as its shear modulus.

Poisson's ratio for each longitudinal and transverse coupon was determined as the average of Poisson's ratio values computed by LabView™ at each sampling point. Each coupon's ultimate strength and ultimate strain was determined from its data file.

The computed elastic and strength properties of each coupon are summarized in tables A-4.13 through A-4.24. The elastic and strength properties of coupons from both sample sheets were averaged. The mean values were used to represent the material property in the model. Since the kevlar/epoxy fabric and glass/epoxy fabric were $0^0/90^0$ weave the longitudinal and transverse properties are theoretically equivalent. Thus longitudinal and transverse were averaged to give one elastic modulus. The glass/epoxy coupons had bilinear response a yield strength was defined as being the stress at which the change in slope occurred, approximately 10 kpsi (68.9 Mpa), and a plastic modulus, E_H, defined as being the slope of the least squares curve fit from yield to failure. The kevlar/epoxy coupons were not defined as having a yield strength and plastic modulus since they did

not have a significant bilinear response. The averaged propeties are given in tables A-4.25 and A-4.28.

Note that the glass/epoxy region A and B average longitudinal moduli differed from the average transverse moduli by 2.4% to 5% with sheet 1 having the greater variations. The variation was thought to be the result of some misalignment of the fiber directions between the 0/90 lamina. Differences in the glass/epoxy longitudinal and transverse ultimate strength were 13% for sheet 1 while for sheet 2 the strengths differed by 1.8%. The larger difference in sheet 1 strengths were due in part to its greater fiber misalignment but a variation in matrix content due to poor fiber 'wetting' must also have been present for such a large difference. Overall sheet 2 had more uniform and higher properties. The kevlar/epoxy properties were more uniform than the glass/epoxy. The longitudinal modulus differed from the transverse between 1.1% and 3.0%. The longitudinal ultimate strength differed from the transverse strength between 2.7% and 3.5%. Sheet 2 had more uniform and higher properties than sheet 1.

The fabric properties were significantly different from the uniderictional lamina properties listed in Ishai and Daniel [4]. The glass/epoxy fabric modulus was half that of the unidirectional lamina while the kevlar/epxoy fabric modulus was about one fourth that of the unidirectional lamina. These large variations should have resulted in significant differences between test and model results.

Chapter 5

Model Solution, Results, Correlation and Modification

5.1 Model Solution

The dynamics of the specimen resulting from impact was simulated by solving the finite element model over a 30 millisecond interval using an initial time step of 1.0E-7 seconds. Dytran automatically adjusted the time step up or down as the model elements deformed. The adjustment was based on the previous time step's smallest element using the Courant criteria. The initial model was analyzed using unidirectional lamina elastic properties as discussed in section 4.1 in the absence of fabric lamina properties. To interpret the model response to impact, solution results were saved at specified time intervals. Selected results could then be plotted as a function of time to produce time history plots of results. The following results were stored at time intervals of 1.0E-6 seconds:

- total X, Y, Z force acting on contact surface
- X, Y, Z displacement of contact surfaces and specimen nodes.
- acceleration magnitude of contact surface
- x, y stress in layers of laminate element.

The impact mass contact surface Z forces were saved to construct a crush force time history from which the specimen CIL and SCL could be determined. Its contact surface displacement was saved to produce a crush force versus crush displacement plot from

which energy absorption could be computed. The force/displacement data also provided a means of producing a crush force vs. crush stroke plot for comparison to test plots. The knife edge and support platen contact surface forces and displacements were saved for model checking. The impact mass contact surface acceleration was saved to construct a time history of its acceleration for comparison to the typical acceleration/time response obtained from testing. The specimen nodal displacements were saved to determine deformation occurring in the specimen. These deformations could then be used to compute crush efficiency. The element stresses were saved to provide an indication of stress distribution and to provide an indication of stress wave propagation through the specimen. The remaining stress resultants for the laminate and solid elements were stored at time intervals of 5.0 E-5 seconds. Saving the remaining stress resultants at a reduced time interval reduced hard disk storage requirements. Also saved was the time at which individual elements failed. When an element's stresses met its failure criteria a flag was set indicating it had failed and the time of failure recorded. The element failure time provided a means to interpret the effect of crushing over time. The element failure time was stored at the last time step.

5.2 Model Results

A plot of the impact force versus time is shown in figure B-5.1. The force peaked at 75 kN and oscillated near that value for approximately 4E-5 seconds after which it quickly dropped to zero. The oscillations were a result of intermittent contact with specimen

nodes. The specimen nodes penetrated the contact surface and were accelerated away from it due to its restoring force. The nodes separated slightly from the contact surface due to the acceleration and the force dropped. The elemental stiffness decelerated the nodes after contact was lost and the drove them back into the contact surface where the process was repeated. The force dropped to zero as a result of element failure. Figure B-5.2 shows the kevlar stress distribution at t = .2 ms by which time the force had dropped to zero. White indicates element failure in the plot (stiffness properties reduced to zero and element removed from calculation). The entire bottom layer of elements had failed by .2 ms. The failure was due to shearing in the kevlar lamina. The kevlar lamina was oriented at $^{+}/- 45^{0}$ to the impact load which resulted in shear stresses being developed at impact. For compressive loads, kevlar/epoxy strengths are least in shear thus a shear failure resulted. Element failure occurred along the bottom layer of elements due to stress wave reflection. The specimen was semi fixed along its interface with the support platen due to friction. For fixed end conditions stress waves reflect with the same sign thus adding to the stress state produced by the wave prior to reflection. Since the specimen wasn't totally fixed the stress didn't double upon reflection but it did add to a value sufficient to produce failure.

Element failure as a result of stress wave reflection can be more clearly seen in a plot of element stress versus time. Figure B-5.3 shows a plot of stress for the glass/epoxy lamina in an element at the support platen interface. The lamina stress was zero for

approximately 5.0E-5 seconds after which it built to a value of 30 Mpa and failed around 6.5E-5 seconds. Following failure the stress ramped back down to zero and remained there. The ramp down in stress was a result of Dytran's representation of post failure behavior where lamina stiffness properties are degraded over 200 time steps following failure and element failure occurs after all lamina have failed and their properties are ramped to zero. Note that glass/epoxy lamina stress versus time was plotted since it fails after kevlar due to slower stress wave propagation thus determining when element failure occurs. This behavior agrees with an estimation of stress wave propagation in glass/epoxy as shown.

$$v = \left[\frac{E}{\rho}\right] = \left[\frac{39.E3}{2.1E-9}\right] = 4.31E+6 \ \frac{mm}{s}$$

$$t_{bottom} = \frac{200.}{4.31E+6} = 4.64E-5 \ s$$

The estimation shows that stress should have begun to build as shown in the graph with reflection occurring shortly thereafter, thus increasing the stress above the glass/epoxy strength and producing failure.

The design intent of the laminate elements that wrapped the foam was to contain the foam and prevent it from flowing thus producing high compressive strength. The failure of these elements freed the foam to flow thus reducing the specimen stiffness to near zero. The load path into the platen was essentially eliminated and the specimen became free to translate resulting in the crush load dropping to a value equal to that of the inertia force

accelerating the specimen downward.

By .5ms after impact large areas of foam and laminate elements had failed as shown in figure B-5.4. These failures were a result of stress wave propagation back up the specimen. Due to these failures the restraint provided by the knife edge supports and support platen was eliminated and it became unconstrained resulting in invalid results.

5.3 Model Correlation

The specimen force time history shown in figure B-5.1 indicated that its CIL was 75. kN and that it provided no SCL. The model CIL exceeded the test value by 137%. The model SCL is invalid due to the premature failure. No other EA parameters could be calculated due to the premature failure. No correlation existed between the model and test specimen.

5.4 Model Modifications

5.4.1 Perturbed Geometry

The laminate failure was due to in-plane stresses in excess of the Tsai-Wu failure criteria being developed at impact before buckling could occur. The specimen crushes as a result of its laminate sides buckling into a high order buckling pattern. An investigation into Dytran's solution technique revealed that buckling isn't specifically solved using an eigenvalue approach. Instead small imperfections in the mesh either user created or

induced by numerical roundoff are relied upon to produce moments and out of plane forces that result in out of plane deformation and buckling. The specimen geometry created in SDRC was planar with no imperfections. Thus out of plane forces/moments were produced by imperfections due to nodal coordinate round-off error. Nodal coordinate round off error was extremely small thus extremely large in-plane force had to be developed before buckling would be initiated. The stresses resulting from in-plane forces met the Tsai-Wu failure criteria before the in-plane forces were large enough to initiate buckling that would allow the specimen to crush and stop the growth in in-plane stress.

The specimen geometry was perturbed to produce out of plane imperfections that would initiate buckling before the laminate stresses satisfied the failure criteria. Slight perturbations on both sides of the specimen were created by displacing a row of nodes .04 in (1 mm) outward. One longitudinal and two vertical perturbations were created on each side of the specimen as shown in figure B-5.5. The vertical perturbations were added to initiate buckling that may arise from restraining longitudinal expansion, due to Poisson's effect, with the nodal restraints at the knife edges.

A plot of the perturbed geometry impact force versus time is shown in figure B-5.6. Surprisingly perturbing the geometry had no effect on the peak force or its decay. Only the duration of the peak load was effected, being reduced 50% to approximately 2E-5 seconds. As with the planar geometry, element failure occurred along the bottom of the

specimen resulting in the force decaying to zero. Figure B-5.7 shows the kevlar lamina stress distribution at 2E-4 seconds with white indicating failed elements. Note that the perturbed geometry had very little effect on the stress distribution. This indicated that the stress wave passed across it before enough out of plane straining could occur to reduce stiffness. Figure B-5.8 shows the stress distribution at 5.E-4 seconds. By this time the line of perturbed nodes had resulted in buckling. However, prior to buckling the stress wave had reflected and caused a significant amount of element failures.

It was expected that perturbing the geometry would significantly reduce the peak impact force by providing a means of out of plane deformation that would reduce its stiffness. Impact force is a function of the impacting bodies stiffness and damping. Damping wasn't included in the specimen material models thus stiffness could be used to give an indication of relative impact force. The apparent stiffness increases as impact velocity increases. However static stiffness will give an indication of relative impact stiffness. Thus an investigation into the static stiffness of the planar and perturbed geometry was made to determine if there was a significant difference in stiffness that would lower the impact force. A .04 in (1 mm) vertically downward displacement was imposed on the top layer of nodes and the total Z reaction force calculate from which a static spring rate was determined. The planar specimen had a static spring rate of 382.5 kLb/in (67.0 kN/mm) while the perturbed specimen had a rate of 306.1 kLb/in (53.6 kN/mm). The perturbations reduced the static stiffness 19% thus the perturbed specimen should have had a smaller peak impact force. Figures B-5.9 and B-5.10 show the planar and perturbed

geometry static stress distributions for the .04 in (1 mm) displacement respectively. Stresses concentrate at the ends of the planar specimen indicating more load is carried there. The perturbed geometry stresses concentrate around the perturbation and are 123% larger than the planar geometry maximum stress. The higher stress magnitudes indicate buckling should initiate sooner than that of the planar specimen. As was seen in figure 5.8 buckling did occur at the perturbations.

The position of nodes along the top of the specimen was plotted over time to determine the displacement occurring at impact. These displacements are shown in figures B-5.11 and B-5.12 . From the graphs it is seen that both the planar and perturbed specimen compressed at a constant rate of approximately 985 $^{in}/_{s}$ (25E+3 $^{mm}/_{s}$). Both specimen had compressed .02 in (.5 mm) at 1.0E-4 seconds when their peak force was reached. The planar and perturbed specimen peak impact forces exceeded their static force-displacement relationship by 123% and 180% respectively. In addition, their impact force had relatively constant mean values (mean of oscillations) over .04 in (1 mm) of displacement. The differences in force values and violation of force displacement relationship indicated that other factors contributed to the resistive force. It is recognized that the dynamic stiffness is different than the static stiffness due the entire specimen not being uniformly stressed at impact as a result of stress-strain wave propagation and inertia effects. A better approximation could be made based on a shock wave analysis. However the static estimation provided a 'quick and dirty' indication

The impact mass acceleration time history was investigated to determine inertia effects. Figures B-5.13 and B-5.14 show the impact mass acceleration versus time when impacting the planar and perturbed specimen respectively. The impact mass had a peak acceleration of 1.8E+8 $^{in}/_{s2}$ (4.5E+9 $^{mm}/_{s2}$) for both specimen. The impact mass acceleration trend over time was nearly identical to the force trend. They appeared to differed by a scale factor only. This is as it should be since the force is calculated from the relation f=ma.

It was concluded that inertia forces due to the extremely large acceleration magnitude dominated the specimen impact force relationship. A rough calculation of the inertia force due to impact acceleration showed that it was 25 times the stiffness force at .02 in (.5 mm) deflection. The acceleration magnitudes predicted by the model are unrealistically high. They were thought to be a result of the contact surface restoring force calculation technique . The actual equation for calculation of restoring force is not given in Dytran's manual just a general description of parameters that influence it is given. It was believed that the magnitude of penetration occurring over one time step at the initial time of contact along with the number of nodal penetrations contacted resulted in the unrealistically high acceleration. Note that the impact mass was constrained to move parallel to the specimen top face thus 144 nodes simultaneously penetrated its contact surface. To verify this the maximum time step was reduced by a factor of 10 and 100. Reducing the time step reduced the impact force magnitude 7% to approximately 70 kN. This implied that excessive penetration at initial contact did not occur and that it was not

the cause of the excessive acceleration. Since the unrealistically large acceleration resulted in a stress wave that failed the laminate material after one cycle, the manner in which the impact was modeled had to be changed before crushing could be simulated.

5.4.2 Impact Modification and Material Properties Update

Several changes were made in how the impact was modeled. Rather than have the impact mass free fall onto a rigidly supported specimen the specimen was accelerated according to the acceleration pulse produced by the test fixture pulse generator upon impact. The specimen with the impact mass resting on its top was accelerated upward by the support platen contact surface. The definition of the pulse was obtained from Kellas's report [8] and is shown in figure B-5.15. Only the initial acceleration peak that lasted for 11 ms was modeled. The 11 ms acceleration profile was approximated by a linear ramp from 0 to 250g over 5ms, a constant 250g for 1ms and a linear ramp back down to 0g over 5ms. The approximation is shown in figure B-5.15 . Modeling the impact in this manner better represents the actual test dynamics described in section 3.1. A velocity profile obtained from integrating the acceleration pulse had to be prescribed for the support platen nodes since Dytran did not have a means to prescribe nodal accelerations directly. Figure B-5.16 shows the velocity profile while table A-5.1 gives the time-velocity data pairs entered in Dytran to describe the profile.

The impact mass was rotated 1.5^0 to prevent simultaneous penetration of all top surface nodes and to induce an out of plane force that would initiate buckling. Reducing the

number of penetrations served to lower the initial impact force by lowering the restoring force generated by the contact surface. Buckle initiation due to out of plane force was intended to prevent in-plane forces and stresses from building to unacceptably large magnitudes.

The kevlar/epoxy fabric lamina and glass/epoxy fabric lamina elastic properties were available at the time of these modifications. Thus the laminate elastic properties were updated as a part of the modifications. The stacking sequence of the laminate was also changed to that of the fabric lay-up. Initially two unidirectional lamina were used to represent the one fabric lamina.

These modifications improved the model's prediction of the crushing behavior. Large numbers of elements did not fail as a result stress wave reflection. Rather the stresses built over time until elements along the interface with the impact mass failed. Figure B-5.17 shows the impact force time history. The impact force reached a peak magnitude of 12.5 kN at 2.5 ms. The impact force reached its maximum value prior to the applied acceleration peak due to element failure beginning to occur at 2.5 ms. The failures resulted in the sharp drop in impact force. Figure B-5.18 shows the kevlar/epoxy shear stress approaching its shear strength of 1.55 (11.0 Mpa) along the interface with the impact mass at 2.5 ms. Figure B-5.19 shows the stress history of an element in contact with impact mass. Element failure occurred at 2.5 ms corresponding to the drop in impact force. The impact force oscillated for approximately .6 ms due to failure propagating

along the specimen interface with the contact surface. This propagation can be seen in the plot of kevlar/epoxy lamina shear stress distribution at 3 ms shown in figure B-5.20. The sharp drop in impact force after 3 ms was due to buckling occurring (crush initiation) in the remaining elements. This buckling can be seen in the 3.5 ms stress-deformation plot shown in figure B-5.21. After the significant drop due to buckling the impact force recovers somewhat and begins to oscillate. This was a result of underlying regions of elements reloading and buckling. Figure B-5.22 shows the stress history for an element in the mid-section of the specimen. The loading/unloading sequence due to buckling of subsequent regions can be seen in its stress response. The element stress built as elements above it loaded to the point of buckling and dropped after buckling occurred. The element went into a tensile stress state due to energy stored during compression being released when the elements above buckled. At 8 ms the impact force spiked to values in excess of 15 kN. The spike was a result of a data file read error arising from an improperly closed file. The file was not properly closed due to the solution being terminated prematurely. Once the lamina failed, the foam containment was lost and it was extruded outward producing element distortions beyond allowable limits and termination of the solution.

Based on the impact force time history, the specimen CIL was 2.8 kLb (12.5 kN) and its SCL was .25 kLb (1.1 kN). These values are 63.7 % and 91.9 % below the reported test values of 7.13 kLb (31.7 kN) and 3.03 kLb (13.5 kN) respectively. The large differences in the CIL and SCL values is attributed to the Tsai-Wu orthotropic failure criteria. When

the combined stresses satisfied the failure criteria brittle failure occurred. For longitudinal and transverse loading the glass/epoxy and kevlar/epoxy materials do fail in a brittle as seen in the coupon tests. However in shear they do not fail in a brittle manner. As was seen in the coupon tests both the glass/epoxy and kevlar/epoxy materials can withstand plastic strain values in excess of 7%. The combination of the kevlar/epoxy lamina being loaded in shear and its low shear strength led to the failure criteria being met at low loads. Energy absorption in the plastic strain range was lost due to these premature failures. In addition, these premature failures led to energy absorption being lost due to containment of the foam being lost allowing it to free flow and fail prematurely.

A constitutive relationship and failure model that better represents the laminate behavior during crushing should be developed to improve the model predictions since Dytran does not currently offer a constitutive relationship with plasticity or a failure criteria based on plastic strain for orthotropic materials. Dytran does however offer the capability to incorporate user defined constitutive relationships and failure criteria. Thus developed constitutive relationships and failure models could be incorporated and used to represent the orthotropic lamina.

Despite the differences in EA parameter magnitudes the crushing behavior of the model was similar to that of test specimen up to 8 ms. Lamina failure occurred along at the impact mass interface and initiated buckling. Once buckled, the material began to crush progressively. This type behavior was seen in the test specimen as shown in figure

B-5.26. Figure B-5.23 shows a plot of the displacement of the support platen and impact mass over time. The difference between their displacement is a measure of crushing that occurred. Crushing occurred uniformly in that it did not oscillate. The crush rate increased over time reaching a maximum rate of 5.2 $^{in}/_{s}$ (133 $^{mm}/_{s}$) at 6 ms after which it remained relatively constant until 8 ms. The increased rate was due to the applied acceleration pulse increasing up to 6 ms. The increasing rate indicated that the model responded to the input properly. The impact mass acceleration also indicated that the model crush behavior was similar to test. The impact mass acceleration time history is shown in figure B-5.27 . Its peak acceleration was approximately 60 g's which is similar to a test impact mass acceleration of approximately 85 g's shown in figure B-5.15 . Note that the test impact mass acceleration shown in figure 5.15 is not for the modeled B1.4 specimen but instead is a representative curve. Thus, the values should not match exactly.

The support platen acceleration and velocity time histories were plotted to verify the model inputs. Their time histories are shown in figures B-5.24 and B-5.25 respectively. The acceleration profile matched the input profile with the exception that it was stepped rather than being a smooth ramp. The velocity profile matched that input profile with no exceptions.

5.4.3 Lamina Constitutive Relation Modified to Elastic Plastic

The constitutive relation of the lamina was changed to an elastic-plastic representation to approximate the effects of a constitutive relation that accounted for plasticity. The

average properties of the fabric lamina given in tables A-4.25 through A-4.28 were used. Dytran only allows for an isotropic relation between elastic modulus and shear modulus thus both could not be specified from the table. Since the loading and failure in the kevlar lamina was shear its shear modulus was entered. The shear modulus was given an elastic-plastic behavior by specifying a plastic shear modulus of half its linear value. The glass lamina was loaded along its fiber direction thus its elastic modulus was used. Its elastic-plastic behavior was approximated by specifying the plastic modulus to be that of the glass segment B modulus. A value of .45 was entered for the kevlar and glass lamina Poisson's ratio to give as near a correct value for E and G as possible, .5 being the limit due to a singularity in the stress relationship. Failure was defined by plastic strain. When the lamina strain reached the specified maximum allowable strain failure occurred. The kevlar ultimate shear strain and glass ultimate normal strain determined from the tests were used to define failure.

Figure B-5.28 shows the impact force time history. From the graph the specimen had a CIL of 6.7 kLb (30.0 kN) and a SCL of 3.1 kLb (13.8 kN). These values differed from test values by 5.0 % and 1.5 % respectively. Thus incorporating plasticity into the constitutive relation and defining failure to occur at the fabric's ultimate strain greatly improves the model accuracy in predicting energy absorption.

Chapter 6

Conclusions

1. The Belytschko-Tsay element formulation is limited in that its rotation is based on in-plane rotations only.
2. Care must be taken in creating the model mesh due to the elements Lagrangian displacement representation that limits their amount of distortion.
3. Care must be taken in defining contact surfaces. Narrow contact surfaces allow penetration whereas large contact surfaces produce unrealistically large initial contact forces when contact is made parallel to large flat sections of slave nodes.
4. Defining the impact according to the actual test acceleration pulse produces much better model behavior than representing the impact as a free fall into a rigidly supported impact.
5. The model's crushing behavior was similar to that of test specimen when the contact surfaces are properly defined and the impact acceleration is defined. However its predicted EA values are extremely low.
6. The orthotropic constitutive relation in Dytran is not an adequate representation of the glass/epoxy or kevlar/epoxy lamina. A representation of the nonlinear shear stress-shear strain plastic region is needed.
7. A more complete constitutive relation that accurately represents shear behavior should be developed for the fiber reinforced lamina and incorporated into the

model through Dytran's user defined constitutive relation option.

8. The available orthotropic material failure criteria do not adequately represent the failure mode of the fiber reinforced material. The criteria result in brittle failure with no plasticity effects. This is not representative of the shear failure mode. In addition, the element is taken out of the calculation after failure occurs and essentially no longer exists after failure. Load transmission through the othotropic material into the impact mass is lost until contact is made with underlying unfailed elements. The foam material is also free to flow once surrounding lamina elements fail. In reality, failed elements do provide load transmission normal to their surface and do provide some restraint to the foam.

9. The model's predicted CIL and SCL are low as a result of the orthotropic constitutive relation and its brittle failure mode. Premature failure occurs in the orthotropic material and the strain energy due to plastic deformation of the material is lost. Premature failure also leads to the containment of the foam being lost allowing it to flow. Energy of compressing the foam against the containing lamina is lost.

10. An orthotropic failure criteria should be developed that better represents the failure mode and incorporated into the model through Dytran's user defined failure criteria option.

11. An elastic-plastic representation of the orthotropic lamina material provides a close approximation of the EA parameters. However this technique is limited for

general modeling since the dominate loading and failure mode must be known so that the corresponding isotropic elastic constant can be used to define the material, i.e. shear modulus for shear load/failure or elastic modulus for in-plane load/failure.

References

References

1. Belytschko, T. B., and C. S. Tsay. "Explicit Algorithms for Nonlinear Dynamics of Shells", The American Society of Mechanical Engineers, 1981.

2. Carden, H. D., and S. Kellas. "Energy Absorbing-Beam Design for Composite Aircraft Subfloors", proceedings of AIAA/ASME/ASCE/ASC 34th Structures, Structural Dynamics Conference, LaJolla, Ca., April 19-21, 1993.

3. Cronhkite, J. D., Y. T. Chung, and L. W. Bark. "Crashworthy Composite Structures", USAAVSCOM TR-87-D-10, DOT/FAA/AC-87-35, December, 1987.

4. Daniel, Isaac M., and Ishai, Ori. Engineering Mechanics of Composite Materials . New York: Oxford UP, 1994.

5. Farley, Gary L. "The Effects of Crushing Speed on the Energy-Absorption Capability of Composite Material", NASA-Langley, 1987.

6. Hallquist, John O., comp. LS-DYNA Theoretical Manual. Livermore, CA: Livermore Software Technology Corporation, 1998.

7. Jones, Lisa E., and Huey D. Carden. "Overview of Structural Behavior and Occupant Responses from a Crash Test of a Composite Airplane", SAE General, Corporate and Regional Aviation Meeting and Exposition, Wichita, Kansas, May 3-5, 1995.

8. Kellas, Sotiris. "An Experimental Investigation into the Energy Absorption Performance of Composite Beam Webs for Aircraft Subfloor Applications", American Helicopter Society National Technical Specialist's Meeting on Rotorcraft Structures, Williamsburg, Va. 1995.

9. MacNeal-Schwendler Corporation. MSC/DYTRAN Version 4.0 Users Manual. Los Angeles: MacNeal-Schwendler, 1997.

10. Malvern, Lawrence E. Introduction to the Mechanics of a Continuous Medium. Prentice-Hall, New Jersey, 1969.

11. Stasa, Frank L. Applied Finite Element Analysis for Engineers. Holt, Rinehart and Winston, New York, 1985.

12. Vaughan, Victor L. Jr., and Emilio Alfaro-Bou. "Impact Dynamics Research Facility for Full-Scale Aircraft Crash Testing", NASA-Langley, 1976.

Appendices

Appendix A

Tables

Table 3.1 Box core specimen EA parameters.
Source: Kellas, Sotiris. "An Experimental Investigation into the Energy Absorption Performance of Composite Beam Webs for Aircraft Subfloor Applications" American Helicopter Society National Technical Specialist's Meeting on Rotorcraft Structures, Williamsburg, Va. 1995.

Spec.I.D.* [cell size] (cell)/(skin) Lay-up	Impact Vel. ft/s	CIL Length lb/in	SCL Length lb/in	SCL/CIL %	Crush Stroke %	Energy Absorbed ft-lb	Normaliz. Sp.Energ. ft-lb/lb
Bx.1 4[3.0x2.0] (±45)/(±45)	28.2	251.1	135.9	54.1	73.0	790	2340
Bx.2 4[3.0x2.0] (0/90)/(±45)	22.7	548.5	143.8	26.2	58.6	621	1784
Bx.3 5[2.4x1.0] (±45)/(±45)	25.6	385.7	155.5	40.3	79.4	1034	3256
Bx.4 5[2.4x1.0] (0/90)/(±45)	25.7	301.5	150.5	49.9	83.3	1085	3361
Bx.5 5[2.4x1.0] $(\pm 45)/(\pm 45)_2$	26.8	627.5	199.1	31.7	59.5	1008	3388
Bx.6 5[2.4x1.0] $(0/90)/(\pm 45)_2$	27.4	952.3	286.5	30.1	30.4	711	3465
Bx.7 5[2.4x1.5] (±45)/(±45)	26.3	519.9	232.5	44.7	53.2	1011	3801
Bx.8 5[2.4x1.5] (0/90)/(±45)	27.5	718.3	188.9	26.3	68.1	942	2305
Bx.9 8[1.5x1.0] (±45)/(±45)	29.8	538.4	201.2	37.4	81.8	1346	3657
Bx.10 8[1.5x1.0] (0/90)/(±45)	29.7	837.4	375.0	44.8	34.8	1050	5136

* Bx. stands for box-core. The digit in front of the square brackets represents the number of cells in the specimen's core.

Table 3.2 Block core specimen EA parameters.
Source: Kellas, Sotiris. "An Experimental Investigation into the Energy Absorption Performance of Composite Beam Webs for Aircraft Subfloor Applications" American Helicopter Society National Technical Specialist's Meeting on Rotorcraft Structures, Williamsburg, Va. 1995.

Spec.I.D.* [cell size] (cell)/(skin) Lay-up	Impact Vel. ft/s	CIL Length lb/in	SCL Length lb/in	SCL / CIL %	Crush Stroke %	Energy Absorbed ft-lb	Normaliz. Sp.Energ. ft-lb/lb
Bl.1 4[3.0x2.0] (±45)/(±45)	28.1	605.1	299.7	49.5	54.4	1333	2817
Bl.2 4[3.0x2.0] (0/90)/(±45)	28.2	606.2	230.6	38.0	71.4	1401	2255
Bl.3 5[2.4x1.0] (±45)/(±45)	29.9	518.6	245.3	47.3	63.5	1336	3435
Bl.4 5[2.4x1.0] (0/90)/(±45)	28.3	593.1	252.4	42.6	51.0	1098	4005
Bl.5 5[2.4x1.0] $(\pm45)/(\pm45)_2$	32.1	690.3	398.0	57.7	62.1	1936	4796
Bl.6 5[2.4x1.0] $(0/90)/(\pm45)_2$	32.4	939.2	310.6	33.1	52.0	1342	3823
Bl.7 5[2.4x1.5] (±45)/(±45)	29.0	806.2	345.3	42.8	35.1	1010	3591
Bl.8 5[2.4x1.5] (0/90)/(±45)	30.3	756.0	246.5	32.6	57.9	1166	2479
Bl.9 8[1.5x1.0] (±45)/(±45)	29.0	666.1	322.6	48.4	55.5	1429	4392
Bl.10 8[1.5x1.0] (0/90)/(±45)	28.3	781.0	260.9	33.4	55.5	1236	3617

* Bl. stands for block-core. The digit in front of the square brackets represents the number of cells in the specimen's core.

Table 4.1 Isotropic Material Elastic Properties, Imperial

Material Type	E psi (10^6)	E_H psi (10^6)	ν	G psi (10^6)	ρ $^{slug}/_{in^3}$ (10^{-3})
Steel	30.0	3.0	.29	11.6	.735

Table 4.2 Orthotropic Material Elastic Properties, Imperial

Material Type	E_1 psi (10^6)	E_2 psi (10^6)	ν_{12}	ν_{21}	G_{12} psi (10^6)	ρ $^{slug}/_{in^3}$ (10^{-3})
glass/epoxy	5.7	1.24	.28	.06	0.54	.197
kevlar/epoxy	12.6	0.80	.34	.02	0.31	.148

Table 4.3 Isotropic Strength Properties, Imperial

Material Type	S_y psi (10^3)	Elongation %
Steel	65.0	20.0

Table 4.4 Orthotropic Strength Properties, Imperial

Material Type	S_{1T} psi (10^3)	S_{1C} psi (10^3)	S_{2T} psi (10^3)	S_{2C} psi (10^3)	S_S psi (10^3)
glass/epoxy	157.0	90.0	5.7	18.6	12.9
kevlar/epoxy	185.0	49.0	4.2	22.9	7.1

Table 4.5 Isotropic Material Elastic Properties, mm/tonne/sec

Material Type	E $^{N}/_{mm^3}$ (10^3)	E_H $^{N}/_{mm^3}$ (10^3)	ν	G $^{N}/_{mm^3}$ (10^3)	ρ $^{kg}/_{mm^3}(10^{-9})$
Steel	206.8	20.7	.29	79.5	7.8

Table 4.6 Orthotropic Material Elastic Properties, mm/tonne/sec

Material Type	E_1 $^{N}/_{mm^3}$ (10^3)	E_2 $^{N}/_{mm^3}$ (10^3)	ν_{12}	ν_{21}	G_{12} $^{N}/_{mm^3}$ (10^3)	ρ $^{kg}/_{mm^3}(10^{-9})$
glass/epoxy	39.0	8.6	.28	.06	3.9	2.10
kevlar/epoxy	87.0	5.5	.34	.02	2.2	1.38

Table 4.7 Isotropic Strength Properties, mm/tonne/sec

Material Type	S_y $^{N}/_{mm^3}$	Elongation %
Steel	450.0	20.0

Table 4.8 Orthotropic Strength Properties, mm/tonne/sec

Material Type	S_{1T} $^{N}/_{mm^3}$	S_{1C} $^{N}/_{mm^3}$	S_{2T} $^{N}/_{mm^3}$	S_{2C} $^{N}/_{mm^3}$	S_S $^{N}/_{mm^3}$
glass/epoxy	1080.0	620.0	39.0	128.0	89.0
kevlar/epoxy	1280.0	335.0	30.0	158.0	49.0

Table 4.9 Glass/Epoxy Sheet 1 Coupon Measurements

dir/#	t_a	w_a	A_a	t_b	W_b	A_b	t_c	W_c	A_c	A_{avg}	A_{min}
L_1	0.050	0.993	0.04965	0.048	0.991	0.04757	0.048	0.990	0.04752	0.04825	0.04752
L_2	0.049	0.993	0.04866	0.048	0.991	0.04757	0.047	0.989	0.04648	0.04757	0.04648
L_3	0.048	0.997	0.04786	0.047	0.998	0.04691	0.047	0.998	0.04691	0.04722	0.04691
L_4	0.047	0.997	0.04686	0.047	0.997	0.04686	0.047	0.997	0.04686	0.04686	0.04686
L_5	0.046	0.997	0.04586	0.046	0.998	0.04591	0.047	0.997	0.04686	0.04621	0.04586
T_1	0.046	0.997	0.04586	0.046	0.996	0.04582	0.045	0.997	0.04486	0.04551	0.04486
T_2	0.046	0.997	0.04586	0.046	0.997	0.04586	0.046	0.997	0.04586	0.04586	0.04586
T_3	0.045	0.997	0.04487	0.046	0.997	0.04586	0.047	0.997	0.04686	0.04586	0.04487
T_4	0.046	0.998	0.04591	0.046	0.998	0.04591	0.046	0.997	0.04586	0.04589	0.04586
T_5	0.047	0.999	0.04595	0.047	0.998	0.04691	0.047	0.998	0.04691	0.04659	0.04595
T_6	0.047	0.998	0.04691	0.047	0.998	0.04691	0.045	0.996	0.04482	0.04621	0.04482
G_1	0.042	0.998	0.04192	0.045	0.998	0.04491	0.045	0.998	0.04491	0.04391	0.04192
G_2	0.043	0.983	0.04227	0.044	0.988	0.04347	0.045	0.993	0.04468	0.04348	0.04227
G_3	0.043	0.998	0.04291	0.044	0.998	0.04391	0.046	0.999	0.04595	0.04426	0.04291
G_4	0.044	0.998	0.04391	0.044	0.999	0.04396	0.046	0.999	0.04595	0.04461	0.04391
G_5	0.044	0.998	0.04391	0.045	0.998	0.04491	0.046	0.999	0.04595	0.04492	0.04391
G_6	0.044	0.975	0.04290	0.046	0.976	0.04490	0.046	0.978	0.04499	0.04426	0.04290
G_7	0.047	0.997	0.04686	0.047	0.997	0.04686	0.047	0.997	0.04686	0.04686	0.04686
G_8	0.048	0.997	0.04786	0.047	0.998	0.04691	0.046	0.998	0.04591	0.04689	0.04591
G_9	0.048	1.000	0.04800	0.047	0.998	0.04691	0.046	0.998	0.04591	0.04694	0.04591

Table 4.10 Glass/Epoxy Sheet 2 Coupon Measurements

dir/#	t_a	w_a	A_a	t_b	W_b	A_b	t_c	W_c	A_c	A_{avg}	A_{min}
L_1	0.042	0.997	0.04187	0.042	0.997	0.04187	0.043	0.999	0.04296	0.04223	0.04187
L_2	0.041	0.997	0.04088	0.042	0.997	0.04187	0.042	0.998	0.04192	0.04156	0.04088
L_3	0.042	0.997	0.04187	0.041	0.997	0.04088	0.041	0.997	0.04088	0.04121	0.04088
L_4	0.042	0.996	0.04183	0.041	0.996	0.04084	0.041	0.997	0.04088	0.04118	0.04084
L_5	0.042	0.996	0.04183	0.042	0.996	0.04183	0.041	0.996	0.04084	0.04150	0.04084
T_1	0.043	0.999	0.04296	0.042	0.999	0.04196	0.041	0.998	0.04092	0.04195	0.04092
T_2	0.041	0.999	0.04096	0.042	0.999	0.04196	0.042	0.998	0.04192	0.04161	0.04096
T_3	0.042	0.997	0.04187	0.042	0.996	0.04183	0.042	0.995	0.04179	0.04183	0.04179
T_4	0.041	0.998	0.04092	0.043	0.998	0.04291	0.041	0.998	0.04092	0.04158	0.04092
T_5	0.041	0.998	0.04092	0.042	0.998	0.04192	0.042	0.998	0.04192	0.04159	0.04092
T_6	0.042	0.998	0.04192	0.042	0.998	0.04192	0.042	0.998	0.04192	0.04192	0.04192
G_1	0.040	0.986	0.03944	0.040	0.990	0.03960	0.040	0.992	0.03968	0.03957	0.03944
G_2	0.041	0.998	0.04092	0.040	0.997	0.03988	0.040	0.997	0.03988	0.04023	0.03988
G_3	0.041	0.994	0.04075	0.040	0.994	0.03976	0.040	0.995	0.03980	0.04010	0.03976
G_4	0.041	0.997	0.04088	0.041	0.997	0.04088	0.041	0.997	0.04088	0.04088	0.04088
G_5	0.041	0.998	0.04092	0.041	0.997	0.04088	0.041	0.997	0.04088	0.04089	0.04088
G_6	0.040	0.997	0.03988	0.040	0.998	0.03992	0.041	0.998	0.04092	0.04024	0.03988
G_7	0.040	0.997	0.03988	0.040	0.997	0.03988	0.041	0.997	0.04088	0.04021	0.03988
G_8	0.040	0.996	0.03988	0.040	0.997	0.03988	0.041	0.998	0.04092	0.04023	0.03988

Table 4.11 Kevlar/Epoxy Sheet 1 Coupon Measurements

dir/#	t_a	w_a	A_a	t_b	W_b	A_b	t_c	W_c	A_c	A_{avg}	A_{min}
L_1	0.046	0.994	0.04572	0.047	0.993	0.04667	0.047	0.994	0.04672	0.04637	0.04572
L_2	0.049	0.994	0.04871	0.050	0.992	0.04960	0.048	0.994	0.04771	0.04867	0.04771
L_3	0.047	0.995	0.04676	0.049	0.997	0.04885	0.049	0.995	0.04876	0.04812	0.04676
L_4	0.048	0.99	0.04752	0.047	0.990	0.04653	0.047	0.991	0.04658	0.04688	0.04653
L_5	0.048	0.993	0.04766	0.054	0.993	0.05362	0.052	0.992	0.05158	0.05096	0.04766
T_1	0.047	0.996	0.04681	0.042	0.996	0.04183	0.045	0.996	0.04482	0.04449	0.04183
T_2	0.047	1.000	0.04700	0.046	1.000	0.04600	0.048	1.000	0.04800	0.04700	0.04600
T_3	0.050	0.995	0.04975	0.048	0.995	0.04776	0.046	0.995	0.04577	0.04776	0.04577
T_4	0.044	0.996	0.04382	0.044	0.996	0.04382	0.045	0.995	0.04477	0.04414	0.04382
G_1	0.045	0.988	0.04446	0.043	0.992	0.04266	0.043	0.989	0.04253	0.04321	0.04253
G_2	0.043	0.987	0.04244	0.043	0.988	0.04248	0.044	0.989	0.04352	0.04281	0.04244
G_3	0.041	0.987	0.04047	0.043	0.988	0.04248	0.043	0.987	0.04244	0.04180	0.04047
G_4	0.042	0.988	0.04150	0.043	0.988	0.04248	0.045	0.988	0.04446	0.04281	0.04150
G_5	0.042	0.988	0.04150	0.045	0.987	0.04442	0.045	0.988	0.04446	0.04346	0.04150
G_6	0.044	0.989	0.04352	0.044	0.987	0.04343	0.044	0.988	0.04347	0.04347	0.04343

Table 4.12 Kevlar/Epoxy Sheet 2 Coupon Measurements

dir/#	t_a	w_a	A_a	t_b	W_b	A_b	t_c	W_c	A_c	A_{avg}	A_{min}
L_1	0.045	0.973	0.04378	0.044	0.972	0.04277	0.045	0.972	0.04374	0.04343	0.04277
L_2	0.045	0.972	0.04374	0.043	0.973	0.04184	0.045	0.975	0.04388	0.04315	0.04184
L_3	0.045	0.971	0.04370	0.045	0.971	0.04370	0.045	0.971	0.04370	0.04370	0.04370
L_4	0.045	0.971	0.04370	0.045	0.970	0.04365	0.046	0.970	0.04462	0.04399	0.04365
L_5	0.046	0.911	0.04191	0.044	0.910	0.04004	0.043	0.907	0.03900	0.04032	0.03900
T_1	0.045	0.977	0.04396	0.044	0.976	0.04294	0.043	0.976	0.04197	0.04296	0.04197
T_2	0.043	0.995	0.04278	0.043	0.996	0.04283	0.043	0.996	0.04283	0.04281	0.04278
T_3	0.046	0.995	0.04577	0.045	0.995	0.04477	0.044	0.996	0.04382	0.04479	0.04382
T_4	0.045	0.834	0.03753	0.045	0.833	0.03748	0.045	0.834	0.03753	0.03752	0.03748
G_1	0.045	0.995	0.04477	0.044	0.995	0.04378	0.045	0.994	0.04473	0.04443	0.04378
G_2	0.046	0.994	0.04572	0.045	0.995	0.04477	0.046	0.997	0.04586	0.04545	0.04477
G_3	0.044	0.992	0.04365	0.045	0.992	0.04464	0.045	0.994	0.04473	0.04434	0.04365
G_4	0.044	0.888	0.03907	0.046	0.889	0.04089	0.046	0.888	0.04085	0.04027	0.03907
G_5	0.044	0.995	0.04378	0.046	0.995	0.04577	0.045	0.994	0.04473	0.04476	0.04378
G_6	0.046	0.997	0.04586	0.045	0.995	0.04477	0.044	0.995	0.04378	0.04481	0.04378
G_7	0.045	0.998	0.04491	0.043	0.996	0.04283	0.044	0.997	0.04387	0.04387	0.04283
G_8	0.044	0.997	0.04387	0.045	0.999	0.04495	0.043	0.996	0.04283	0.04388	0.04283

Table 4.13 Glass/Epoxy Sheet 1 Longitudinal Properties

Sample number	E_{1A} kpsi	E_{1B} kpsi	υ_{12}	S_{1y} kpsi	S_{1u} kpsi	ε_{1u} %
1	2725.6	1922.1	0.154	11.858	37.928	1.836
2	2683.1	1853.0	0.125	12.005	37.377	1.861
3	2756.4	1958.4	0.113	10.693	34.585	1.658
4	2718.4	1860.8	0.120	12.905	39.219	1.923
5	2703.8	1833.3	0.139	10.926	39.990	2.042
AVG.	2717.5	1885.5	0.130	11.677	37.820	1.864
Std. Dev.	24.3	47.0	0.030	0.798	1.862	0.125

Table 4.14 Glass/Epoxy Sheet1 Transverse Properties

Sample Number	E_{2A} kpsi	E_{2B} kpsi	υ_{21}	S_{2y} kpsi	S_{2u} kpsi	ε_{2u} %
1	2893.0	2135.1	0.098	13.231	50.373	2.269
2	2778.9	2085.0	0.115	12.518	50.078	2.309
3	2919.3	2117.9	0.093	13.430	50.051	2.253
4	2818.2	2136.8	0.096	13.466	47.633	2.123
5	2821.1	2084.8	0.063	13.643	49.064	2.238
6	2912.2	2115.6	0.079	13.511	47.679	2.132
AVG.	2857.1	2112.5	0.091	13.300	49.146	2.221
Std. Dev.	53.4	21.1	0.015	0.370	1.129	0.069

Table 4.15 Glass/Epoxy Sheet 1 Shear Propreties

Sample Number	G_{12} kpsi	S_{12y} kpsi	S_{12u} kpsi	γ_{12u} %
1	459.5	1.6	7.674	7.309
2	447.8	1.5	7.841	7.291
3	474.9	1.5	7.985	7.312
4	473.8	1.8	8.098	7.294
5	463.8	1.7	7.964	7.313
6	478.0	1.7	8.220	7.308
7	472.9	1.7	7.778	5.329
8	461.9	1.8	7.524	7.294
9	474.4	1.6	7.101	7.315
AVG.	467.4	1.7	7.798	7.085
Std. Dev.	9.3	0.1	0.318	0.621

Table 4.16 Glass/Epoxy Sheet 2 Longitudinal Properties

Sample Number	E_{1A} kpsi	E_{1B} kpsi	υ_{12}	S_{1y} kpsi	S_{1u} kpsi	ε_{1u} %
1	3072.0	2395.4	0.101	15.298	46.485	1.862
2	3298.7	2426.0	0.116	12.962	45.747	1.740
3	3286.9	2299.1	0.109	13.423	48.976	2.020
4	3236.4	2373.9	0.096	12.952	46.081	1.804
5	3140.1	2281.2	0.095	11.365	48.364	2.060
AVG.	3206.8	2373.5	0.103	13.200	47.131	1.897
Std. Dev.	87.6	55.9	0.010	1.260	1.293	0.123

Table 4.17 Glass/Epoxy Sheet2 Transverse Properties

Sample Number	E_{2A} kpsi	E_{2B} kpsi	υ_{21}	S_{2y} kpsi	S_{2u} kpsi	ε_{2u} %
1	3078.6	2185.4	0.106	13.252	50.799	2.211
2	-	-	-	-	-	-
3	3129.4	2186.7	0.112	12.549	48.834	2.115
4	3037.8	2179.1	0.094	12.865	46.767	2.024
5	3191.4	2210.8	0.092	12.580	48.971	2.092
6	2853.8	2266.5	0.102	16.270	48.688	2.075
AVG.	3058.2	2205.7	0.101	13.503	48.812	2.103
Std. Dev.	114.4	32.3	0.009	1.406	1.278	0.062

Table 4.18 Glass/Epoxy Sheet 2 Shear Properties

Sample Number	G_{12} kpsi	S_{y12} kpsi	S_{u12} kpsi	γ_{u12} %
1	516.9	1.8	9.013	7.298
2	532.7	1.9	8.937	7.298
3	548.5	2.0	8.623	7.310
4	526.6	1.8	8.014	7.309
5	541.9	1.6	7.911	7.305
6	544.7	2.0	7.823	7.290
7	538.7	1.9	8.025	7.298
8	535.4	1.9	8.285	7.287
AVG.	535.7	1.9	8.329	7.299
Std. Dev.	9.6	0.1	0.440	0.008

Table 4.19 Kevlar/Epoxy Sheet 1 Longitudinal Properties

Sample Number	E_1 kpsi	υ_{12}	S_{1u} kpsi	ε_{1u} %
1	3461.4	0.048	57.071	1.637
2	3271.4	-0.020	55.952	1.696
3	3467.1	0.032	58.625	1.683
4	3470.1	0.003	61.094	1.753
5	3000.6	0.049	47.999	1.579
AVG.	3334.1	0.043	56.148	1.670
Std. Dev.	183.1	0.006	4.425	0.058

Table 4.20 Kevlar/Epoxy Sheet 1 Transverse Properties

Sample Number	E_2 kpsi	υ_{12}	S_{2u} kpsi	ε_{2u} %
1	3487.4	0.067	66	1.866
2	3119.1	0.083	56.364	1.798
3	3128.8	0.068	54.311	1.728
4	3290.7	0.103	64.229	1.945
AVG.	3256.5	0.080	60.226	1.834
Std. Dev.	149.7	0.018	4.982	0.080

Table 4.21 Kevlar/Epoxy Sheet 1 Shear Properties

Sample Number	G_{12} kpsi	S_{y12} kpsi	S_{u12} kpsi	γ_{u12} %
1	196.3	1.5	6.101	7.318
2	185.7	1.4	7.386	7.330
3	186.8	1.3	6.522	7.331
4	194.4	1.6	5.306	7.320
5	182.7	1.7	4.641	7.308
AVG.	189.2	1.5	5.991	7.321
Std. Dev.	5.2	0.1	0.952	0.008

Table 4.22 Kevlar/Epoxy Sheet 2 Longitudinal Properties

Sample Number	E_1 kpsi	υ_{12}	S_{1u} kpsi	ε_{1u} %
1	3590.0	0.074	66.041	1.839
2	3731.0	0.053	68.436	1.820
3	3676.8	0.075	61.186	1.656
4	3619.5	0.089	65.036	1.807
5	3278.3	0.082	63.345	1.913
AVG.	3579.1	0.075	64.809	1.807
Std. Dev.	158.0	0.016	2.449	0.084

Table 4.23 Kevlar/Epoxy Sheet 2 Transverse Properties

Sample Number	E_2 kpsi	υ_{12}	S_{2u} kpsi	ε_{2u} %
1	3396.7	0.059	62.117	1.854
2	3385.1	0.053	62.897	1.857
3	3324.6	0.091	59.167	1.78
AVG.	3368.8	0.068	61.394	1.830
Std. Dev.	31.6	0.016	1.606	0.036

Table 4.24 Kevlar/Epoxy Sheet 2 Shear Properties

Sample Number	G_{12} kpsi	S_{12y} kpsi	S_{12u} kpsi	γ_{12u} %
1	-	-	-	-
2	191.6	1.6	7.741	7.218
3	188.0	1.6	6.706	7.201
4	174.5	1.6	6.685	7.243
5	187.1	1.8	8.115	4.011
6	169.0	1.6	5.980	7.222
7	167.6	1.6	6.411	7.207
8	173.4	1.6	6.440	7.231
AVG.	178.7	1.6	6.868	6.762
Std. Dev.	9.2	0.1	0.713	1.123

Table 4.25 Fabric Lamina Averaged Elastic Properties, Imperial

Material Type	E psi (10^6)	E_H psi (10^6)	ν	G psi (10^6)	ρ $^{slug}/_{in^3}$ (10^{-3})
glass/epoxy	2.96	2.14	.106	.47	.197
kevlar/epoxy	3.31	.33	.067	.184	.148

Table 4.26 Fabric Lamina Average Strength Properties, Imperial

Material Type	S_Y psi (10^3)	S_U psi (10^3)	S_S psi (10^3)	ϵ_U %	γ_U %
glass/epoxy	12.9	45.7	1.80	2.021	7.192
kevlar/epoxy	N/A	60.6	1.55	1.784	7.042

Table 4.27 Fabric Lamina Averaged Elastic Properties, mm/tonne/sec

Material Type	E $^{N}/_{mm^3}$ (10^9)	E_H $^{N}/_{mm^3}$ (10^9)	ν	G $^{N}/_{mm^3}$ (10^9)	ρ $^{kg}/_{mm^3}$ (10^{-9})
glass/epoxy	20.4	14.7	.106	3.2	.197
kevlar/epoxy	22.8	N/A	.067	1.3	.148

Table 4.28 Fabric Lamina Average Strength Properties, mm/tonne/sec

Material Type	S_Y $^{N}/_{mm^3}$ (10^3)	S_U $^{N}/_{mm^3}$ (10^3)	S_S $^{N}/_{mm^3}$ (10^3)	γ_u %	ϵ_U %
glass/epoxy	89.	315.	12.4	7.192	2.021
kevlar/epoxy	N/A	418.	10.7	7.042	1.784

Table 5.1 Time-Velocity Data Points Defining Support Platen Time History

Time (sec)	velocity (mm/sec)
0.0000	0.00
0.0005	61.31
0.0010	245.25
0.0015	551.81
0.0020	981.00
0.0025	1532.81
0.0030	2207.25
0.0035	3004.31
0.0040	3924.00
0.0045	4966.31
0.0050	6131.25
0.0055	7357.50
0.0060	8583.75
0.0065	9748.94
0.0070	10791.50
0.0075	11711.44
0.0080	12508.75
0.0085	13183.44
0.0090	13735.50
0.0095	14164.94
0.0100	14471.75
0.0105	14655.94
0.0110	14717.50

Appendix B

Figures

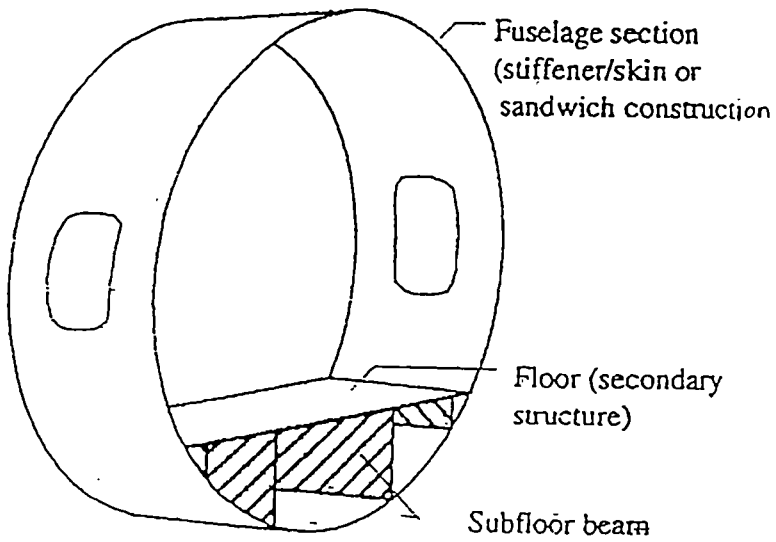


Figure 1.1 Subfloor attachment to fuselage.
Source: Kellas, Sotiris. "An Experimental Investigation into the Energy Absorption Performance of Composite Beam Webs for Aircraft Subfloor Applications" American Helicopter Society National Technical Specialist's Meeting on Rotorcraft Structures, Williamsburg, Va. 1995.

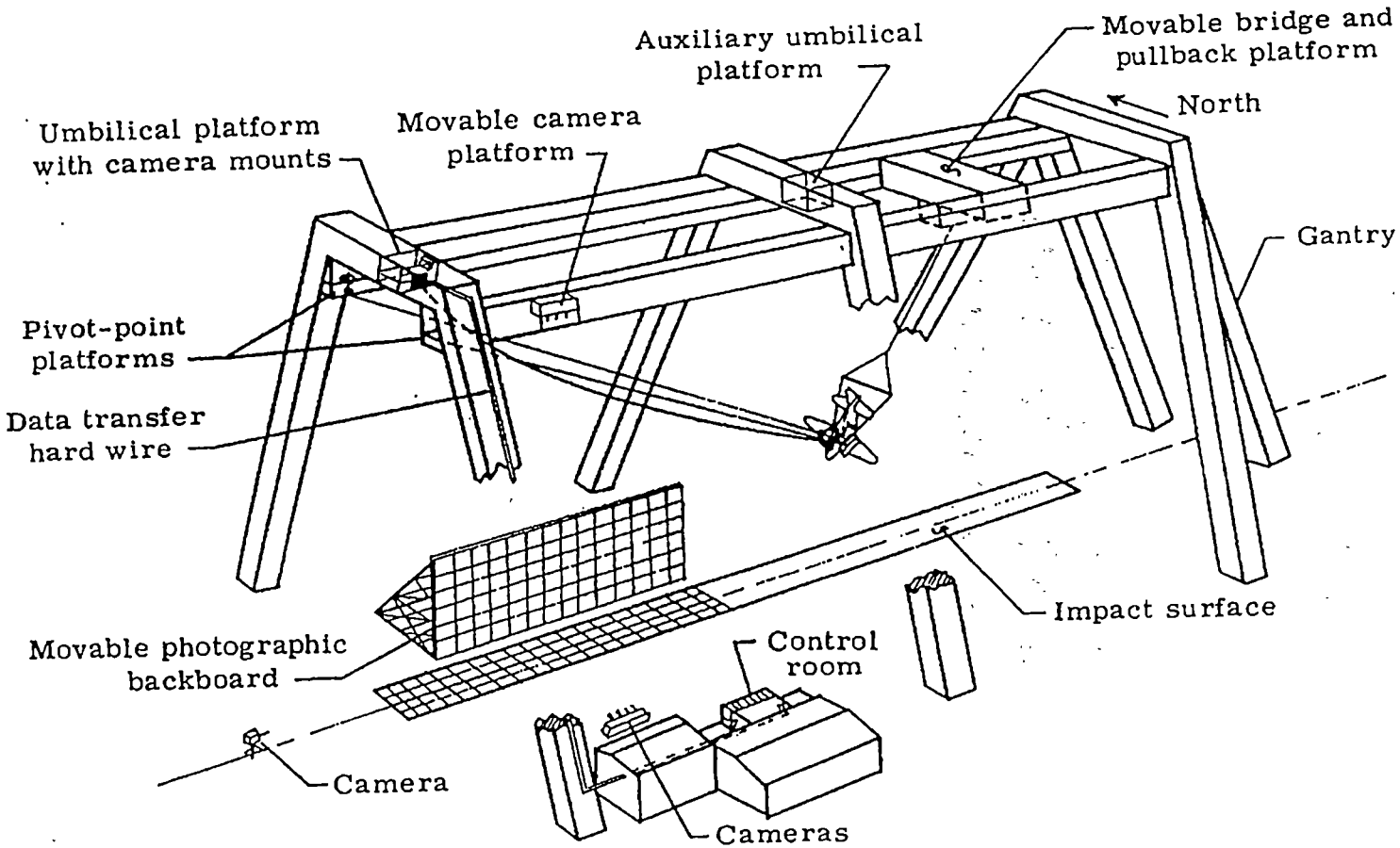


Figure 1.2 IDRF Full scale aircraft test fixture.
Source: Vaughan, Victor L. Jr., and Emilio Alfaro-Bou. "Impact Dynamics Research Facility for Full-Scale Aircraft Crash Testing", NASA-Langley, 1976.

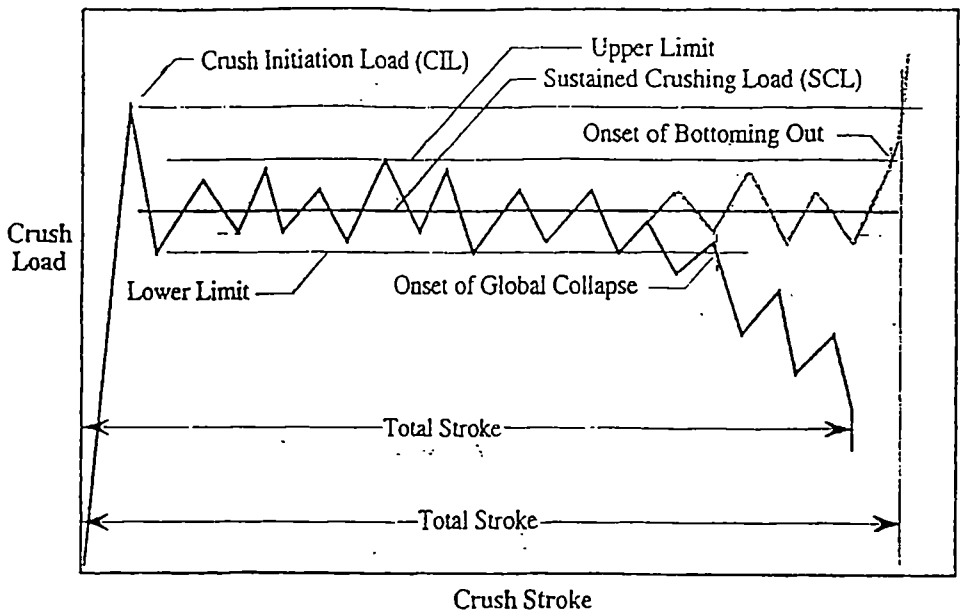


Figure 1.3 Graphical depiction of EA parameters.
Source: Kellas, Sotiris. "An Experimental Investigation into the Energy Absorption Performance of Composite Beam Webs for Aircraft Subfloor Applications" American Helicopter Society National Technical Specialist's Meeting on Rotorcraft Structures, Williamsburg, Va. 1995.

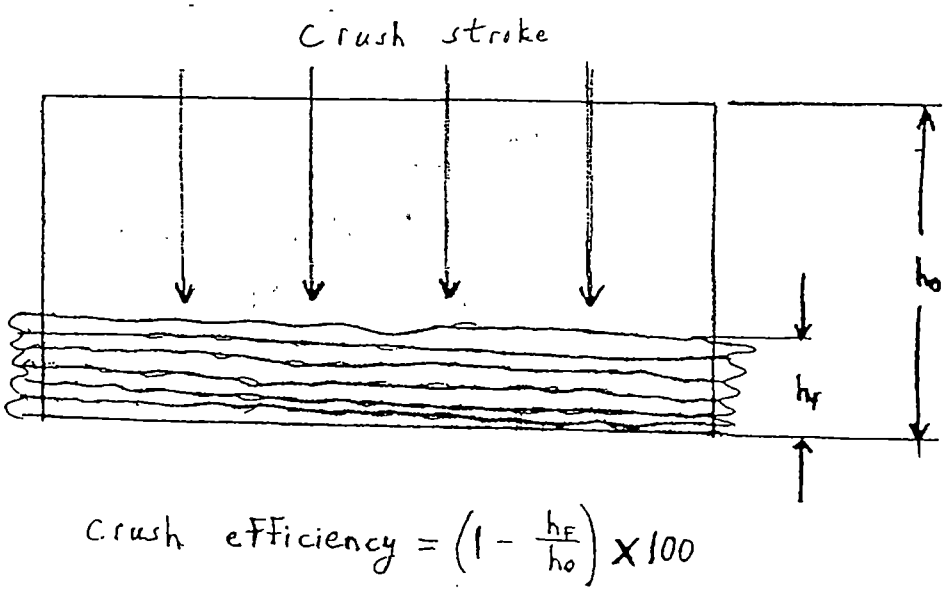


Figure 1.4 Graphical representation of crush efficiency.

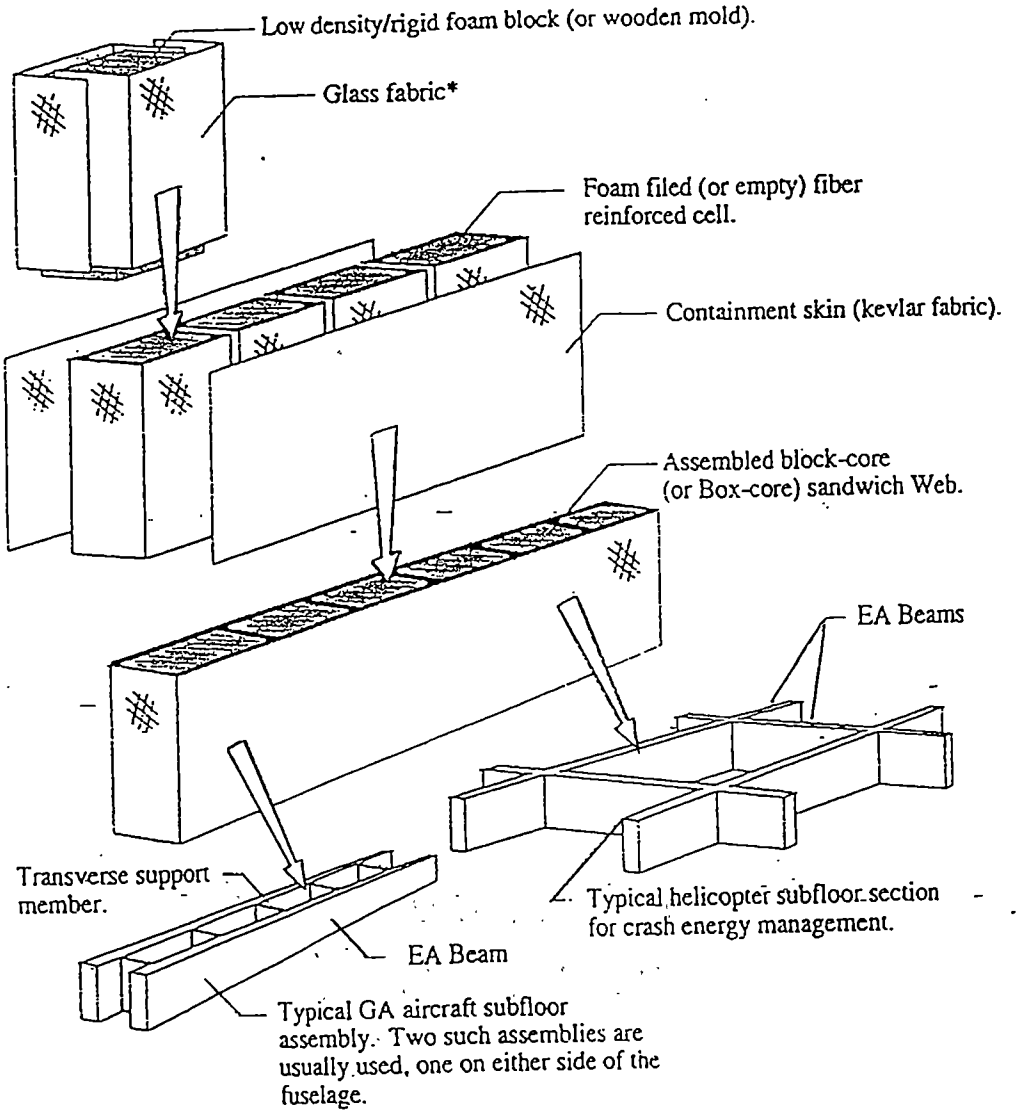
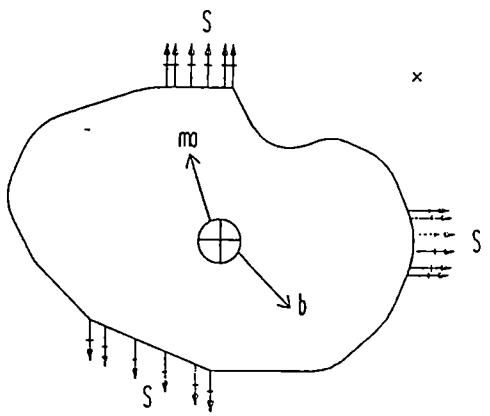
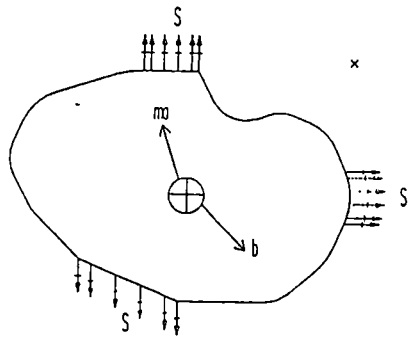


Figure 1.5 Rectangular composite beam construction.
Source: Kellas, Sotiris. "An Experimental Investigation into the Energy Absorption Performance of Composite Beam Webs for Aircraft Subfloor Applications" American Helicopter Society National Technical Specialist's Meeting on Rotorcraft Structures, Williamsburg, Va. 1995.

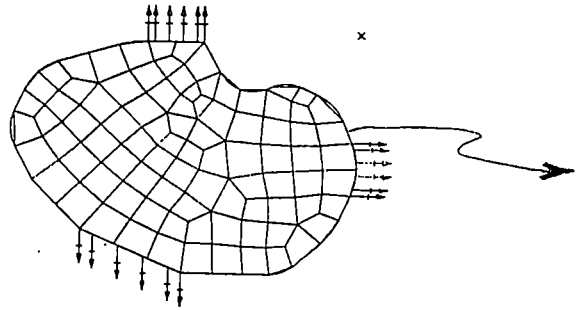


Arbitrary volume with applied tractions,
body force and inertia force.

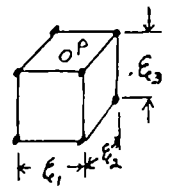
Figure 2.1 Arbitrary volume subjected to surface tensions, body force and inertia force.



Arbitrary volume with applied tractions, body force and inertia force.



Volume divided into subdomains (elements).
Body and inertia forces incorporated into elements.
Surface tractions applied to element boundaies.



$$u_{iP} = \sum_{j=1}^{8} N_{ij}(\xi_k)\, q(t)_j$$

Figure 2.2 Simplified representation of finite element process.

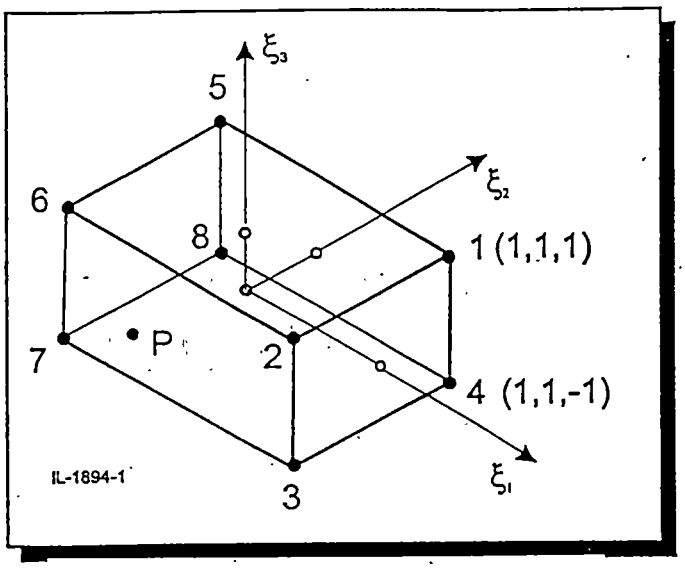


Figure 2.3 Isoparametric brick element.

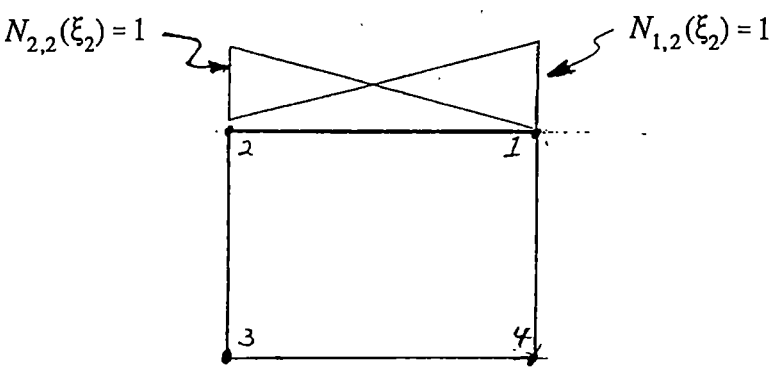


Figure 2.4 Linear variation of shape function.

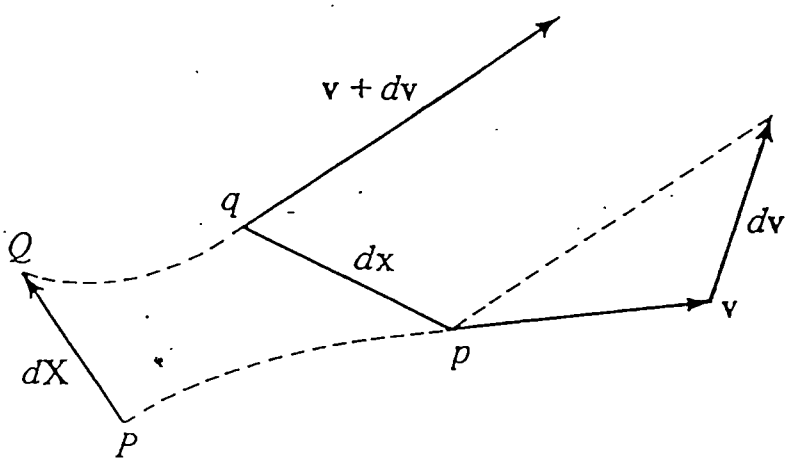
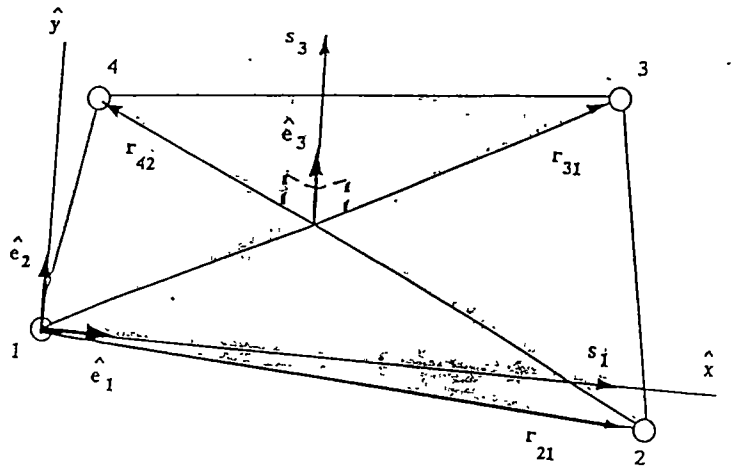
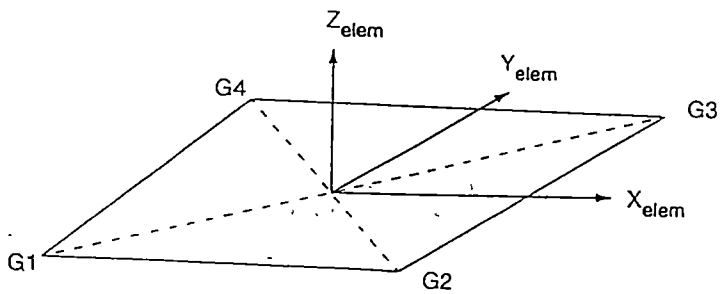


Figure 2.5 Relative motion of two particles.
Source: Malvern, Lawrence E. Introduction to the Mechanics of a Continuous Medium. Prentice-Hall, New Jersey, 1969.



(A) Co-rotational coordinate system.



(B) Element coordinate system.

Figure 2.6 Co-rotational and element coordinate systems.
Source: Hallquist, John O., comp. LS-DYNA Theoretical Manual. Livermore, CA: Livermore Software Technology Corporation, 1998.

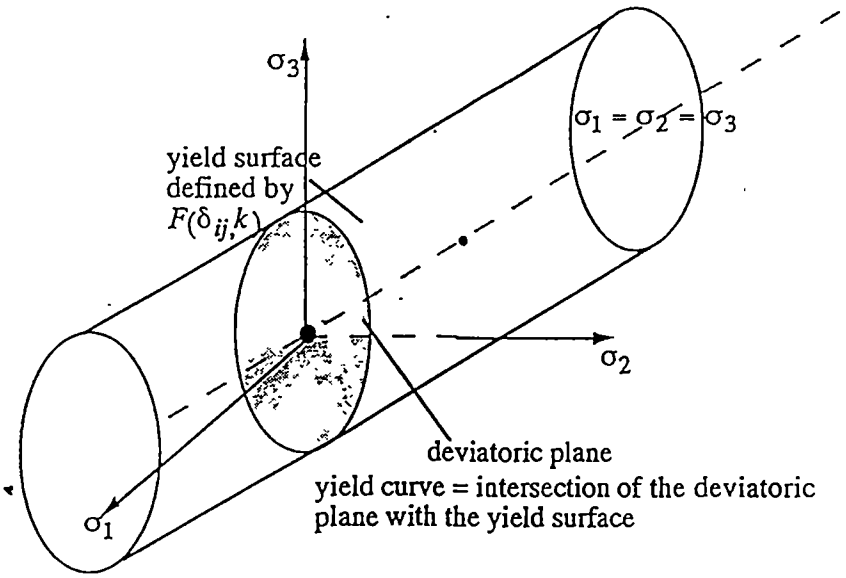


Figure 2.7 Isotropic elastic-plastic yield surface.
Source: MacNeal-Schwendler Corporation. MSC/DYTRAN Version 4.0 Users Manual. Los Angeles: MacNeal-Schwendler, 1997.

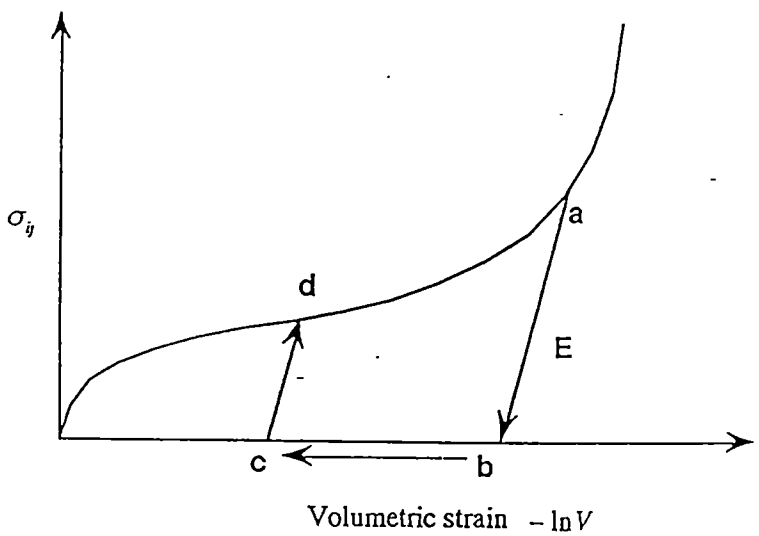


Figure 2.8 Crushable foam stress-strain curve.
Source: MacNeal-Schwendler Corporation. MSC/DYTRAN Version 4.0 Users Manual. Los Angeles: MacNeal-Schwendler, 1997.

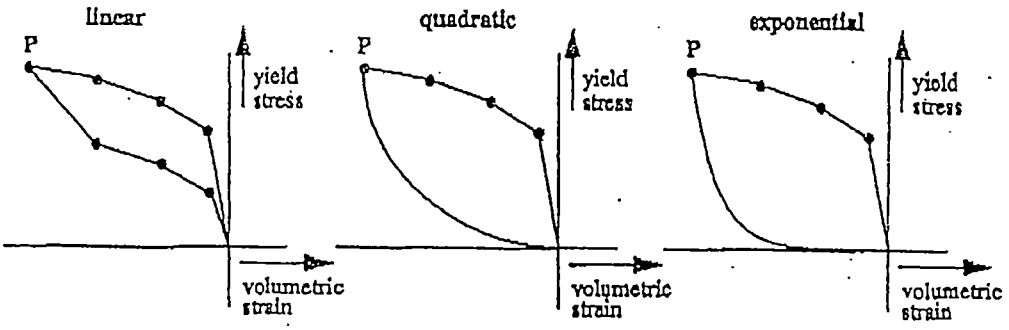


Figure 2.9 Crushable foam unloading stress-strain curve.
Source: MacNeal-Schwendler Corporation. MSC/DYTRAN Version 4.0 Users Manual. Los Angeles: MacNeal-Schwendler, 1997.

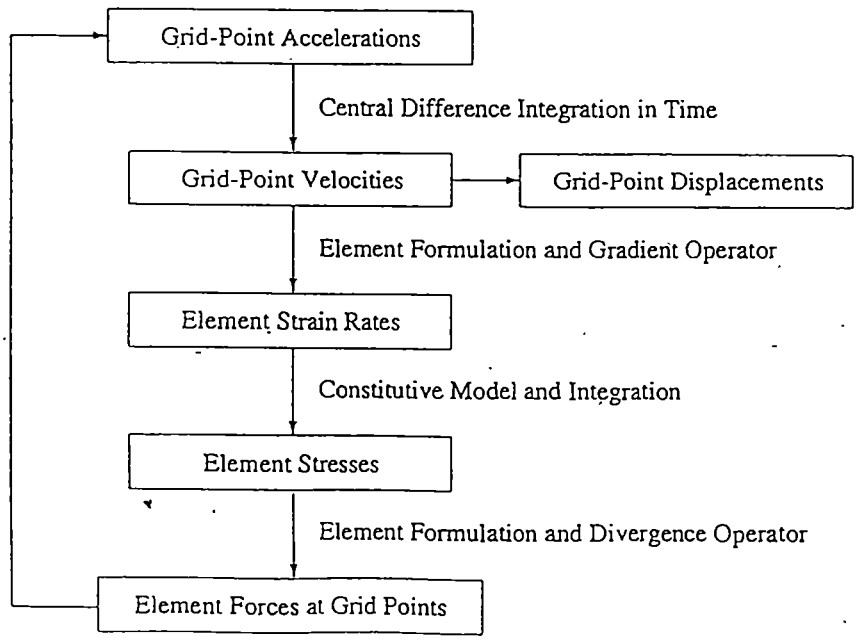
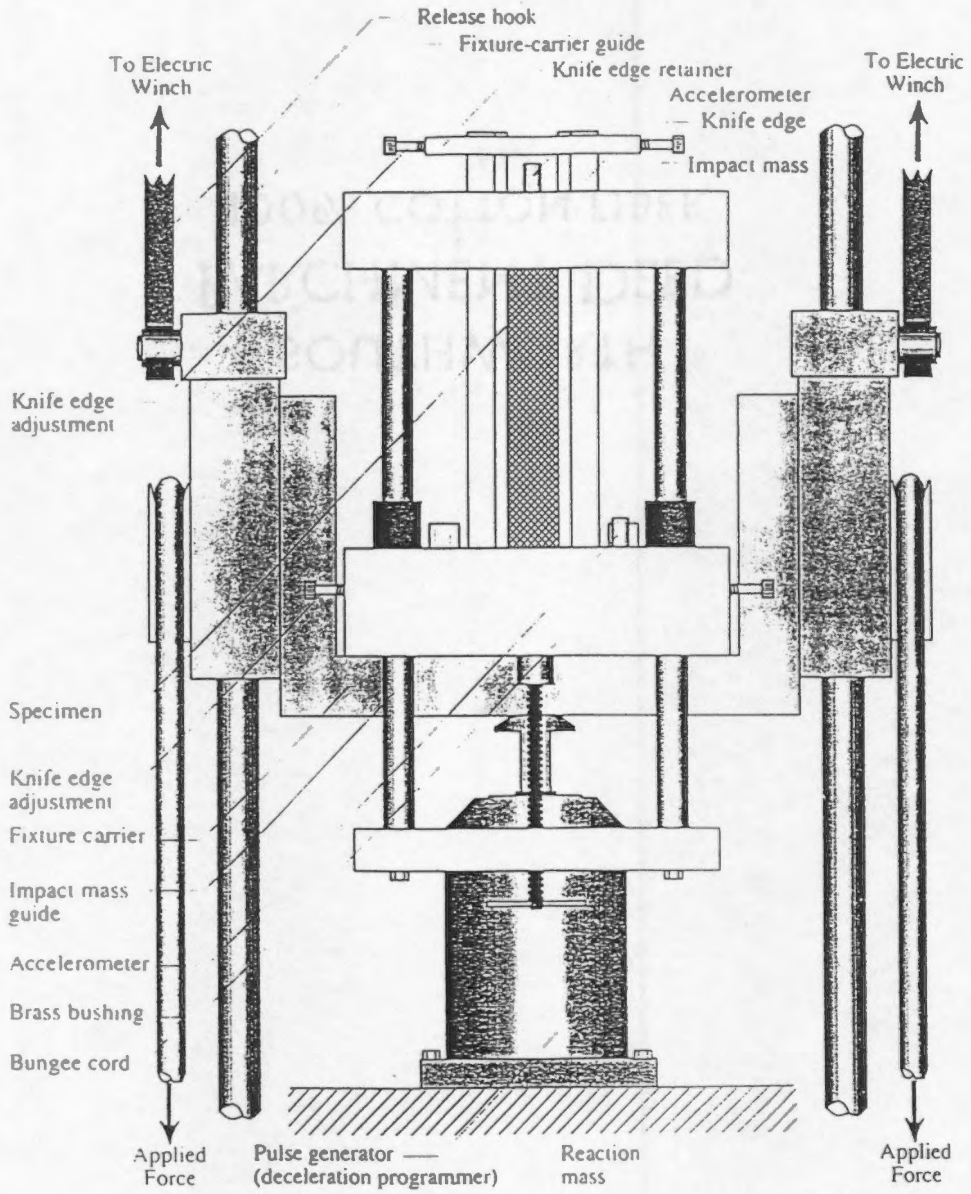


Figure 2.10 Solution process flow chart.
Source: MacNeal-Schwendler Corporation. MSC/DYTRAN Version 4.0 Users Manual. Los Angeles: MacNeal-Schwendler, 1997.



Schematic of dynamic crush set-up. When released from a predetermined height the fixture carrier, aided by the bungee cords and gravity, accelerates towards the pulse generator which at impact produces the deceleration pulse. When high enough decelerations are reached, crushing of the specimen initiates. Force, velocity and displacement are calculated from the accelerometer signals.

Figure 3.1 Crush fixture.
Source: Kellas, Sotiris. "An Experimental Investigation into the Energy Absorption Performance of Composite Beam Webs for Aircraft Subfloor Applications" American Helicopter Society National Technical Specialist's Meeting on Rotorcraft Structures, Williamsburg, Va. 1995.

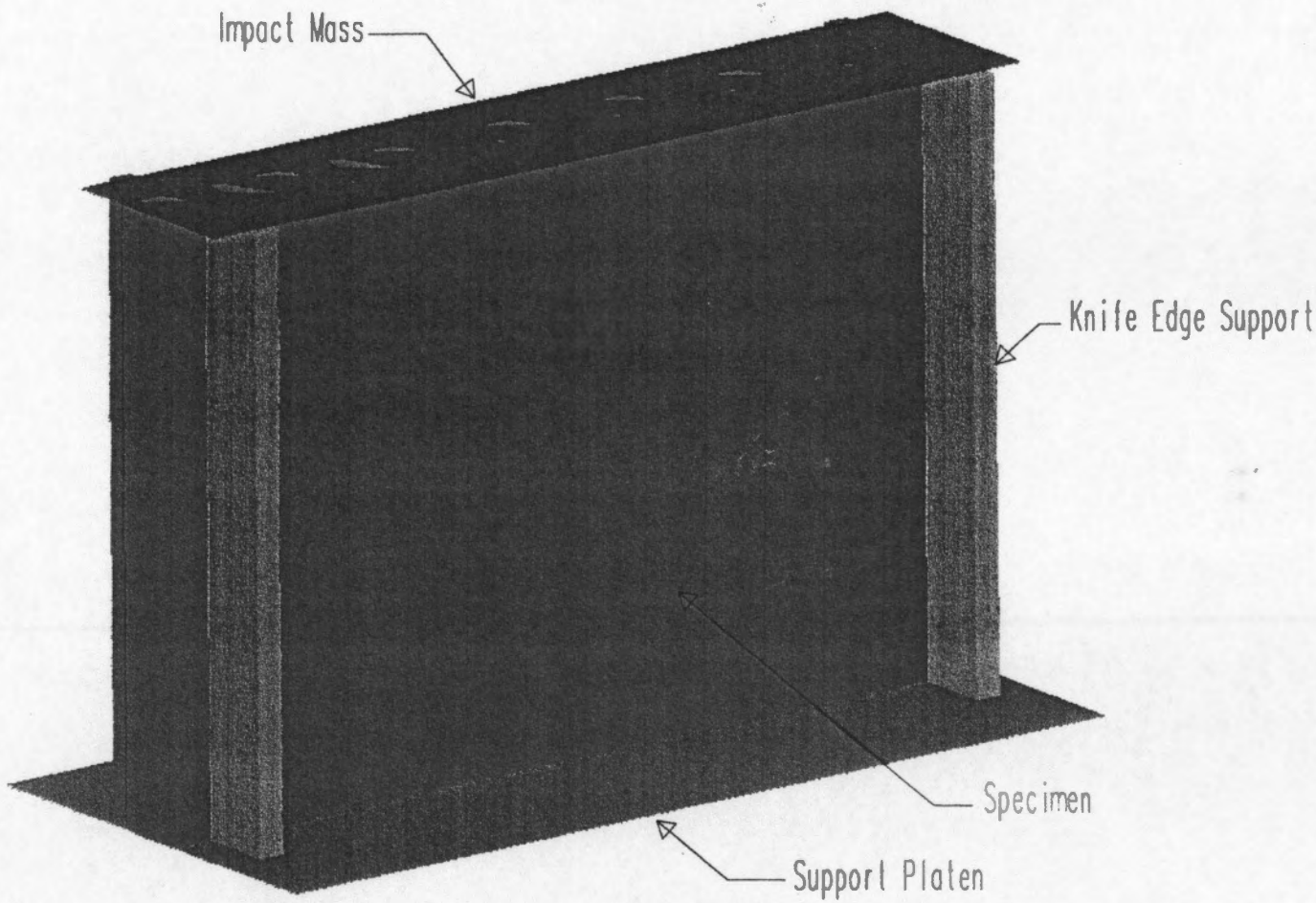


Figure 3.2 Model representation of specimen and crush fixture.

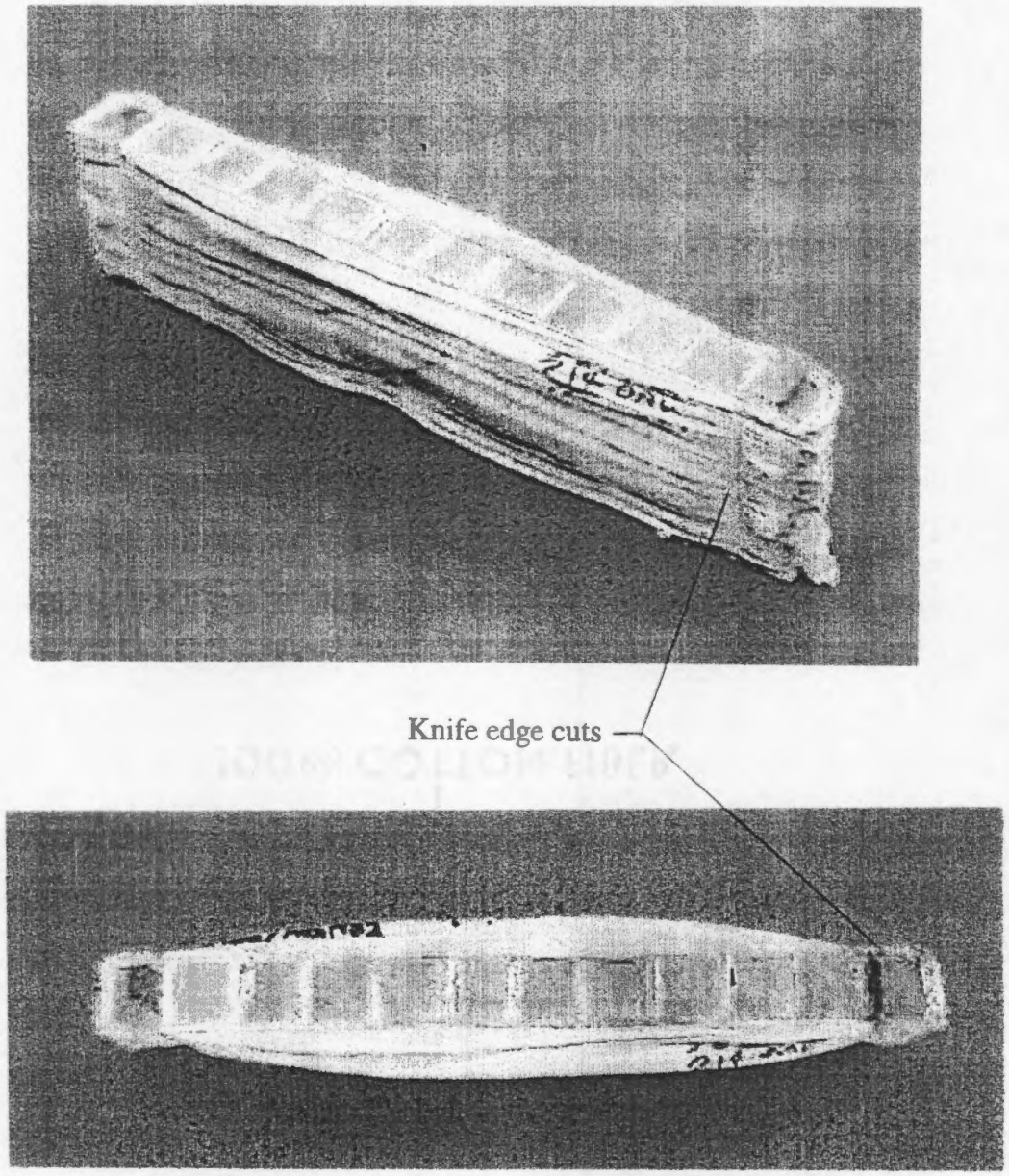


Figure 3.3 Knife edge cuts made into specimen.

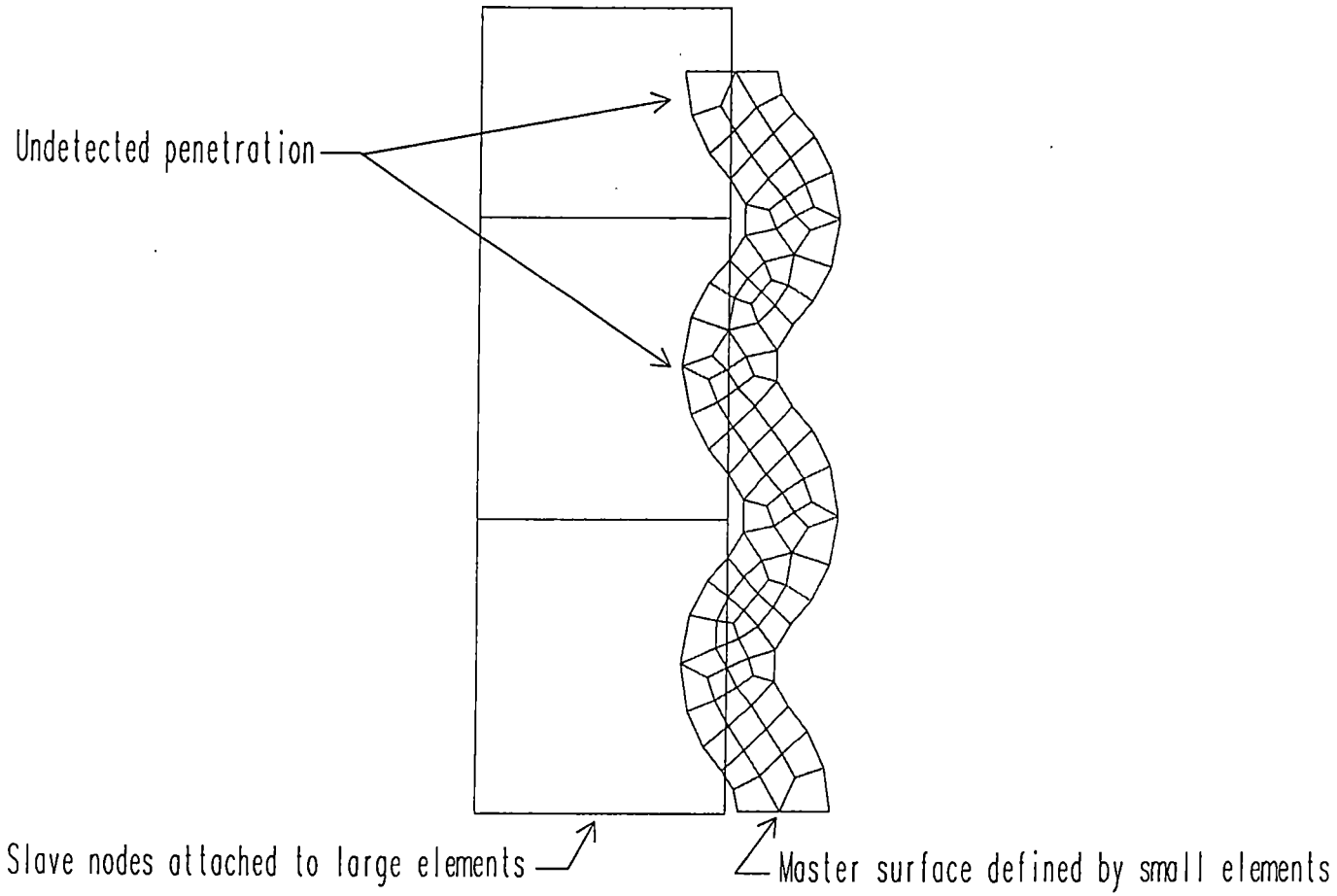


Figure 3.4 Refined master surface mesh penetration into coarse slave mesh.

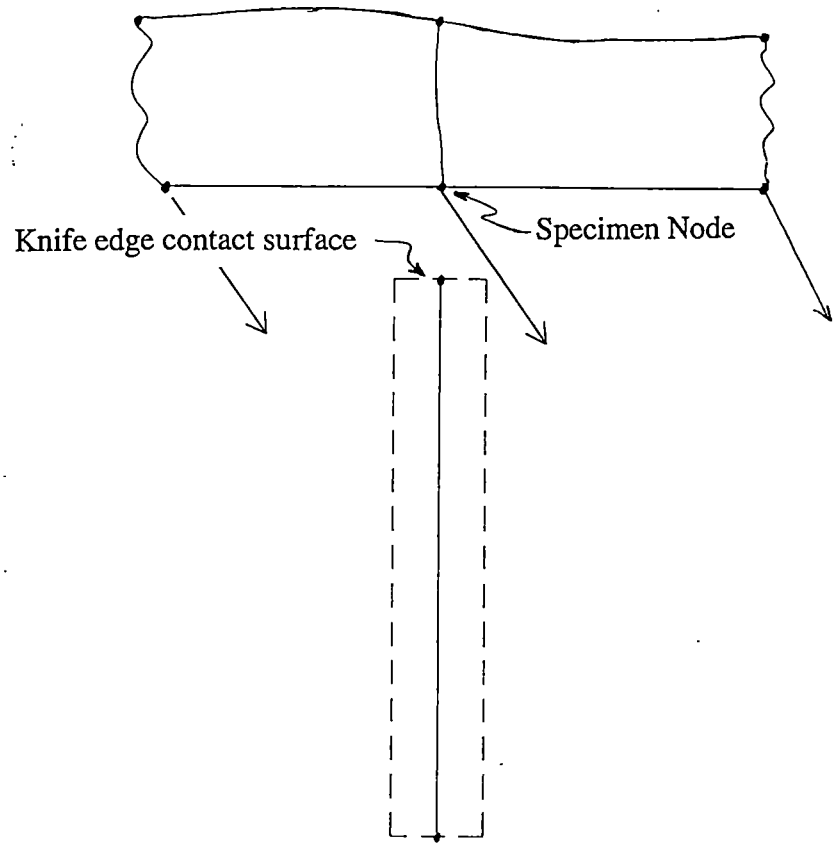


Figure 3.5 Slave node missing knife edge.

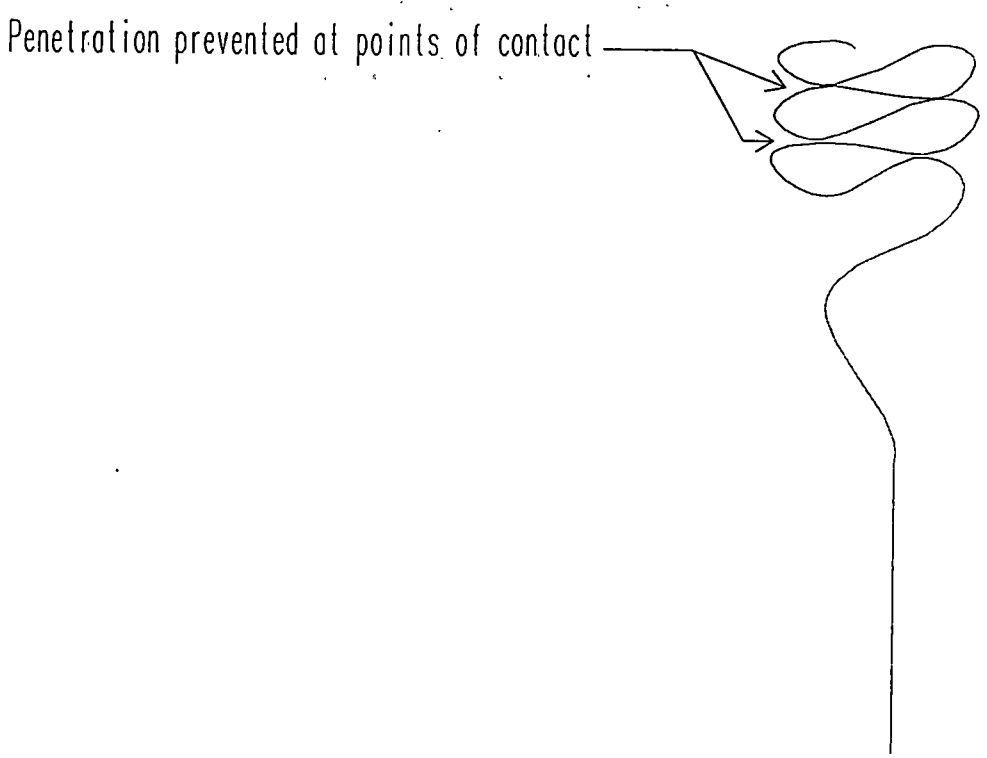


Figure 3.6 Single surface contact surface.

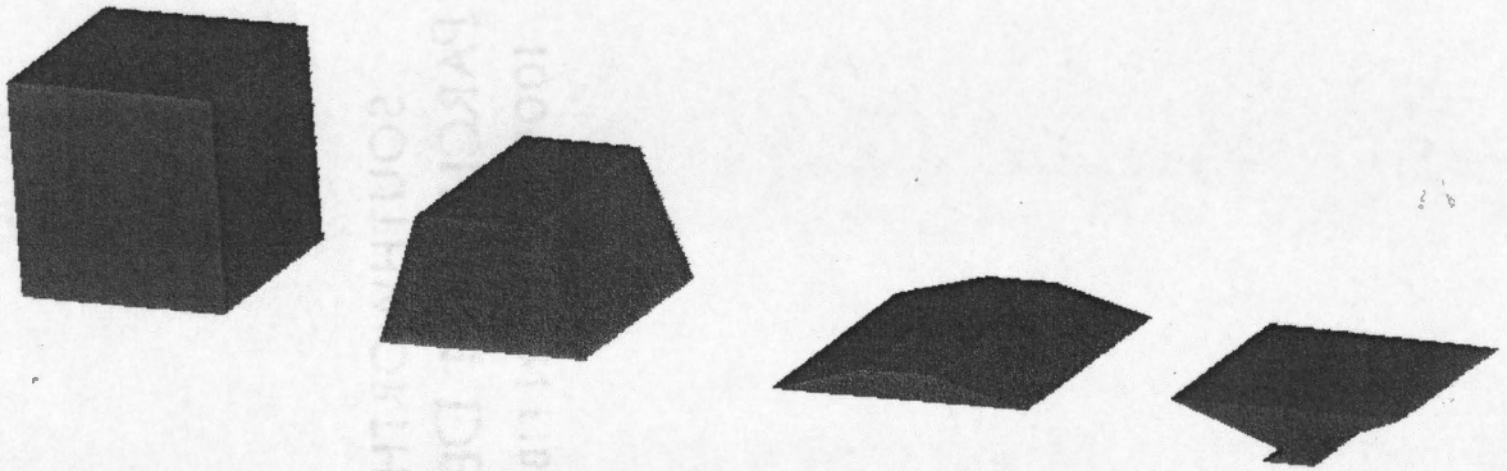


Figure 3.7 Inversion of solid element.

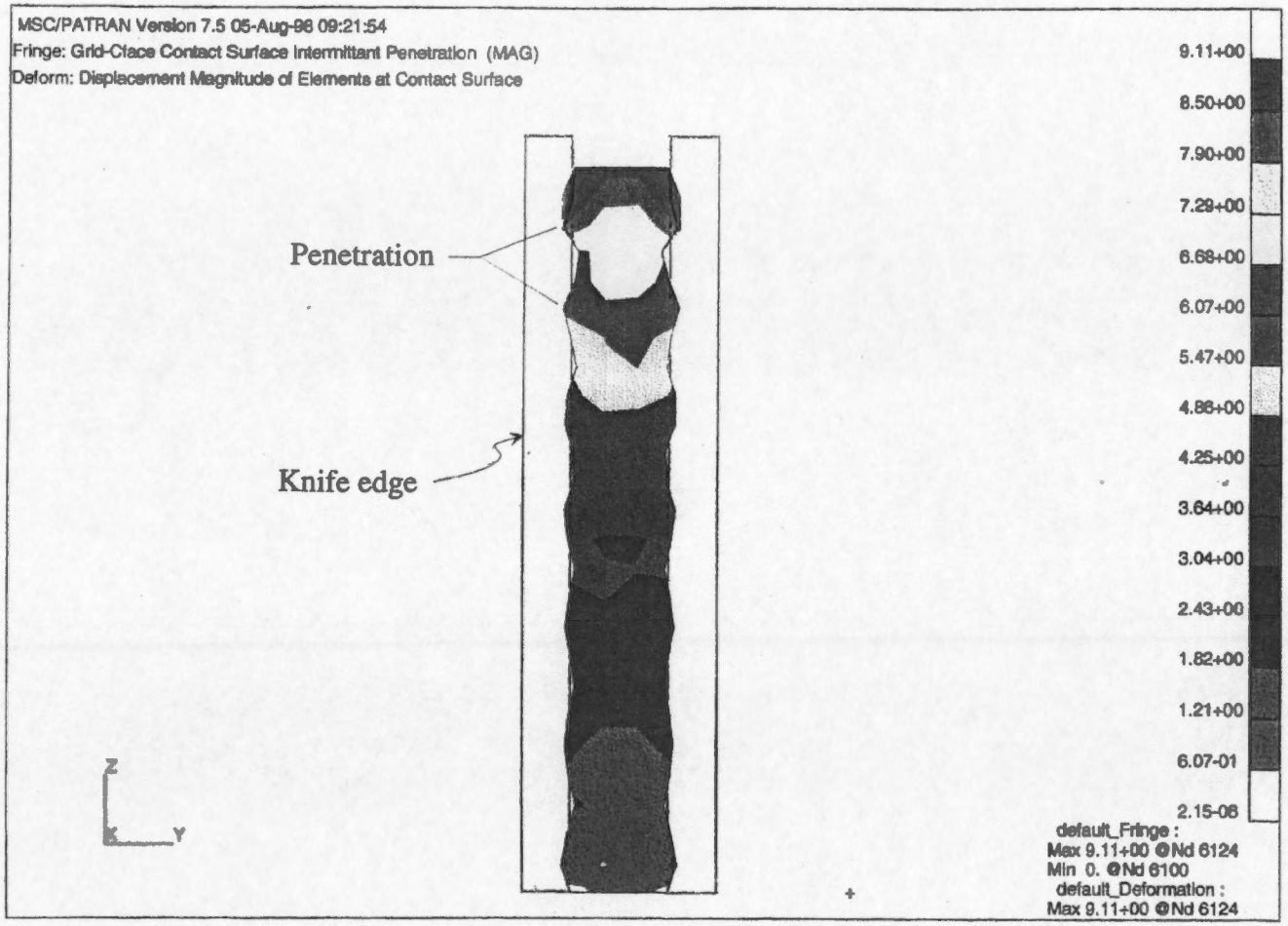


Figure 3.8 Intermittent penetration of knife edge contact surface.

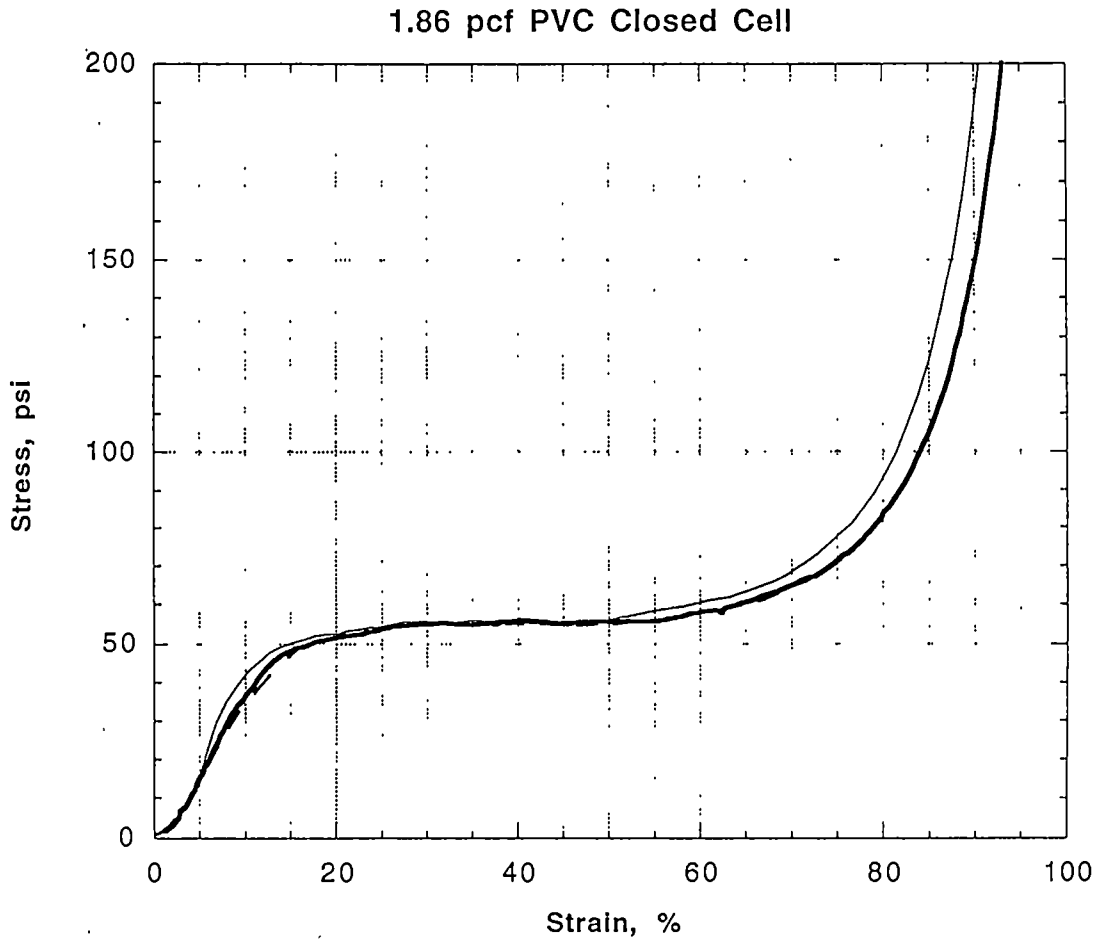


Figure 4.1 PVC foam compressive stress-strain curve.

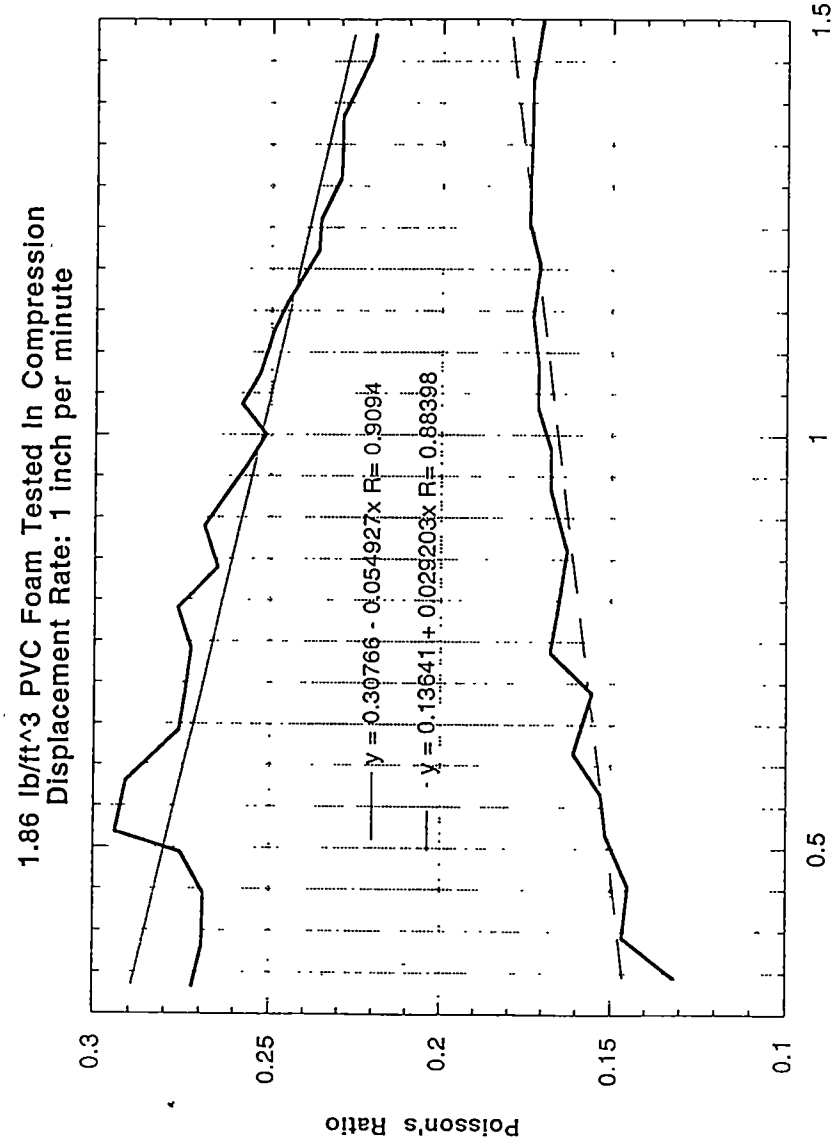


Figure 4.2 PVC foam Poisson's ratio versus strain.

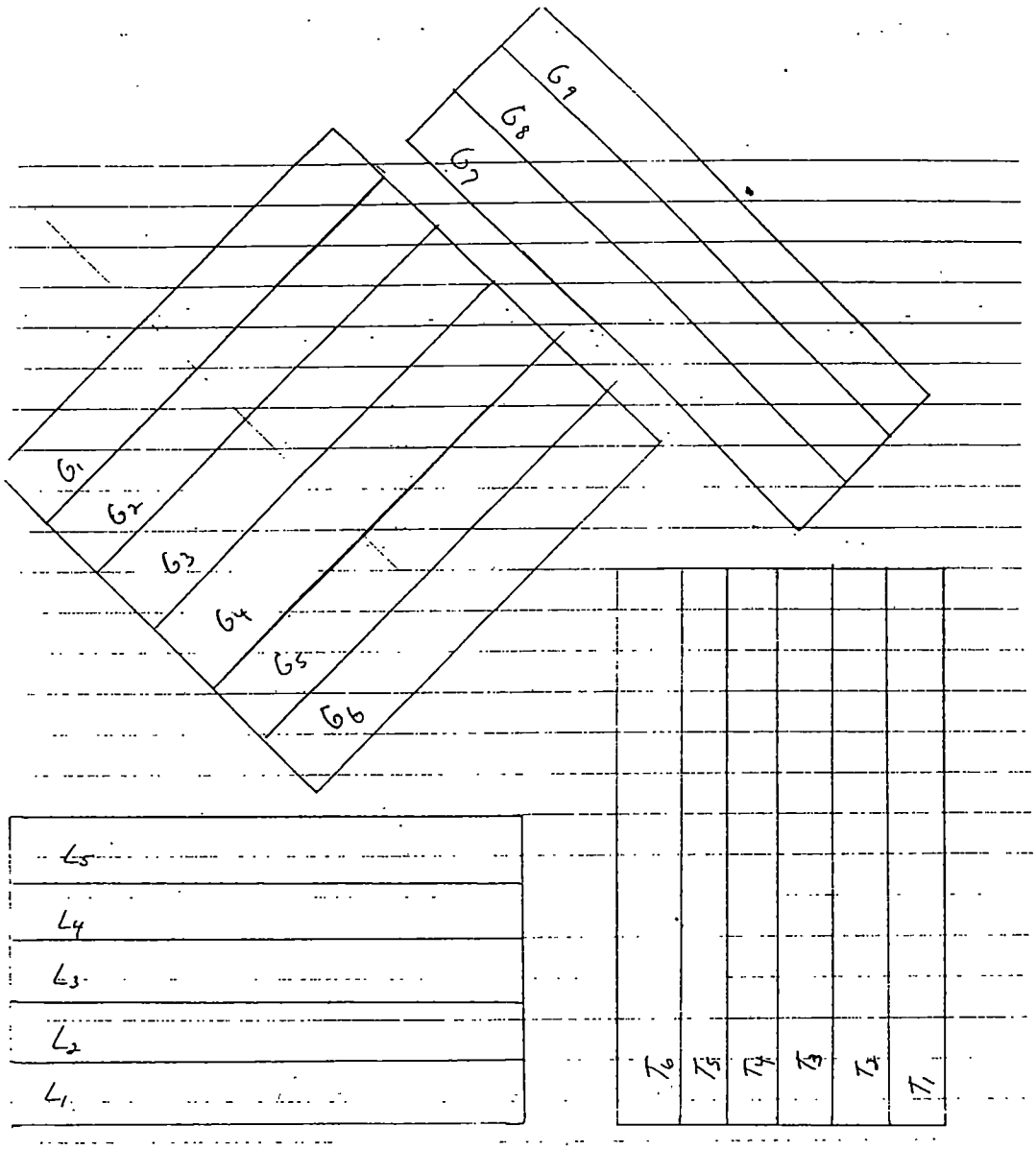


Figure 4.3 Glass/epoxy sheet 1 coupon layout.

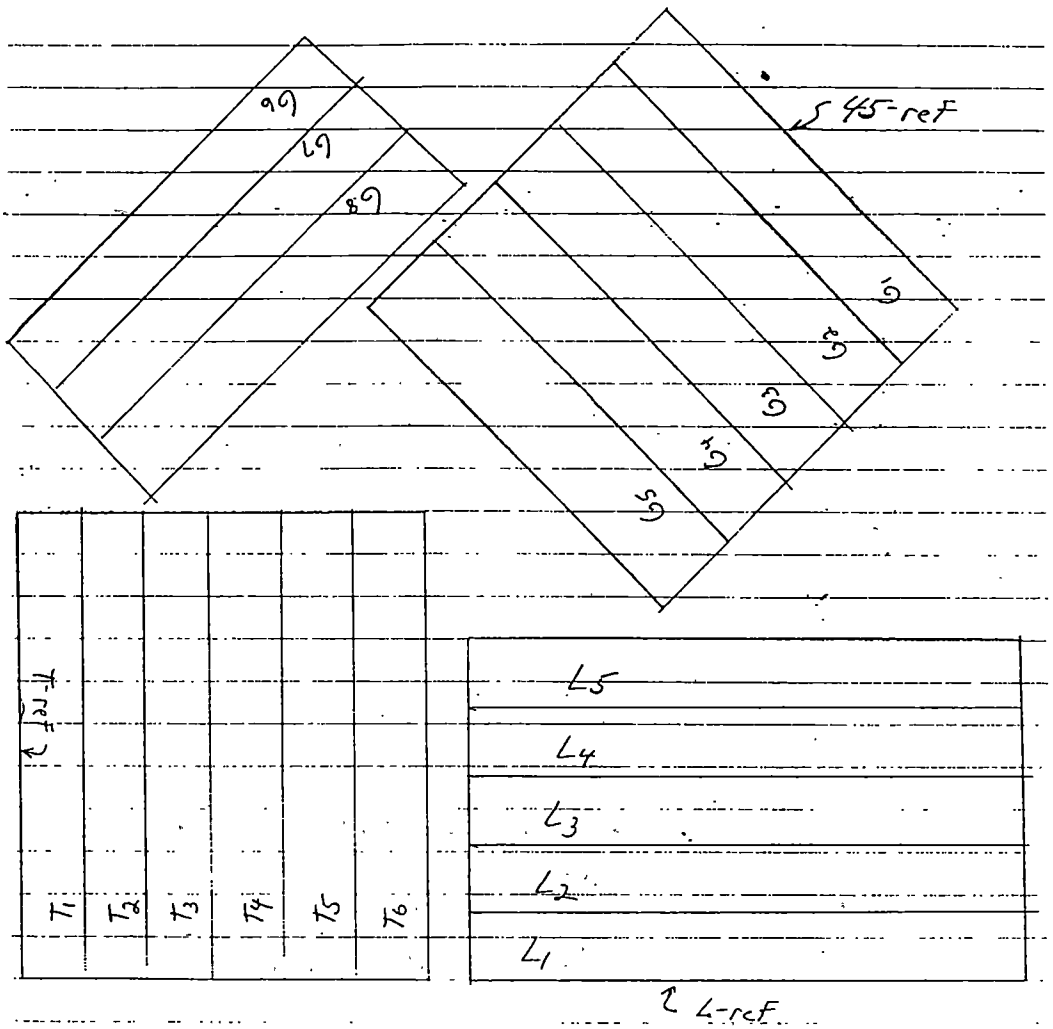


Figure 4.4 Glass/epoxy sheet 2 coupon layout.

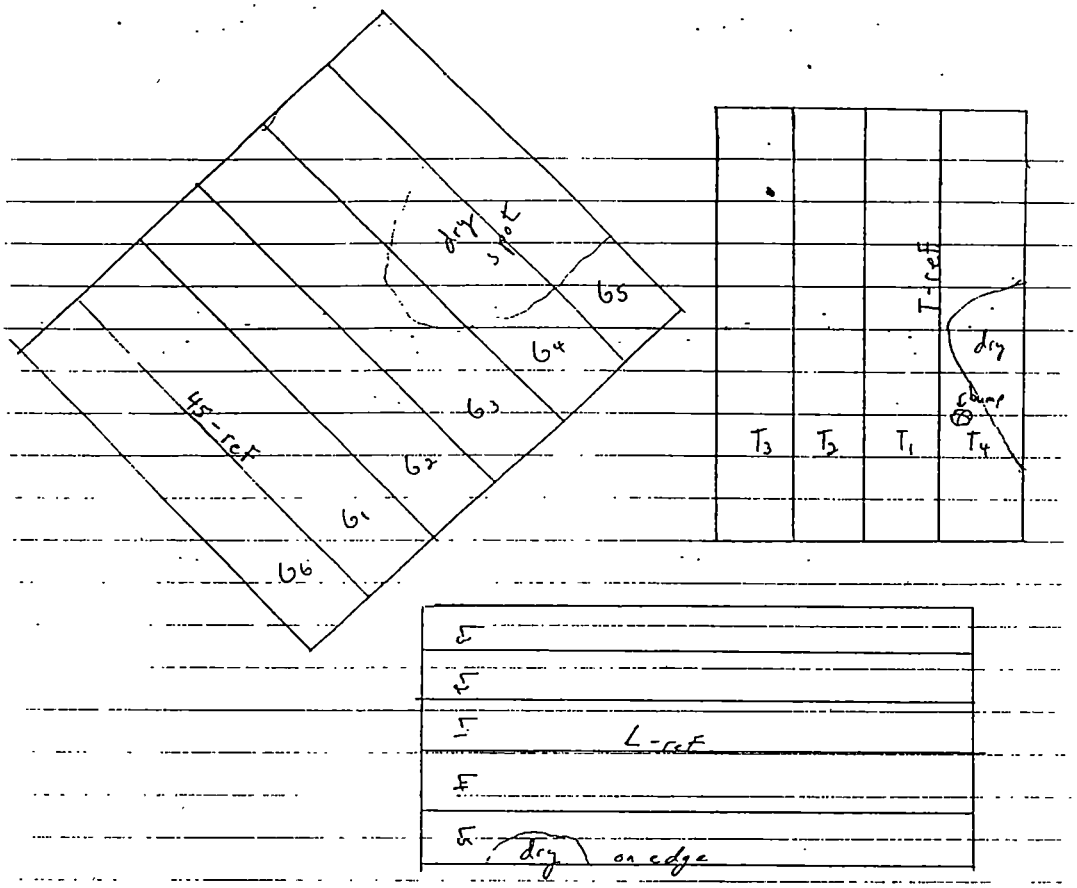


Figure 4.5 Kevlar/epoxy sheet 1 coupon layout.

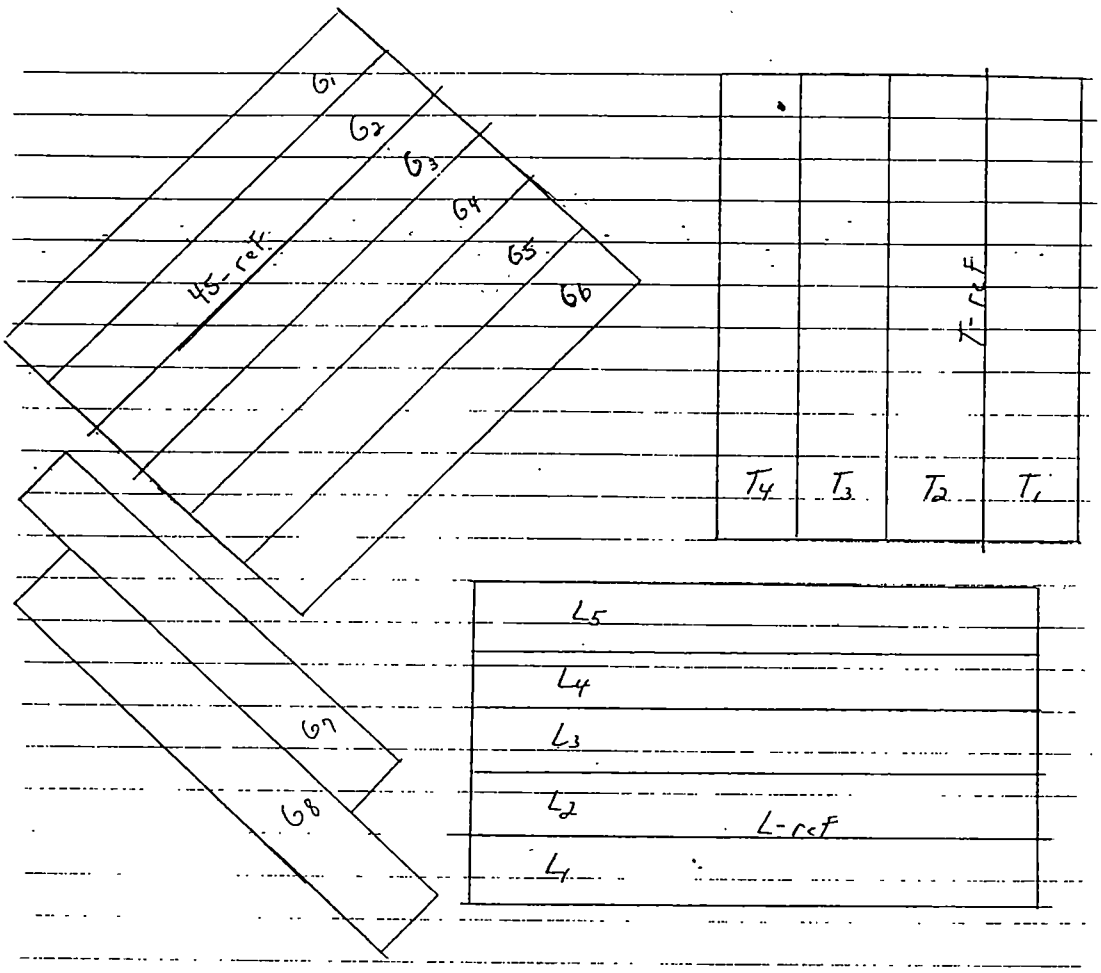
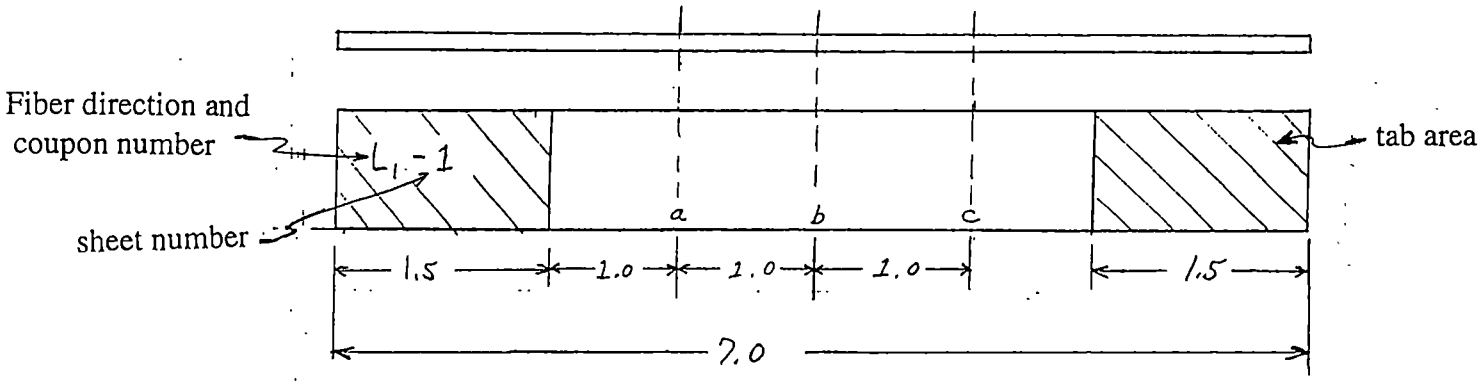


Figure 4.6 Kevlar/epoxy sheet 2 coupon layout.

Sample Measurement Points for Width and Thickness



Note that points a, b, c are taken relative to the fiber direction/sheet number label on the coupon.

Figure 4.7 Coupon measurement points.

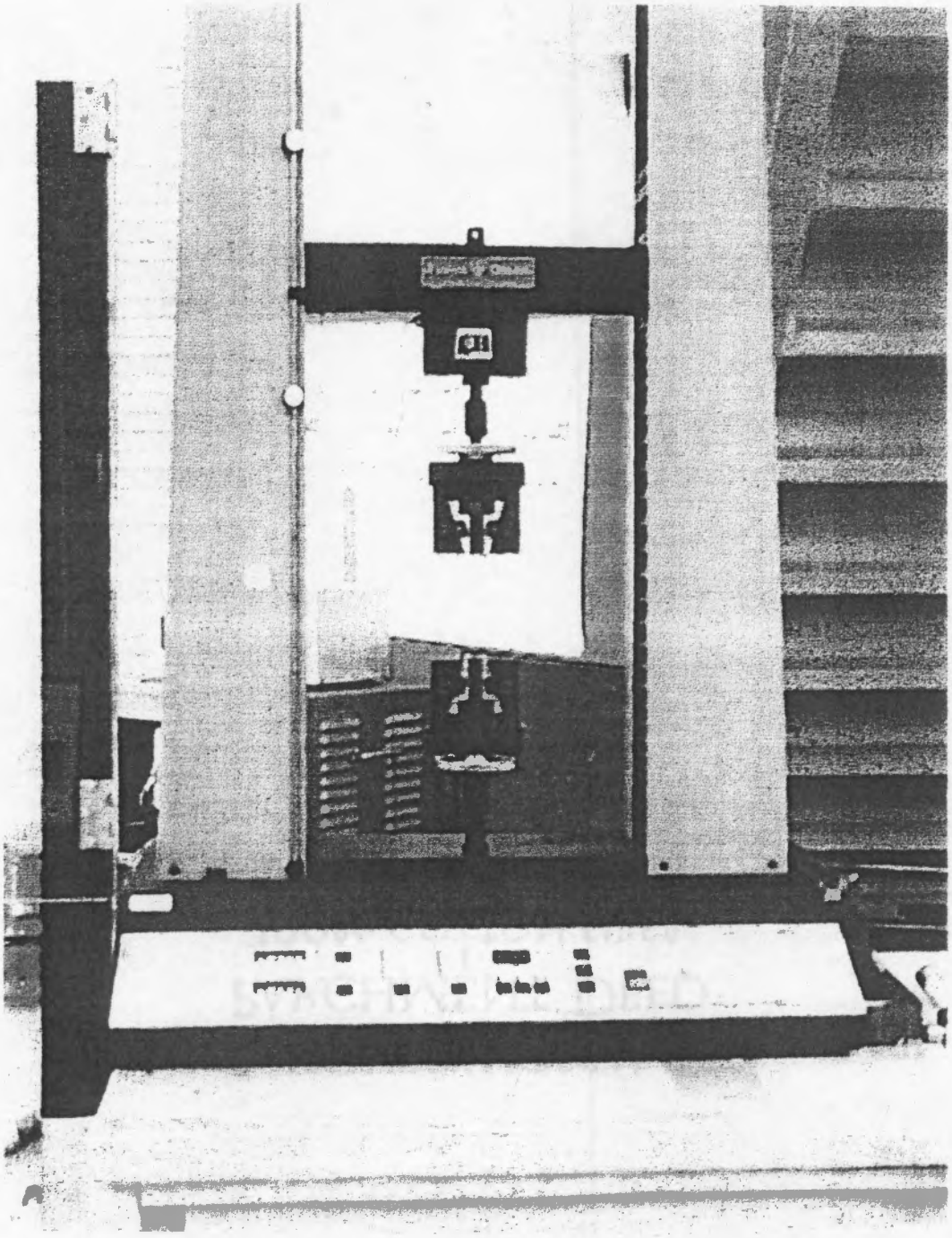


Figure 4.8 Tinius-Olsen coupon pull fixture.

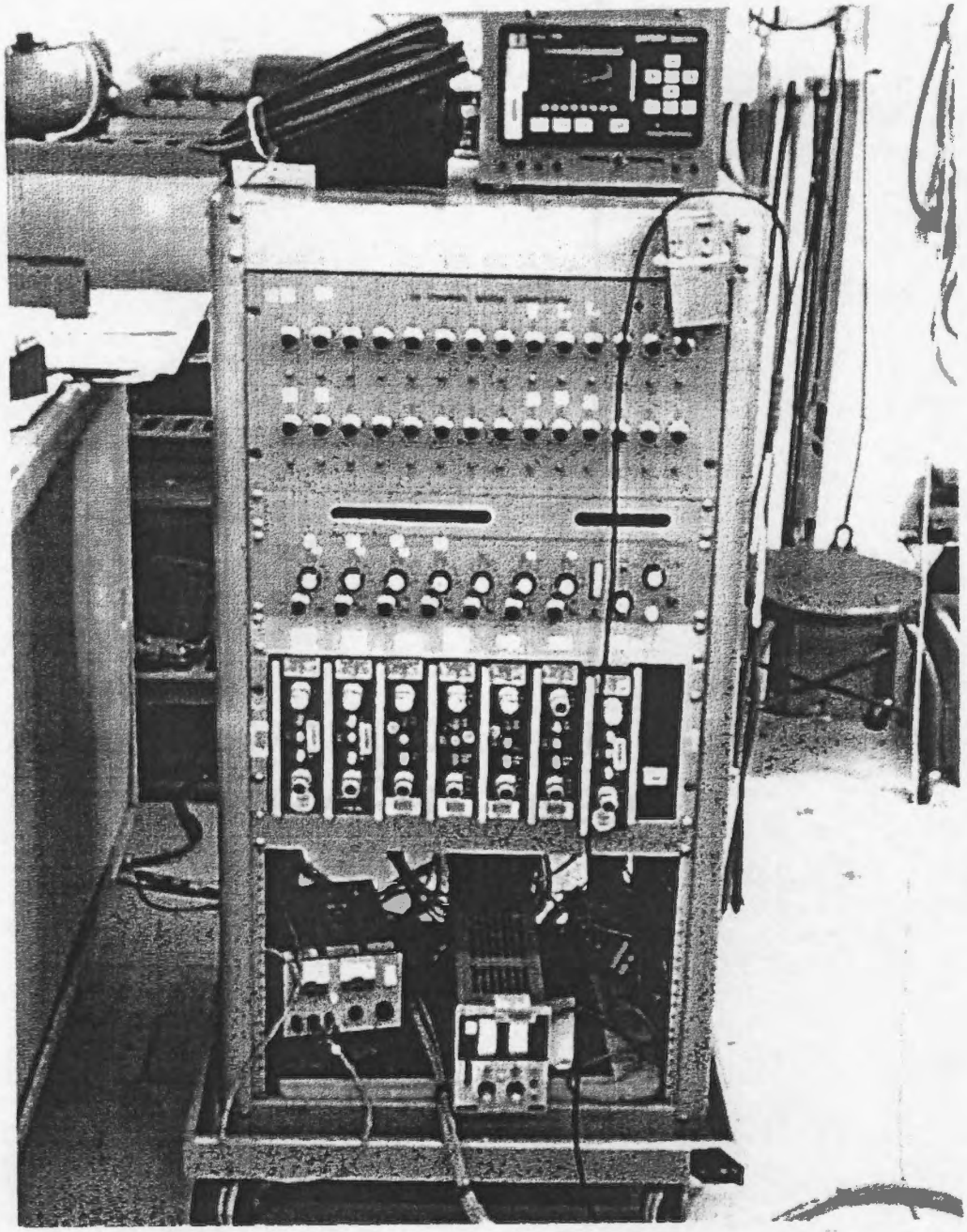


Figure 4.9 NEF 122 strain gage amplifiers.

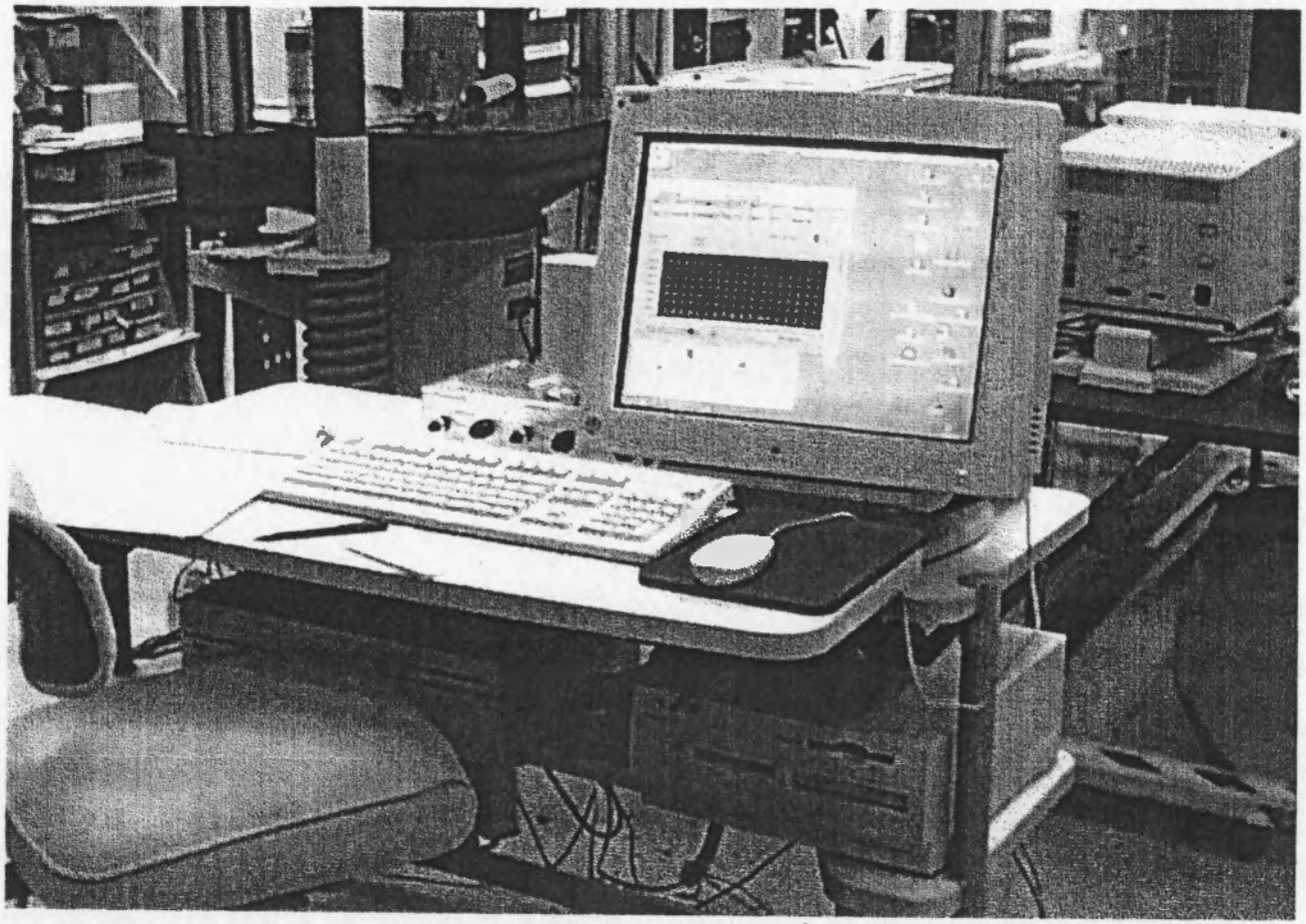


Figure 4.10 Lab View data acquisition on MacIntosh P. C.

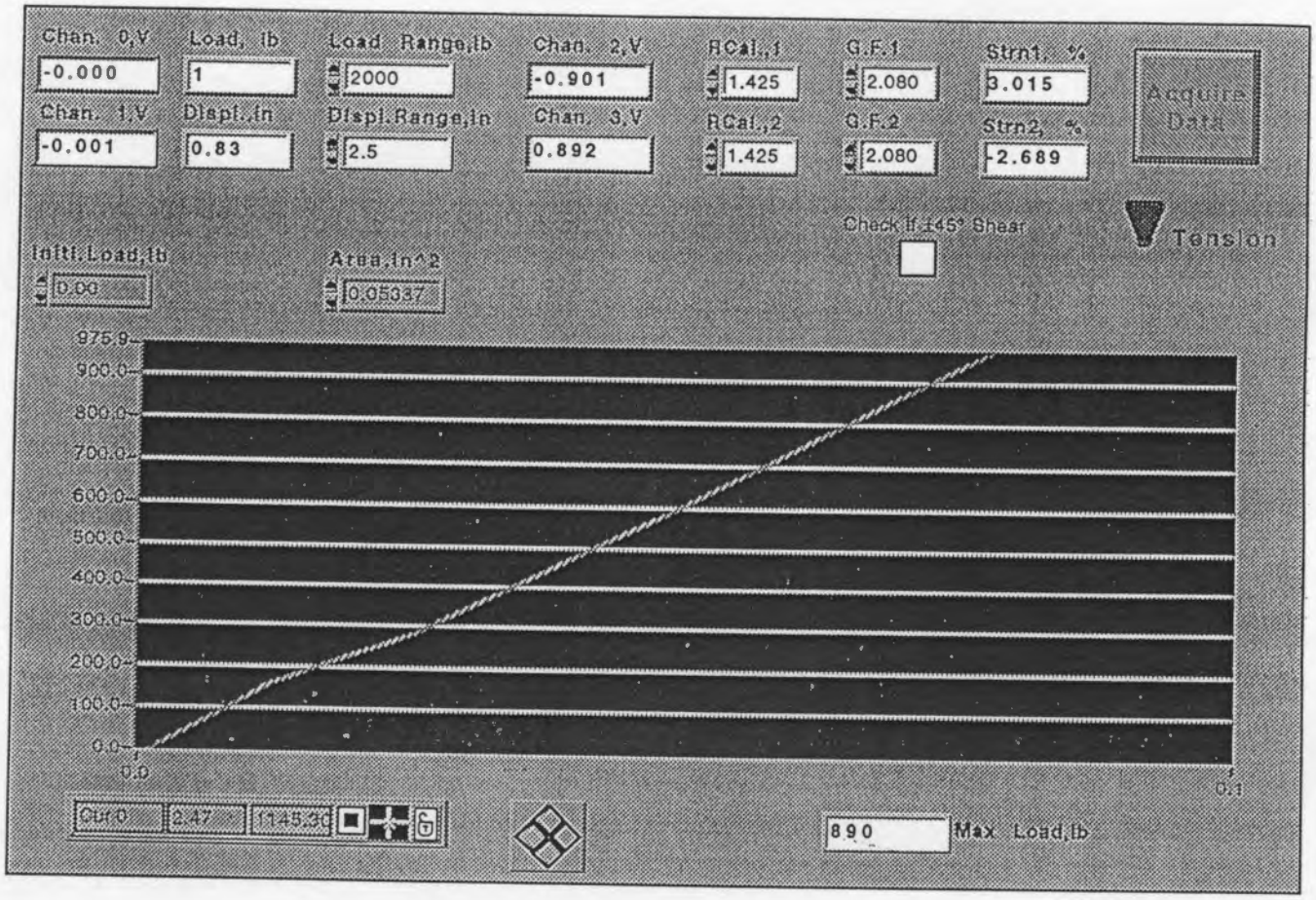


Figure 4.11 Lab View graphical interface.

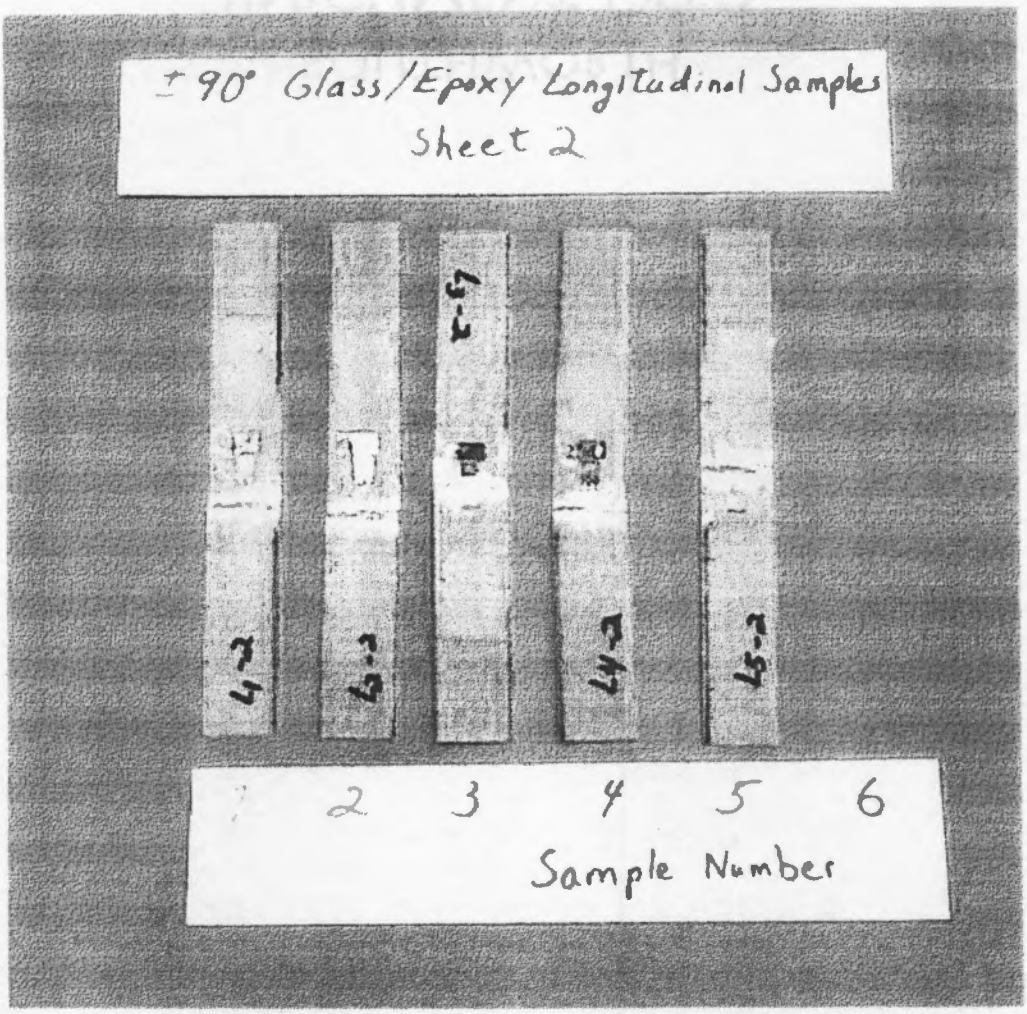


Figure 4.12 Glass/epoxy sheet 2 failed longitudinal coupons.

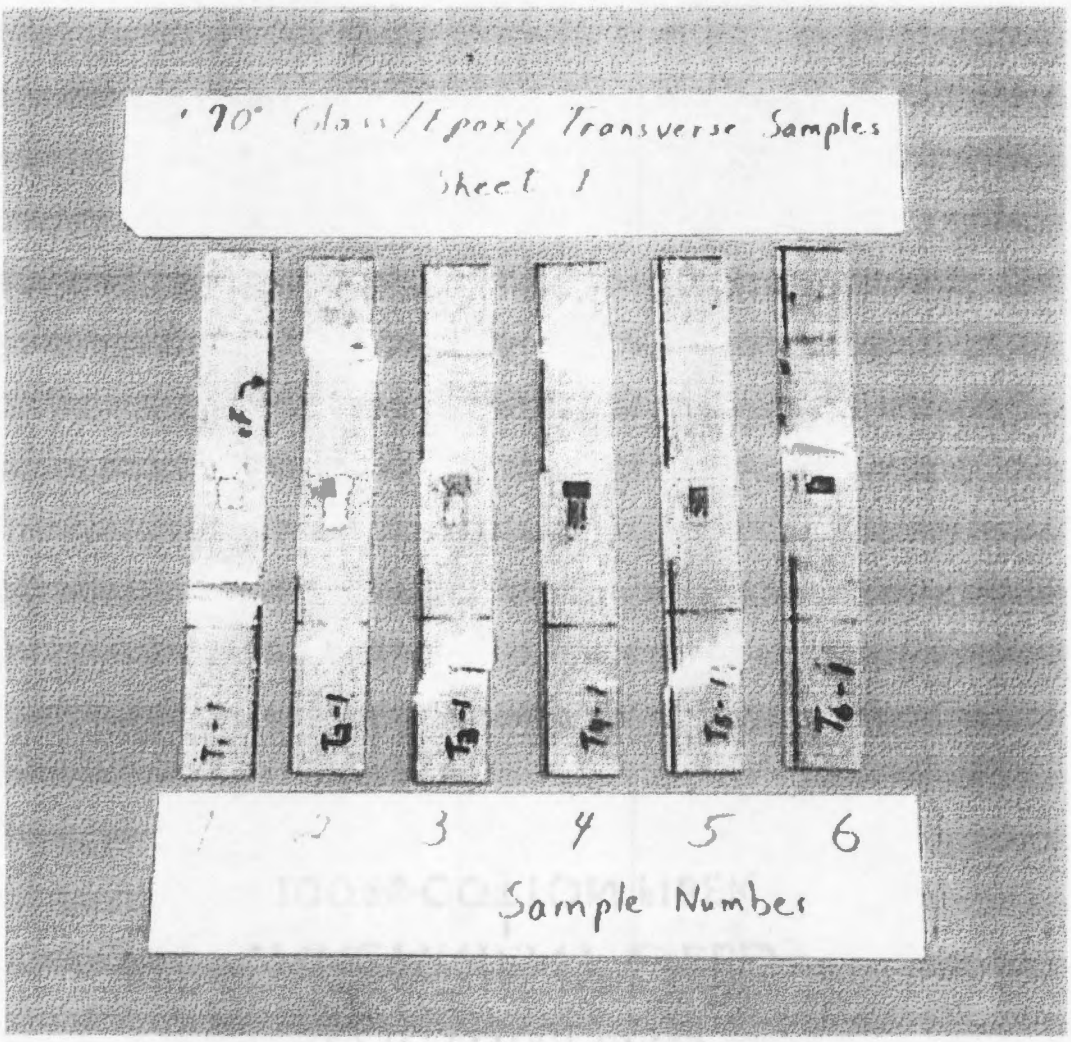


Figure 4.13 Glass/epoxy sheet 1 failed transverse coupons.

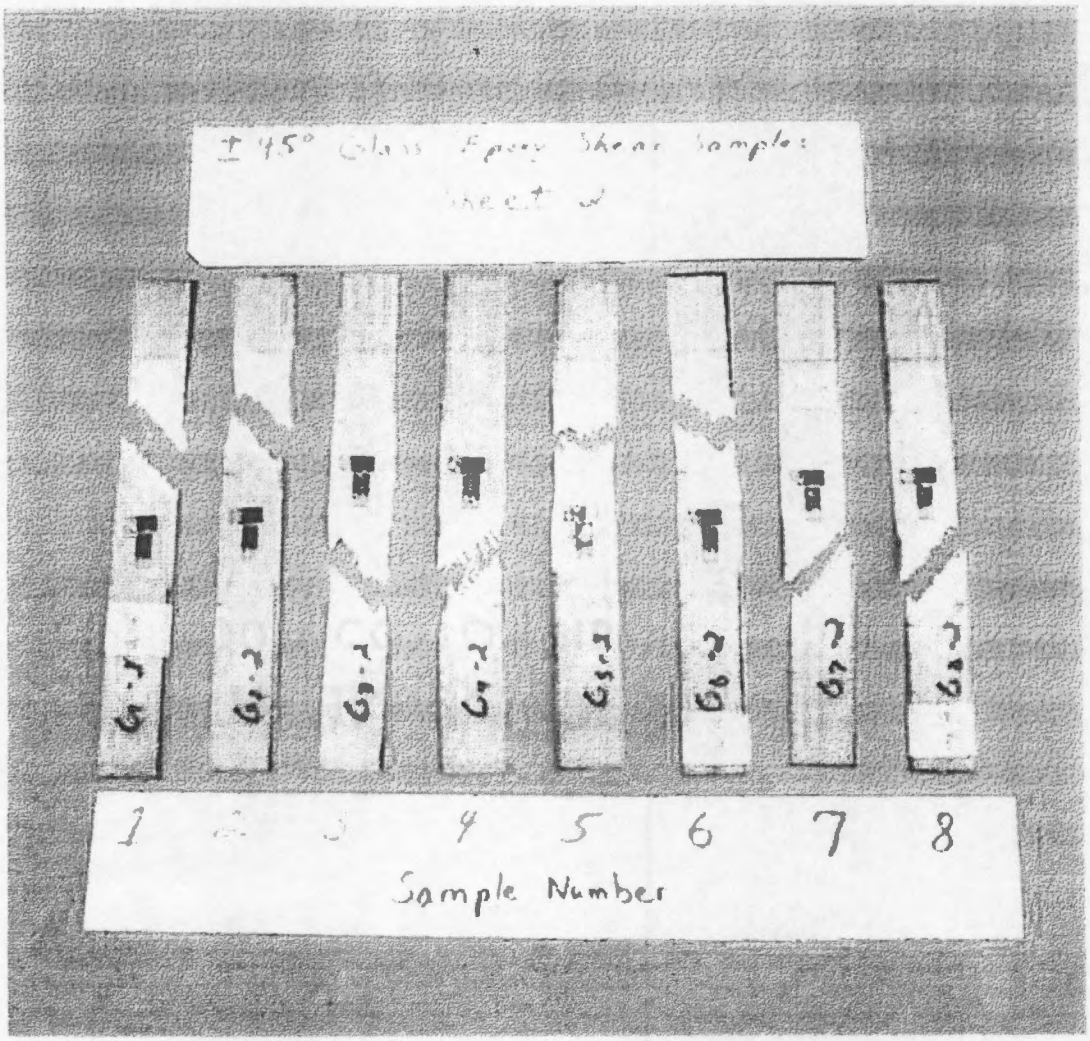


Figure 4.14 Glass/epoxy sheet 2 failed shear coupons.

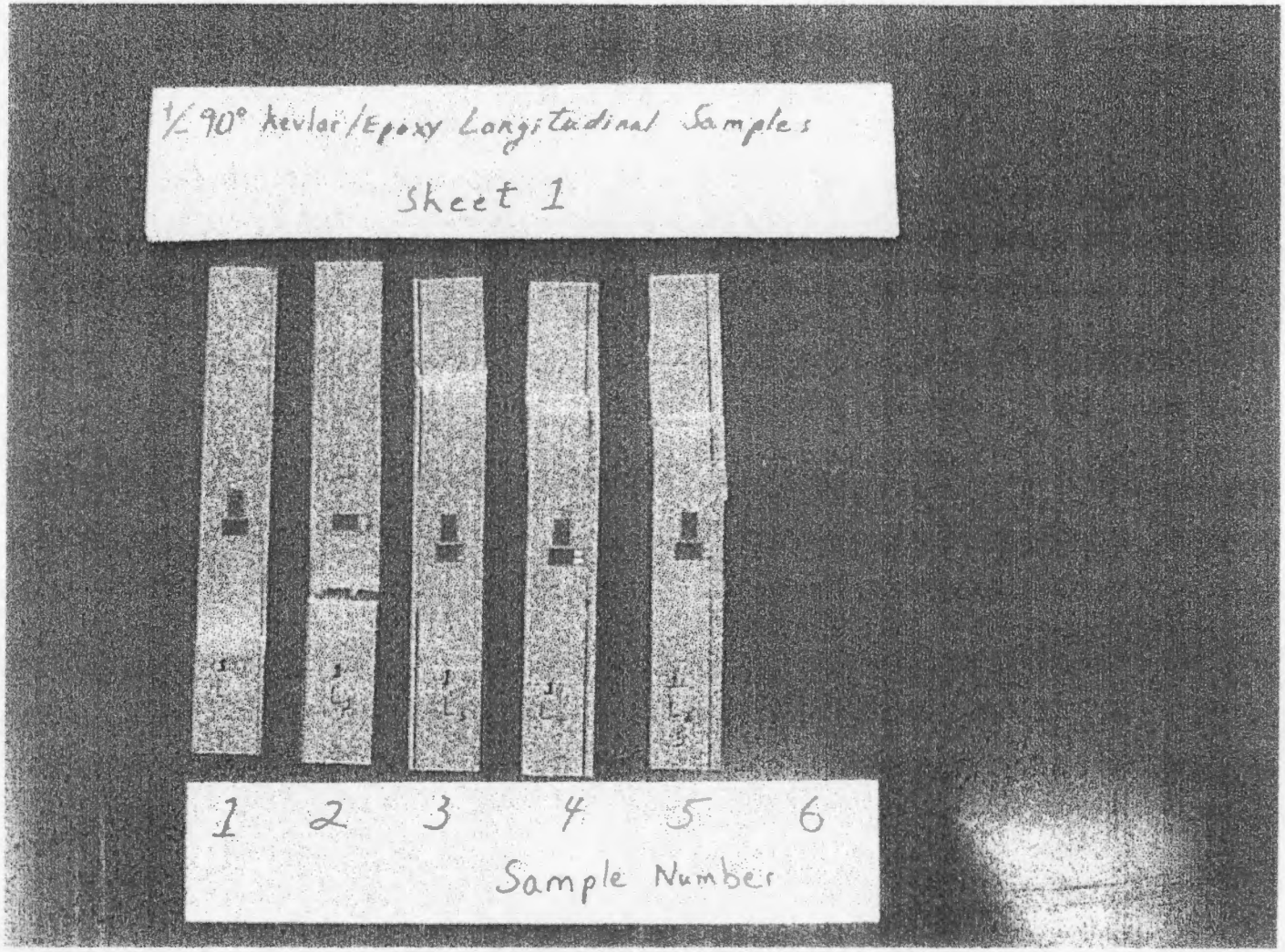


Figure 4.15 Kevlar/epoxy sheet 1 failed longitudinal coupons.

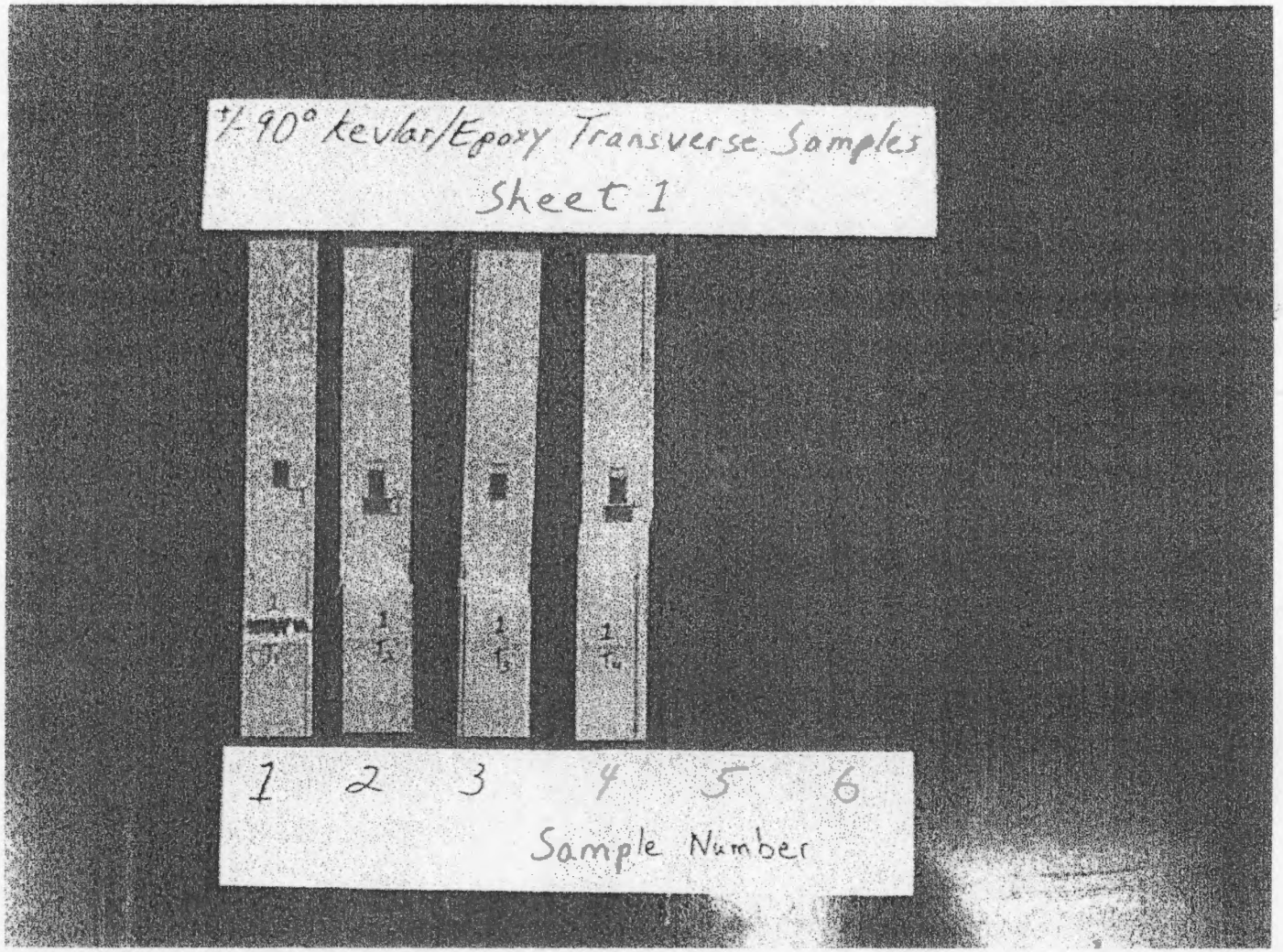


Figure 4.16 Kevlar/epoxy sheet 1 failed traverse coupons.

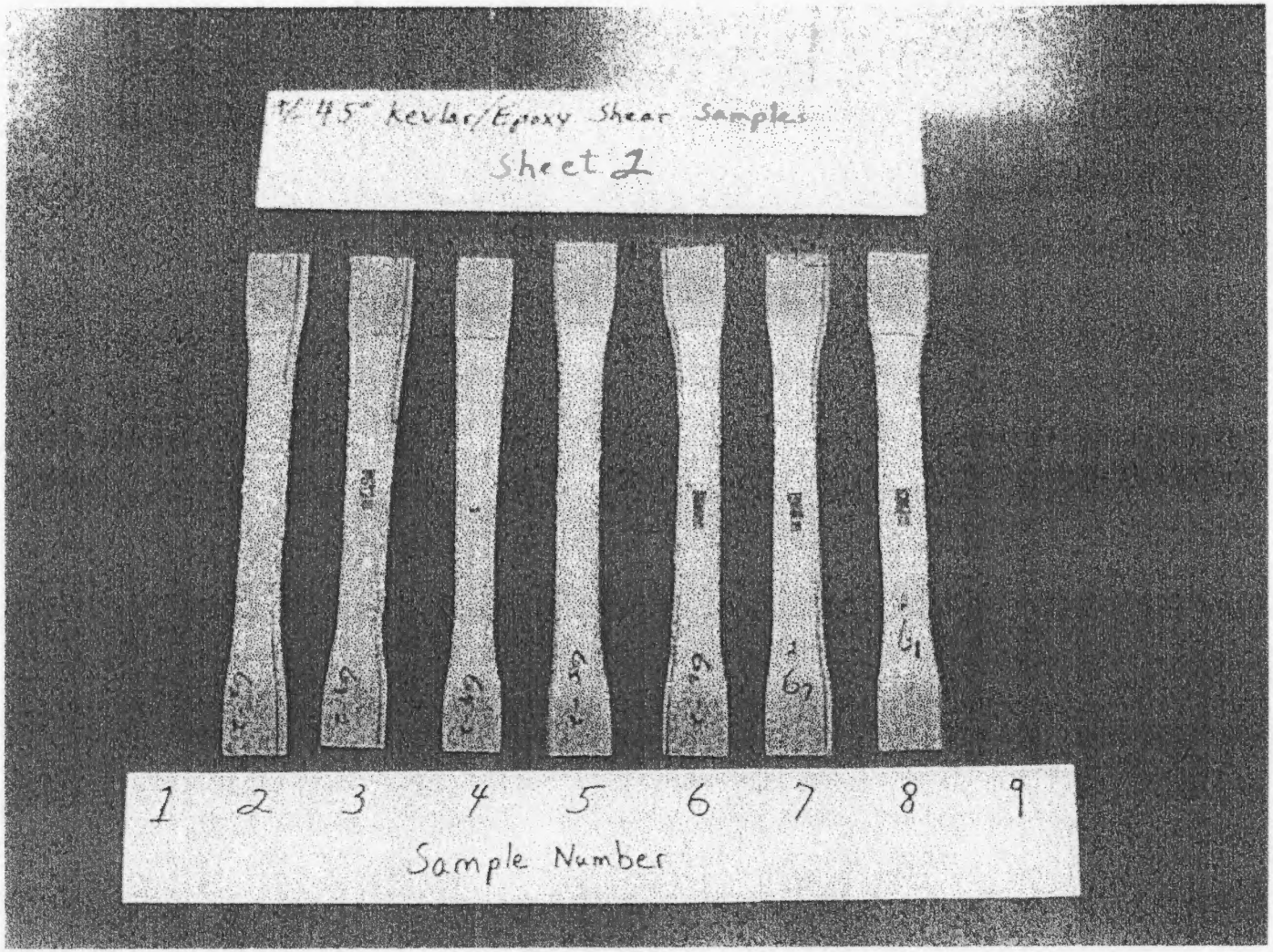


Figure 4.17 Kevlar/epoxy sheet 2 failed shear coupons.

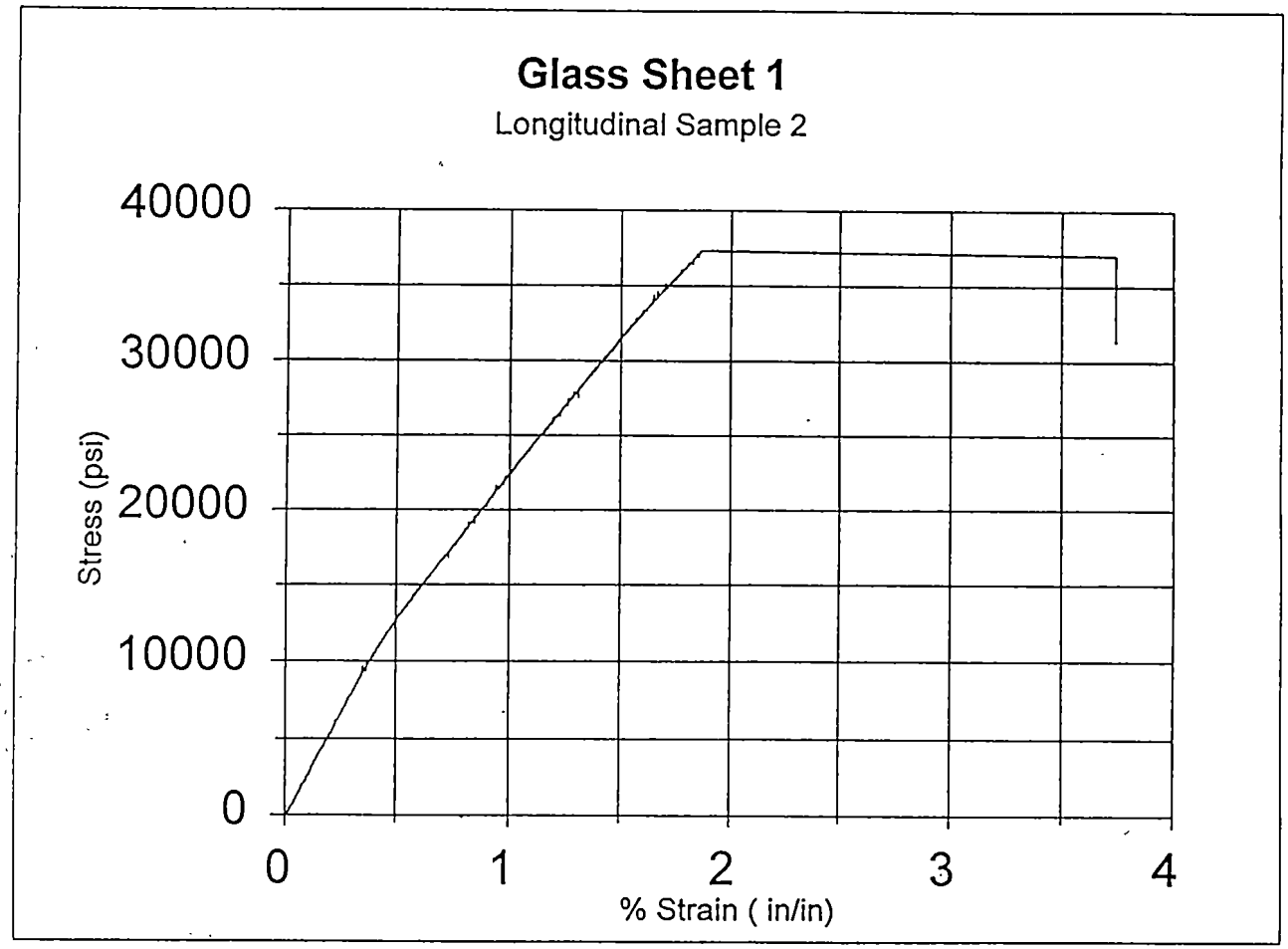


Figure 4.18 Representative glass/epoxy longitudinal stress-strain curve.

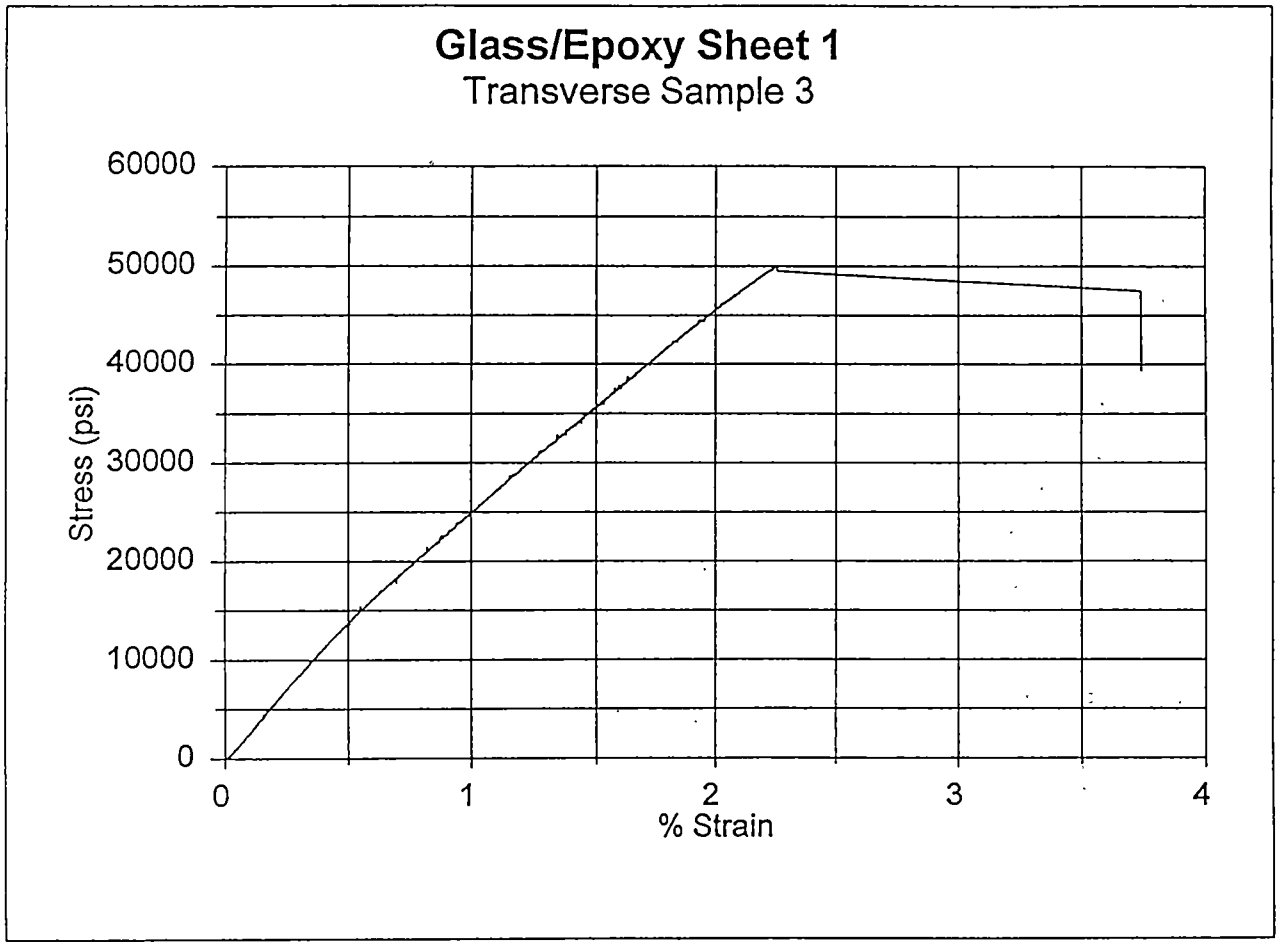


Figure 4.19 Representative glass/epoxy transverse stress-strain curve.

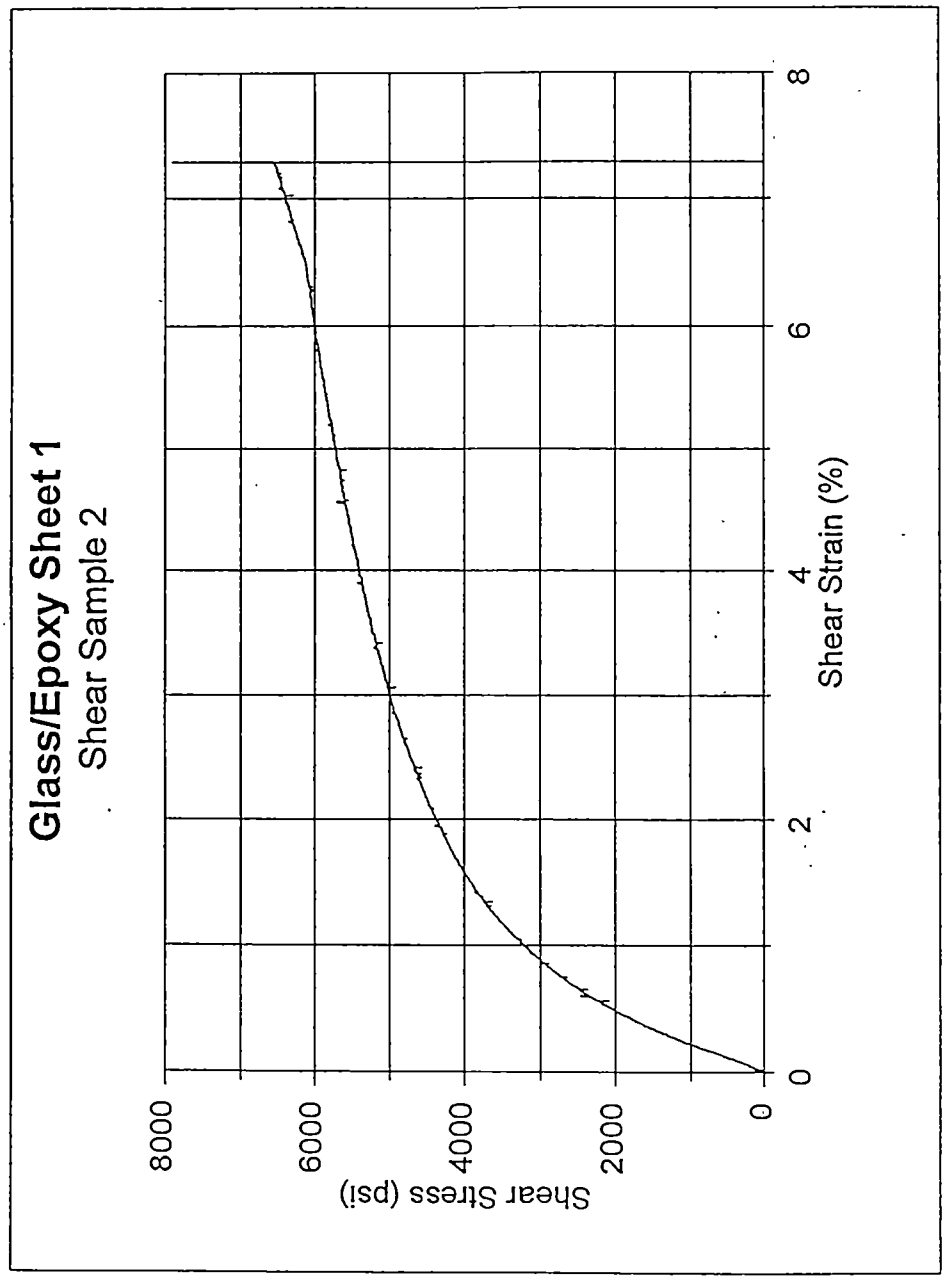


Figure 4.20 Representative glass/epoxy shear stress-strain curve.

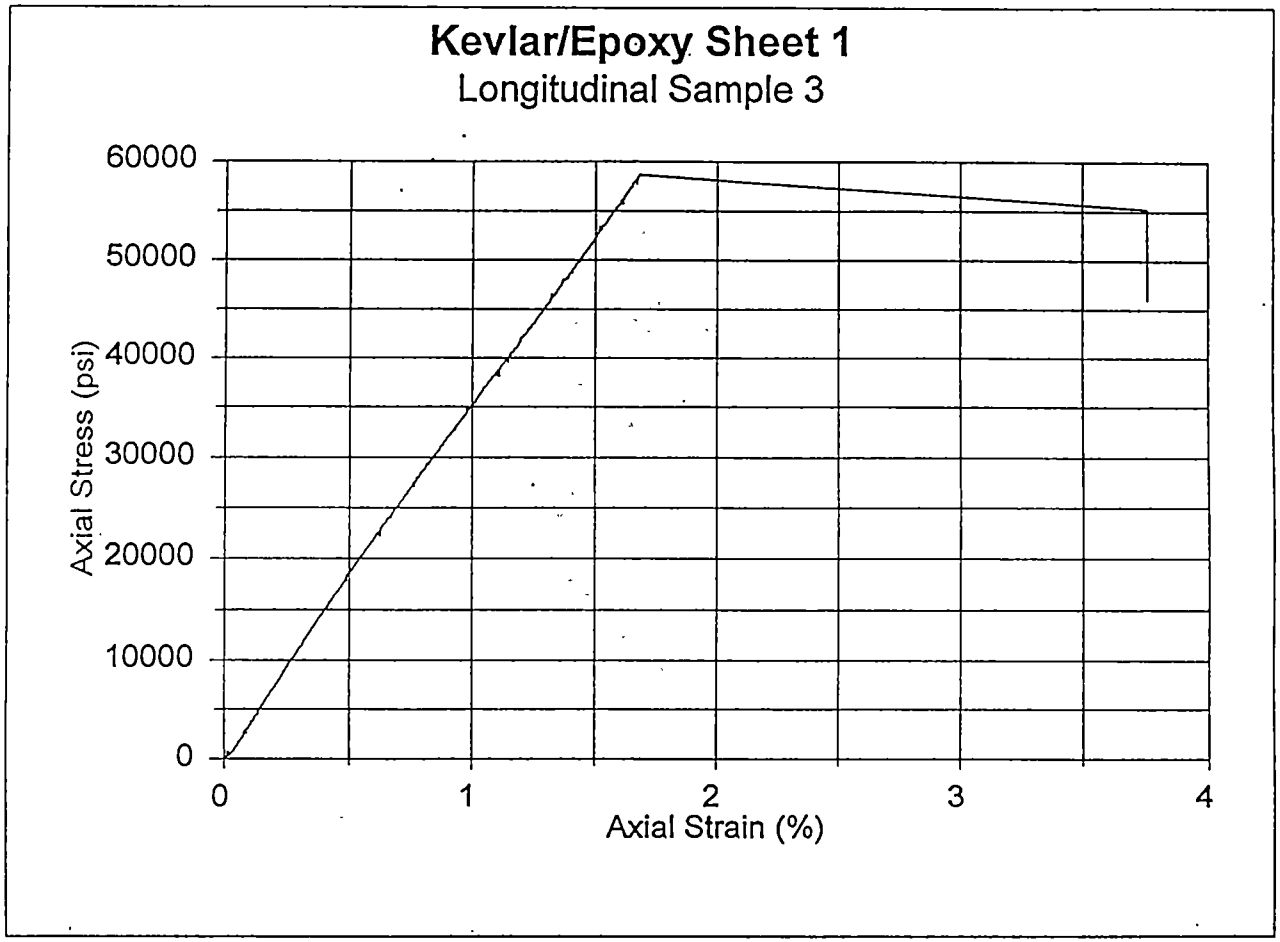


Figure 4.21 Representative kevlar/epoxy longitudinal stress-strain curve.

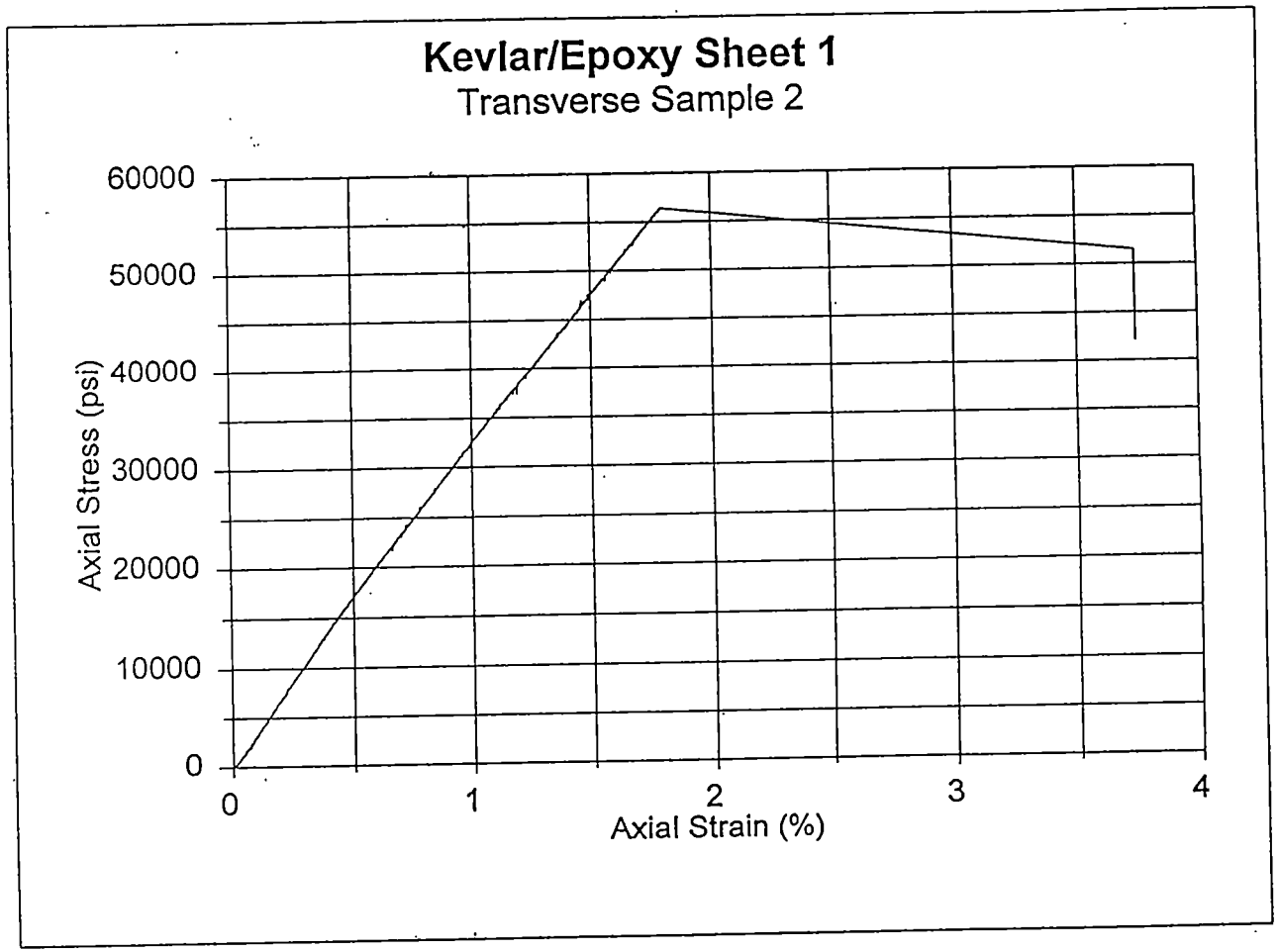


Figure 4.22 Representative kevlar/epoxy transverse stress-strain curve.

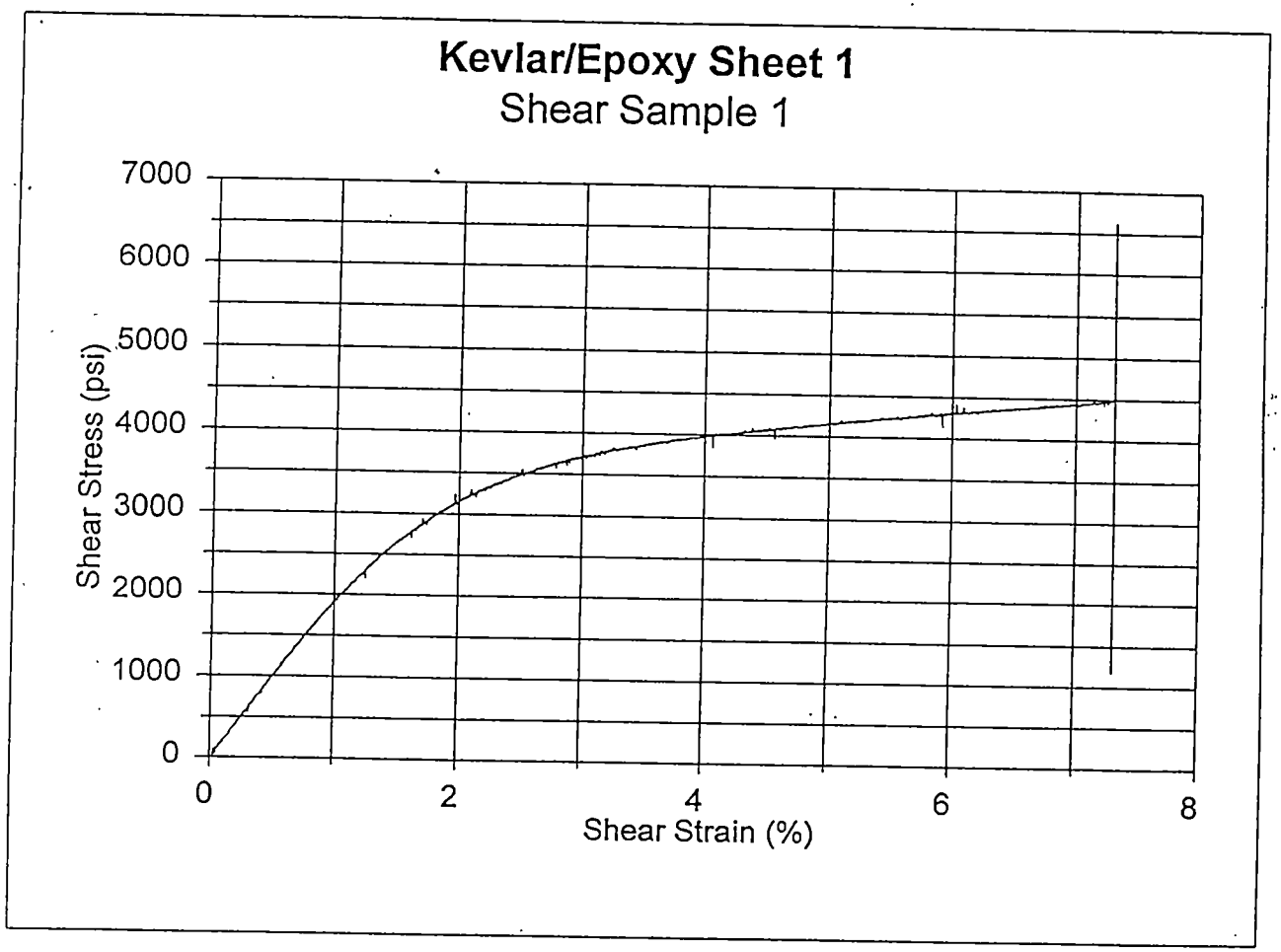


Figure 4.23 Representative kevlar/epoxy shear stress-strain curve.

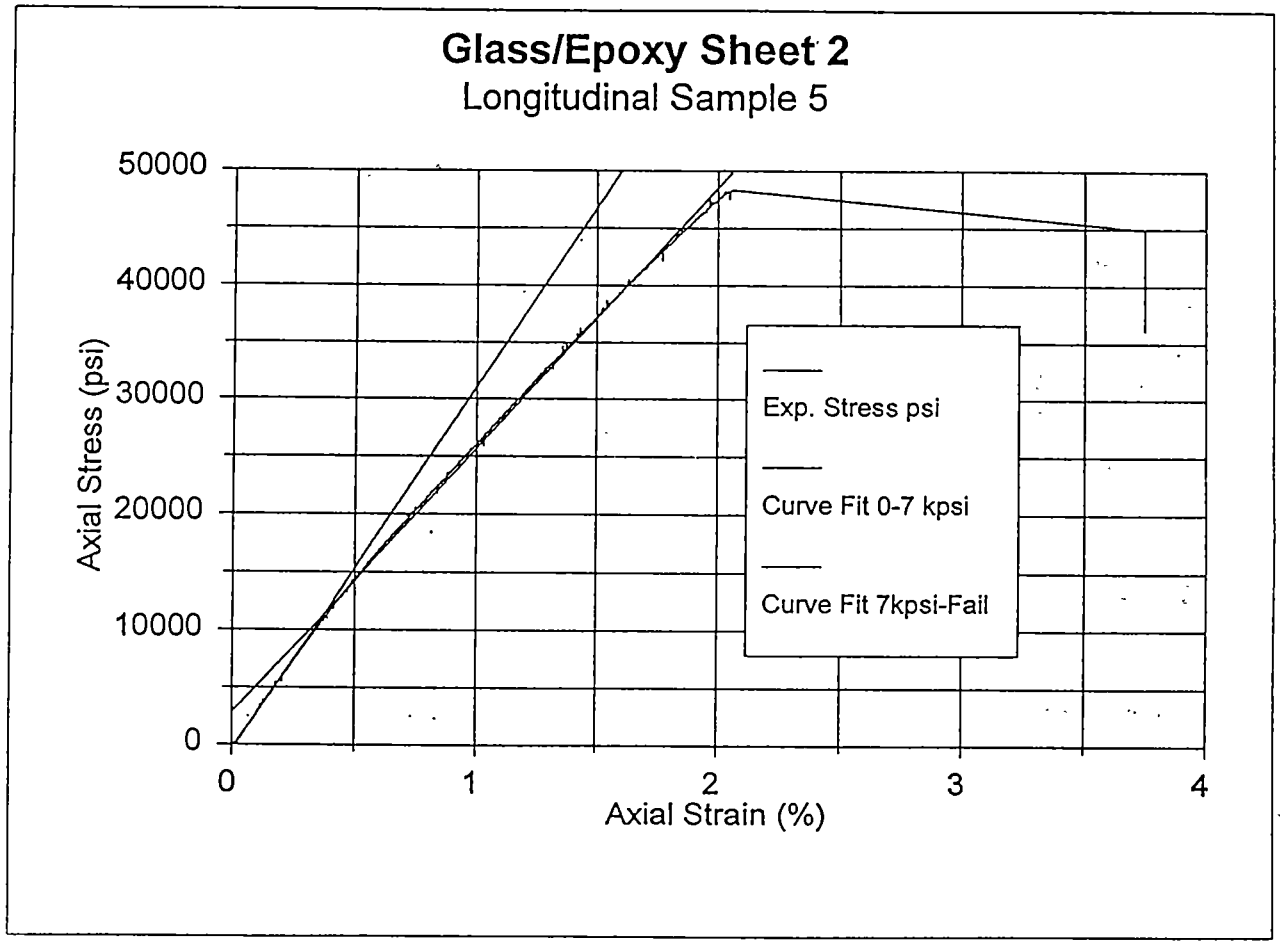


Figure 4.24 Glass/epoxy stress-strain curve fit highlighting change in slope.

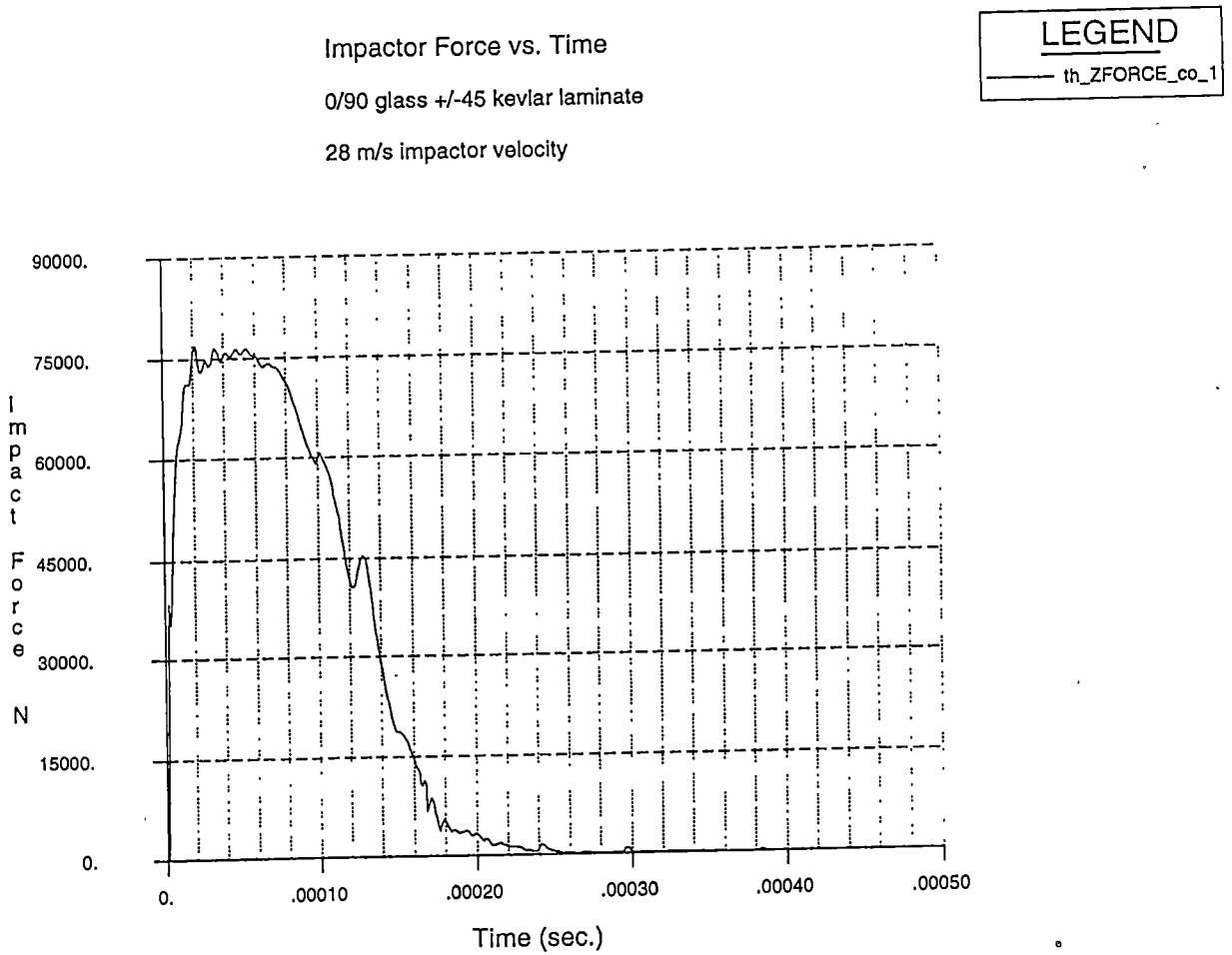


Figure 5.1 Impact force time history of planar geometry specimen.

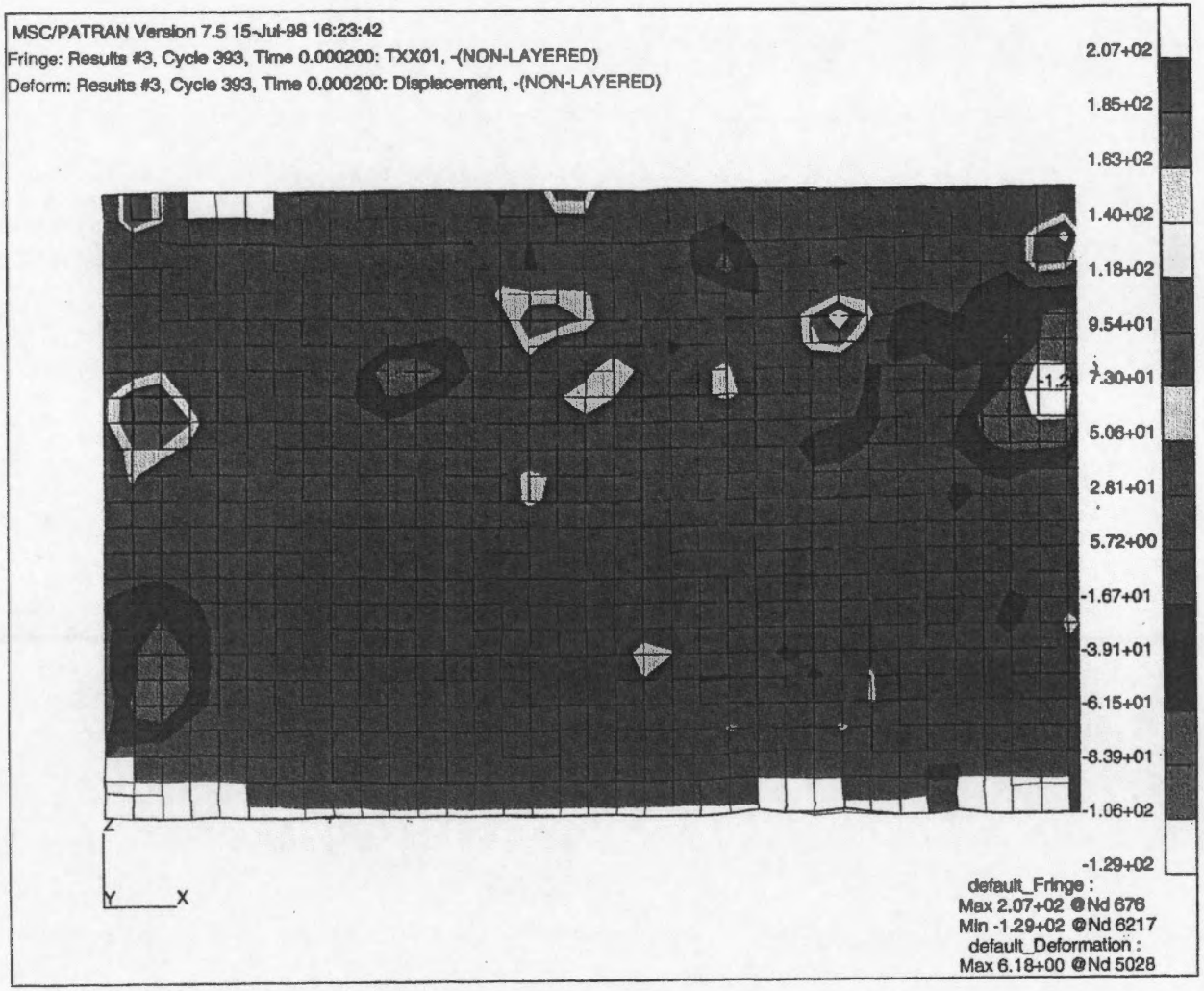


Figure 5.2 Kevlar lamina stress distribution at .2 ms for planar geometry specimen.

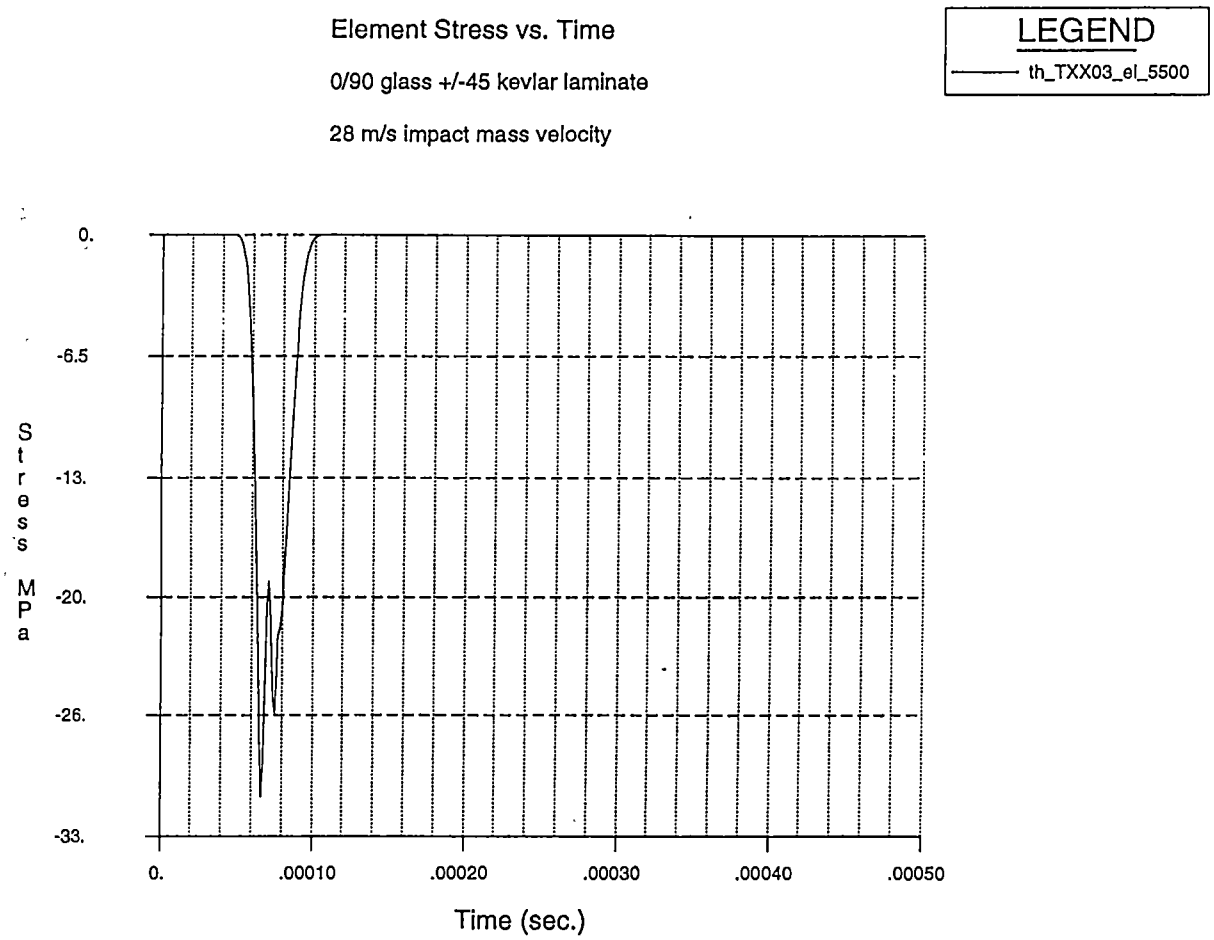


Figure 5.3 Stress time history of element at support platen interface for planar geometry specimen.

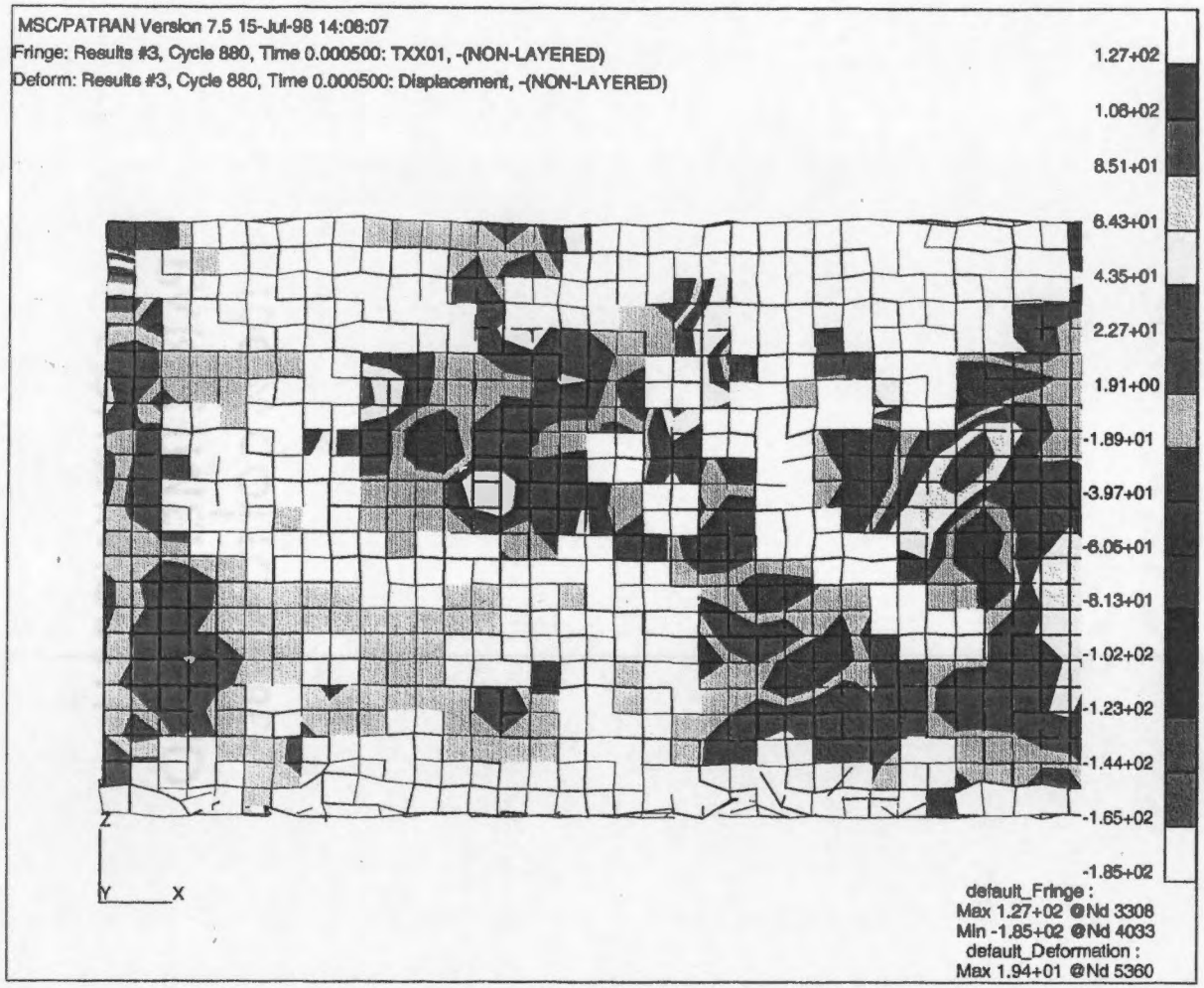


Figure 5.4. Kevlar lamina stress distribution at .5 ms for planar geometry specimen.

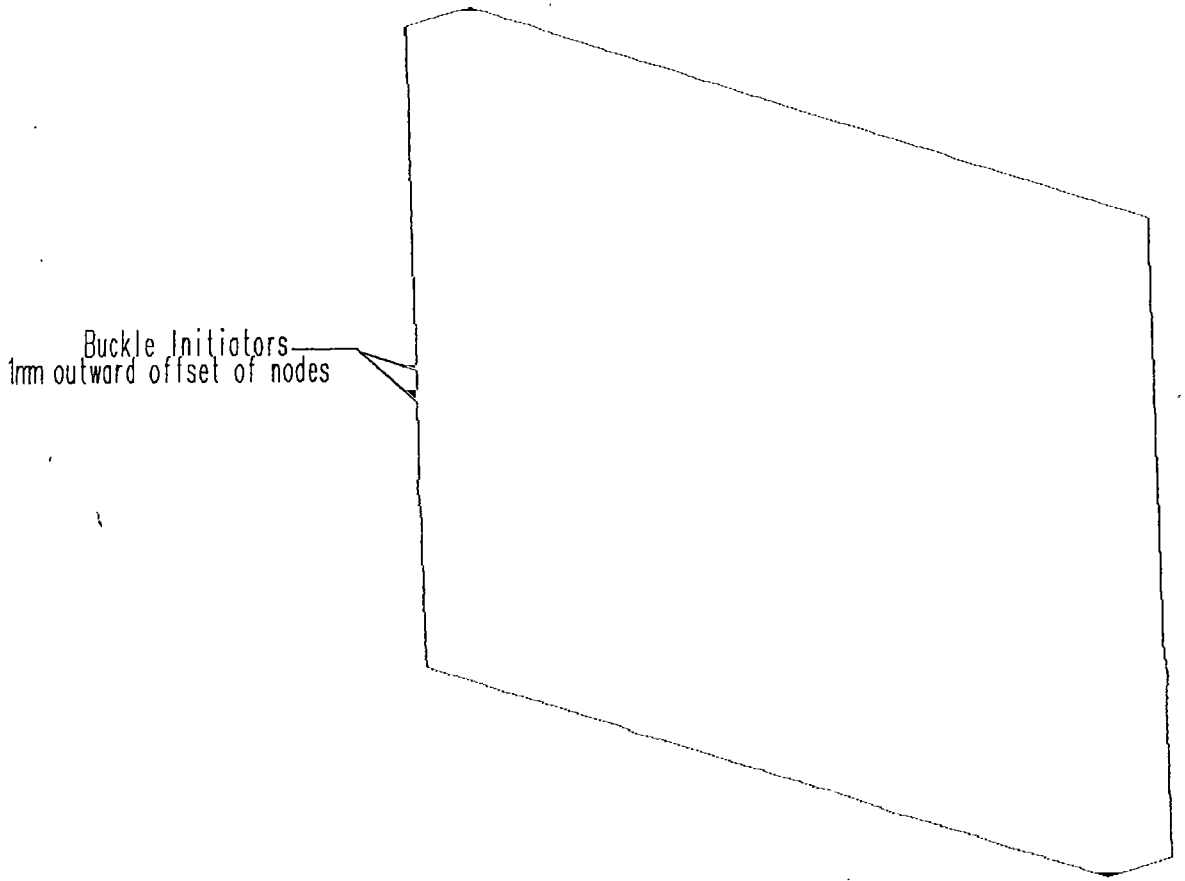


Figure 5.5 Perturbations in specimen sides.

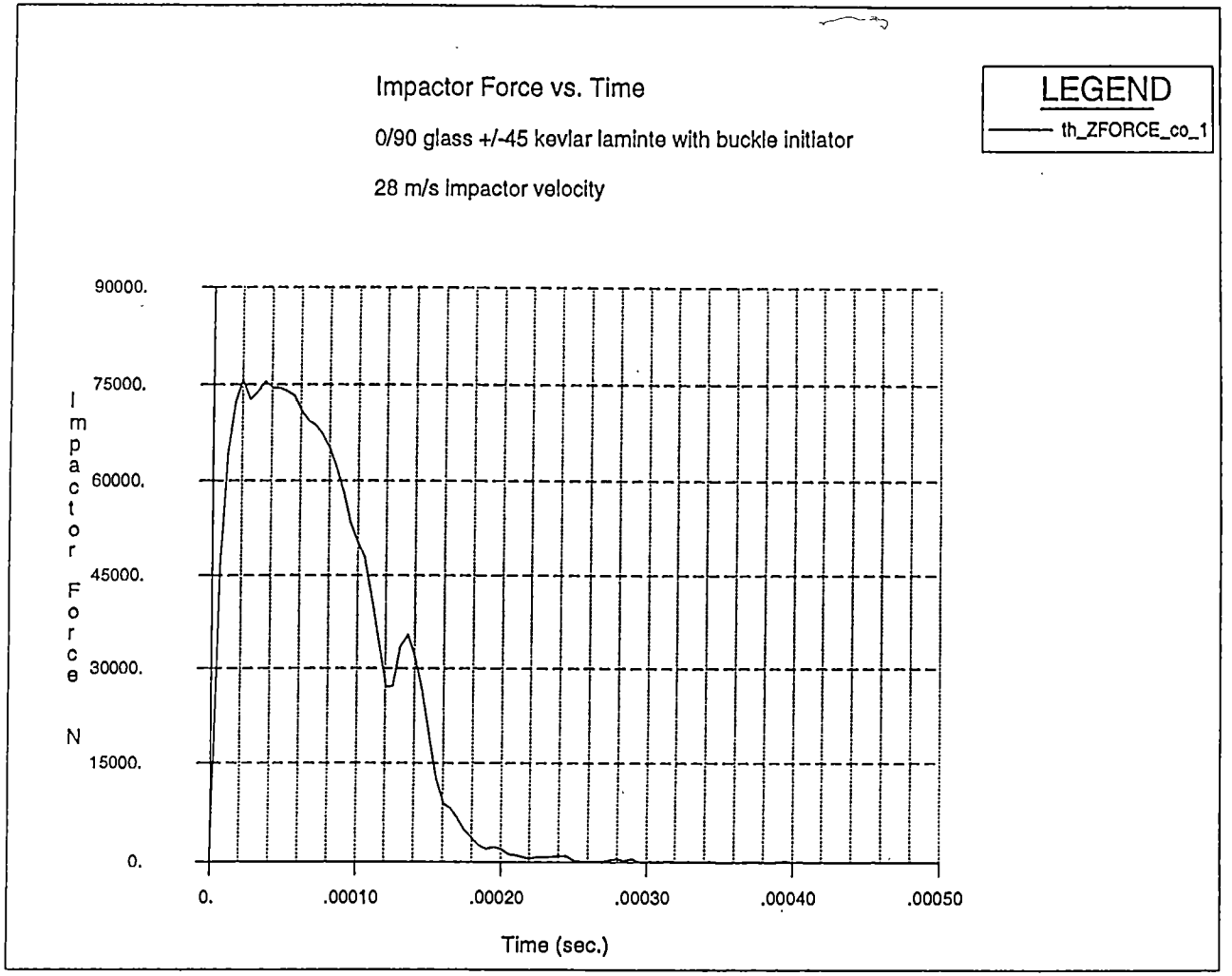


Figure 5.6 Impact force time history of perturbed geometry specimen.

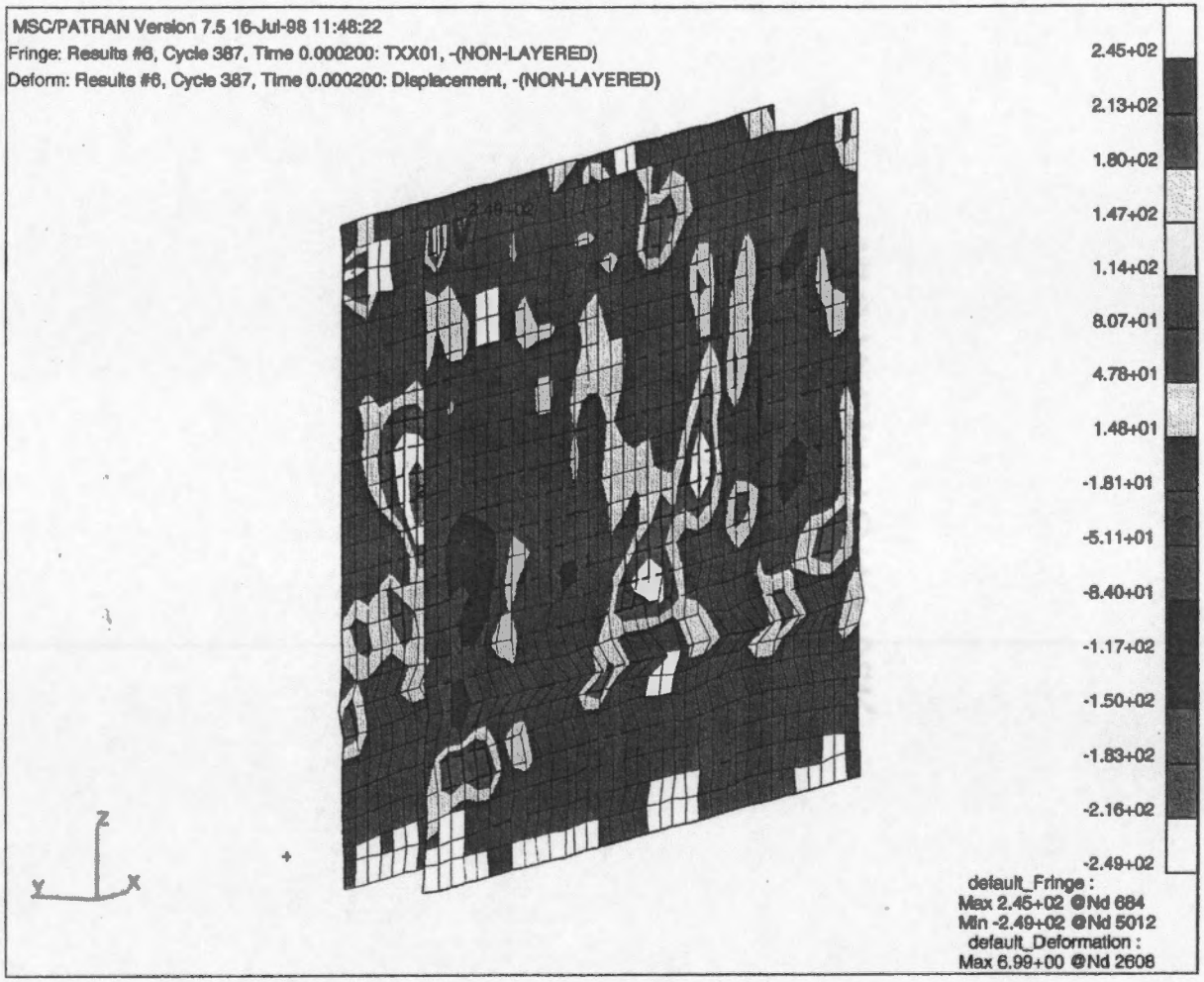


Figure 5.7 Kevlar lamina stress distribution at .2 ms for perturbed geometry specimen.

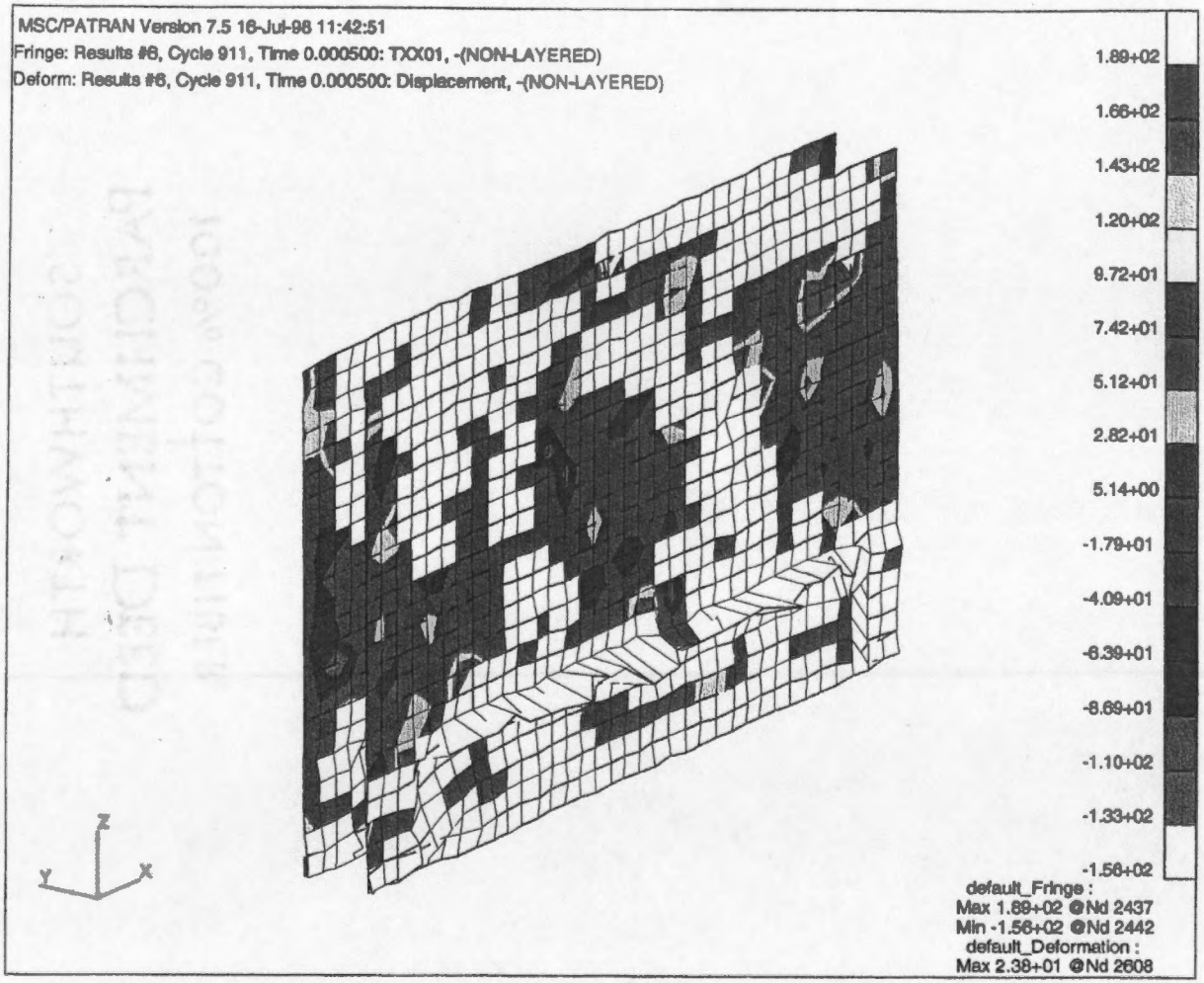


Figure 5.8 Kevlar lamina stress distribution at .5 ms for perturbed geometry specimen.

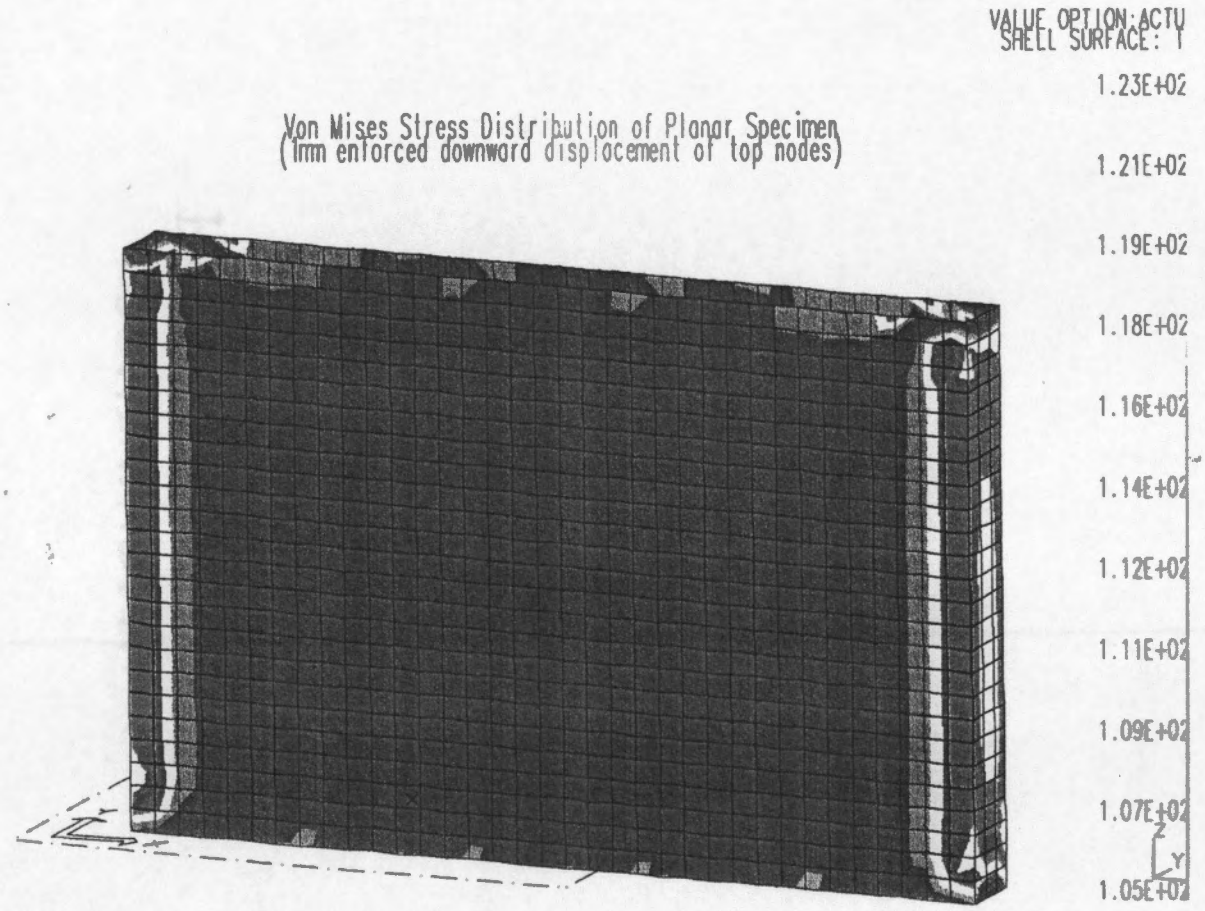


Figure 5.9 Static stress distribution of planar geometry specimen.

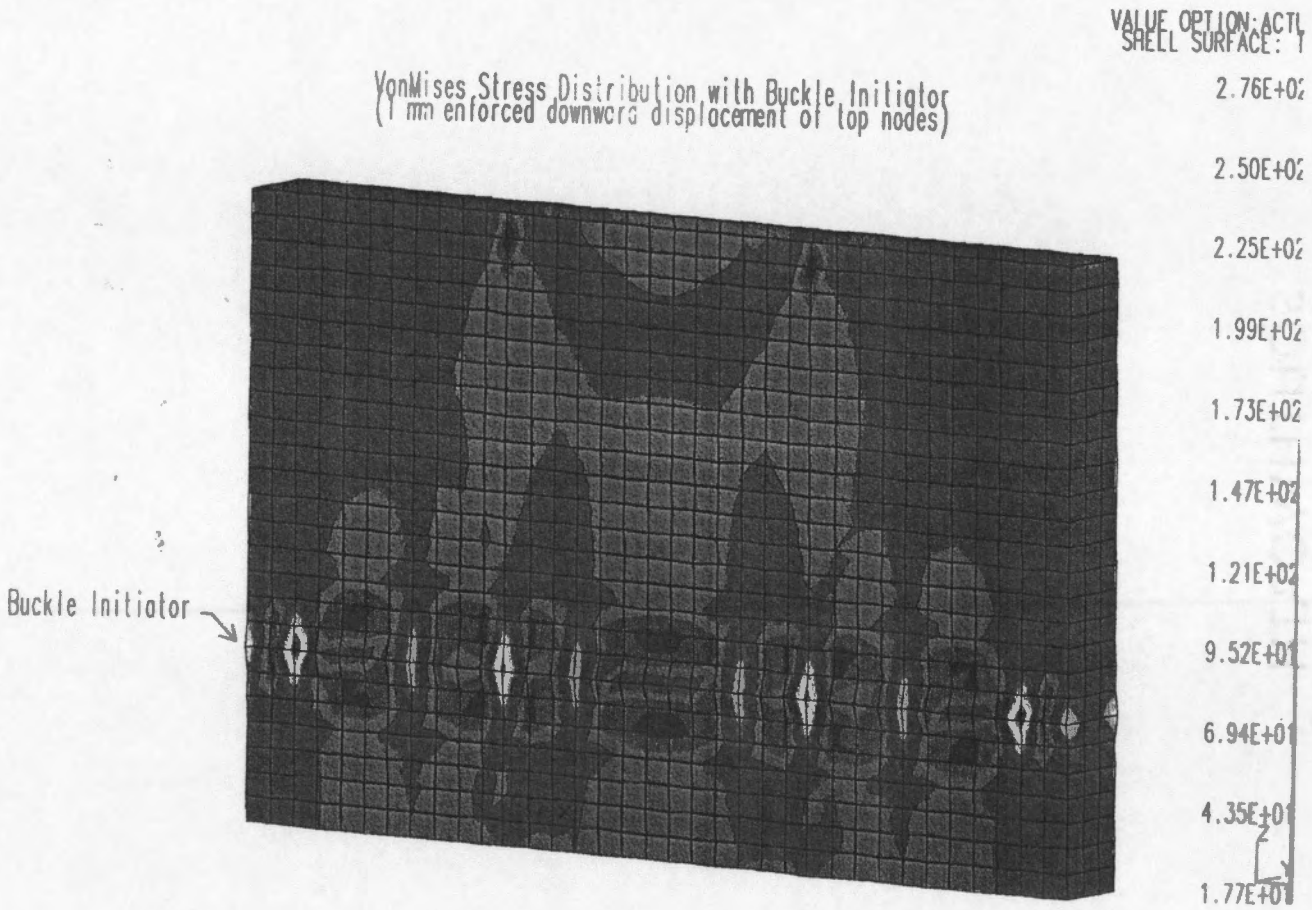


Figure 5.10 Static stress distribution of perturbed geometry specimen.

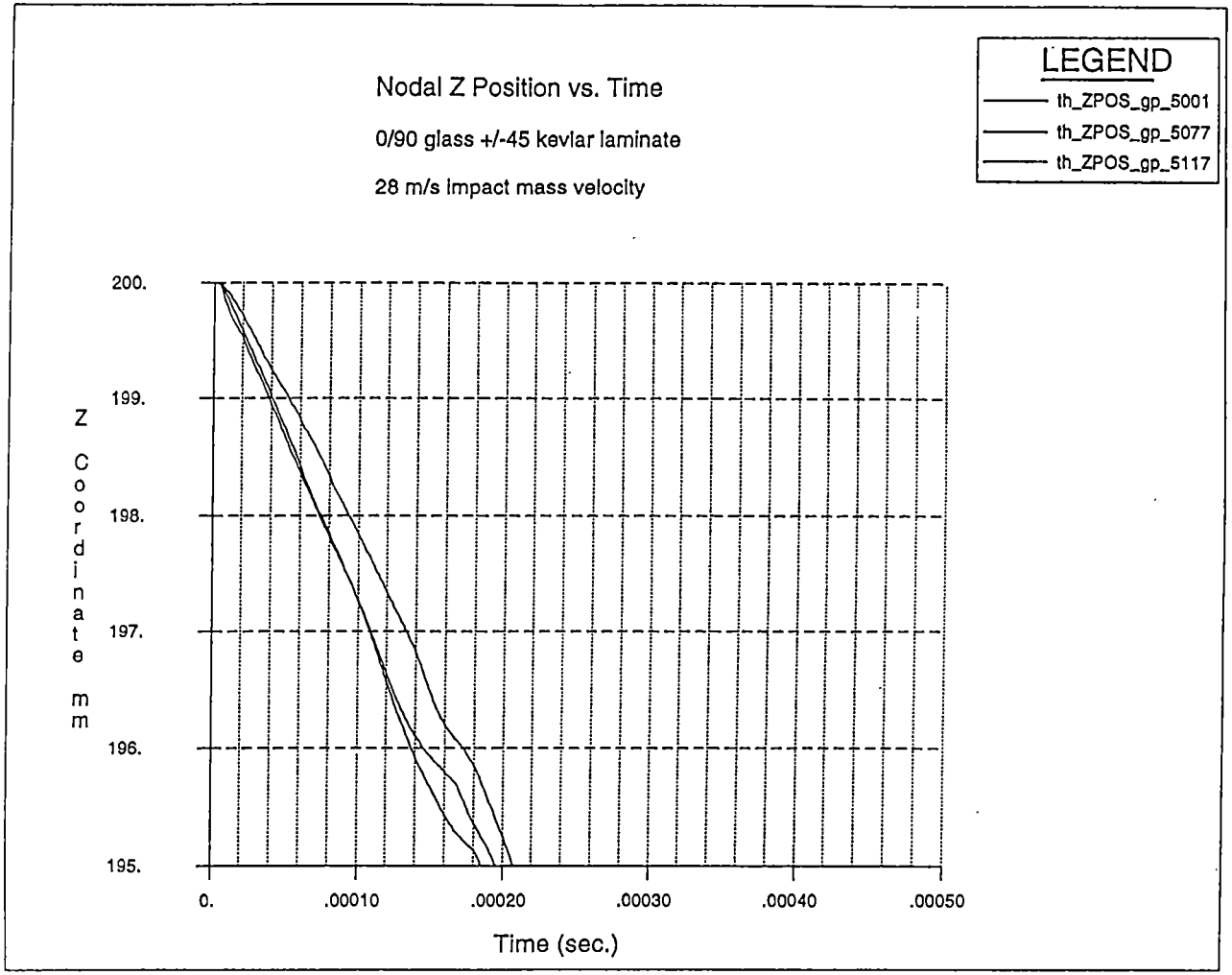


Figure 5.11 Nodal position time history of planar geometry specimen.

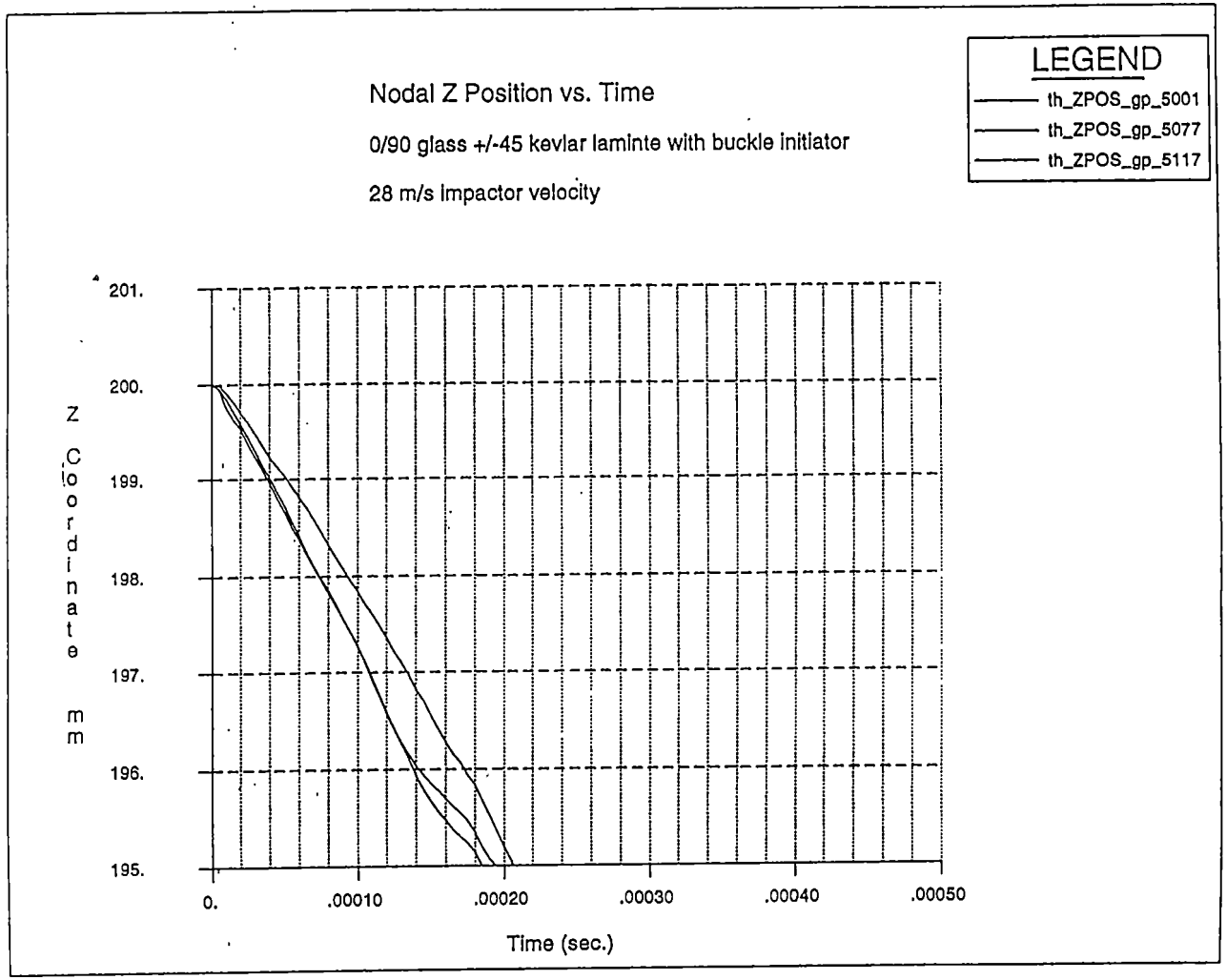


Figure 5.12 Nodal position time history of perturbed geometry specimen.

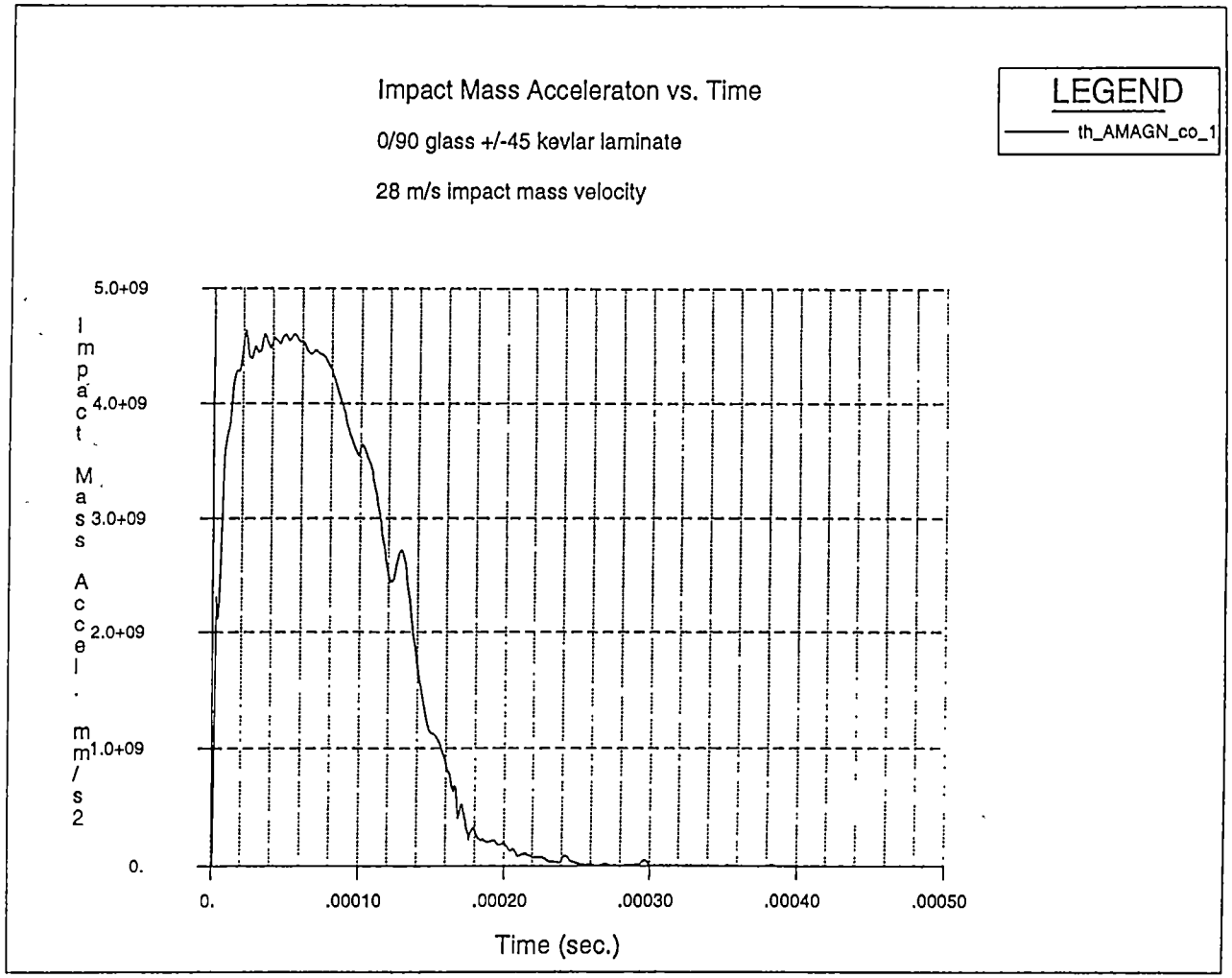


Figure 5.13 Impact mass acceleration time history of planar geometry specimen.

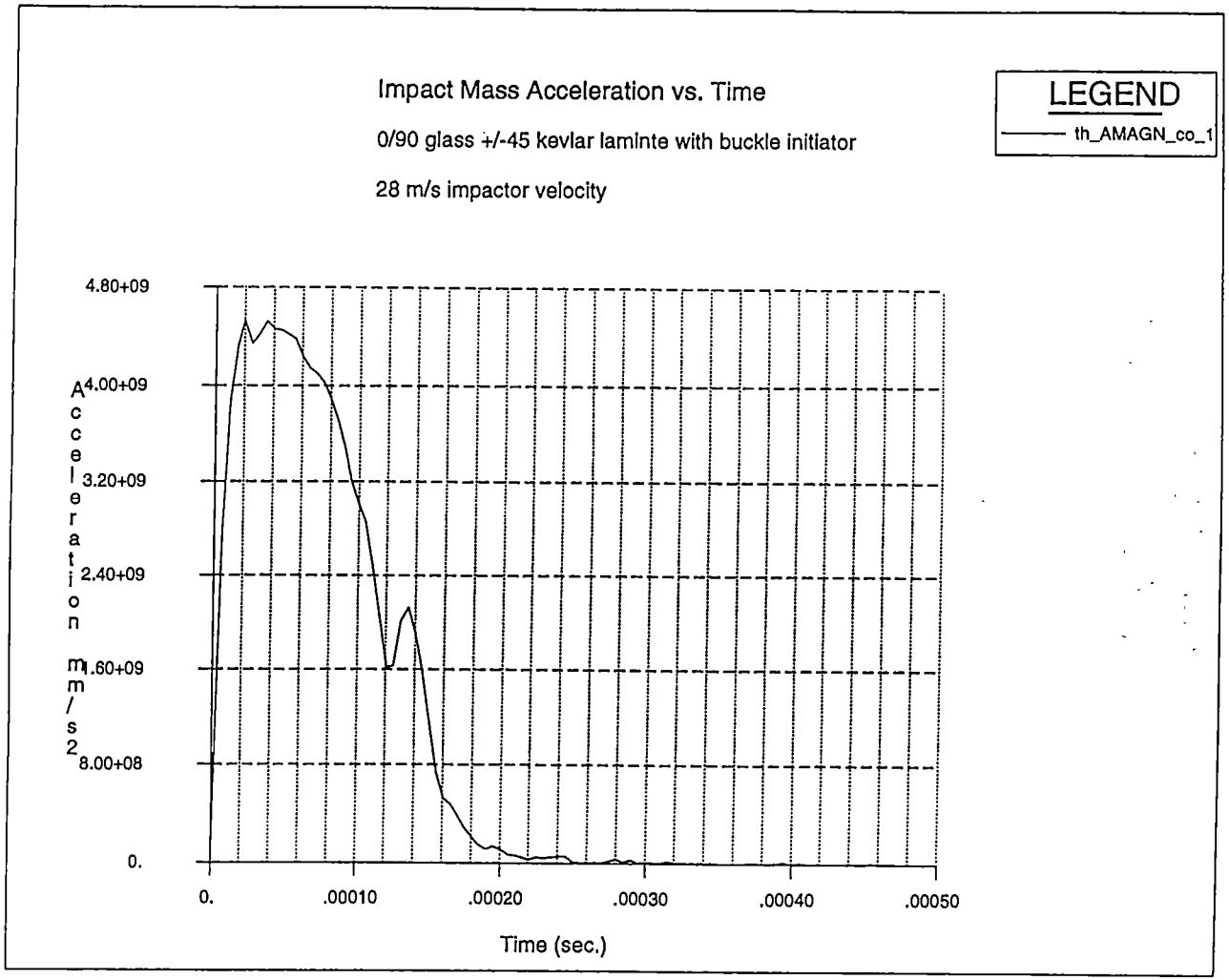
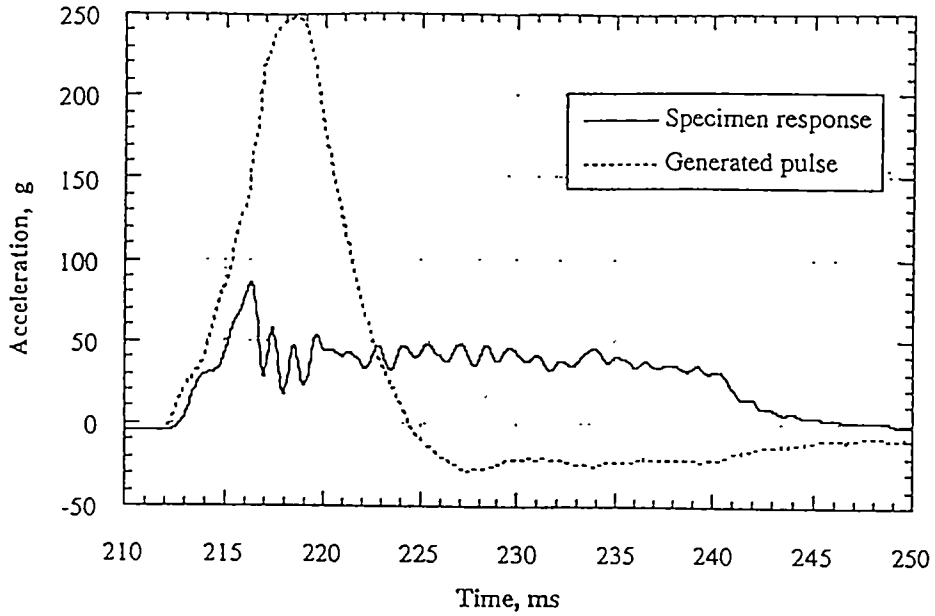


Figure 5.14 Impact mass acceleration time history of perturbed geometry specimen.



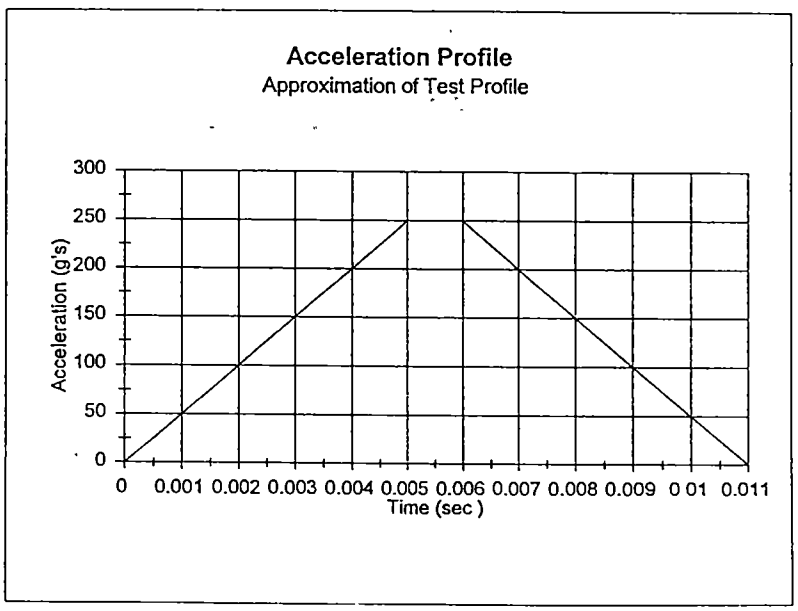


Figure 5.15 Test acceleration pulse and its approximation.

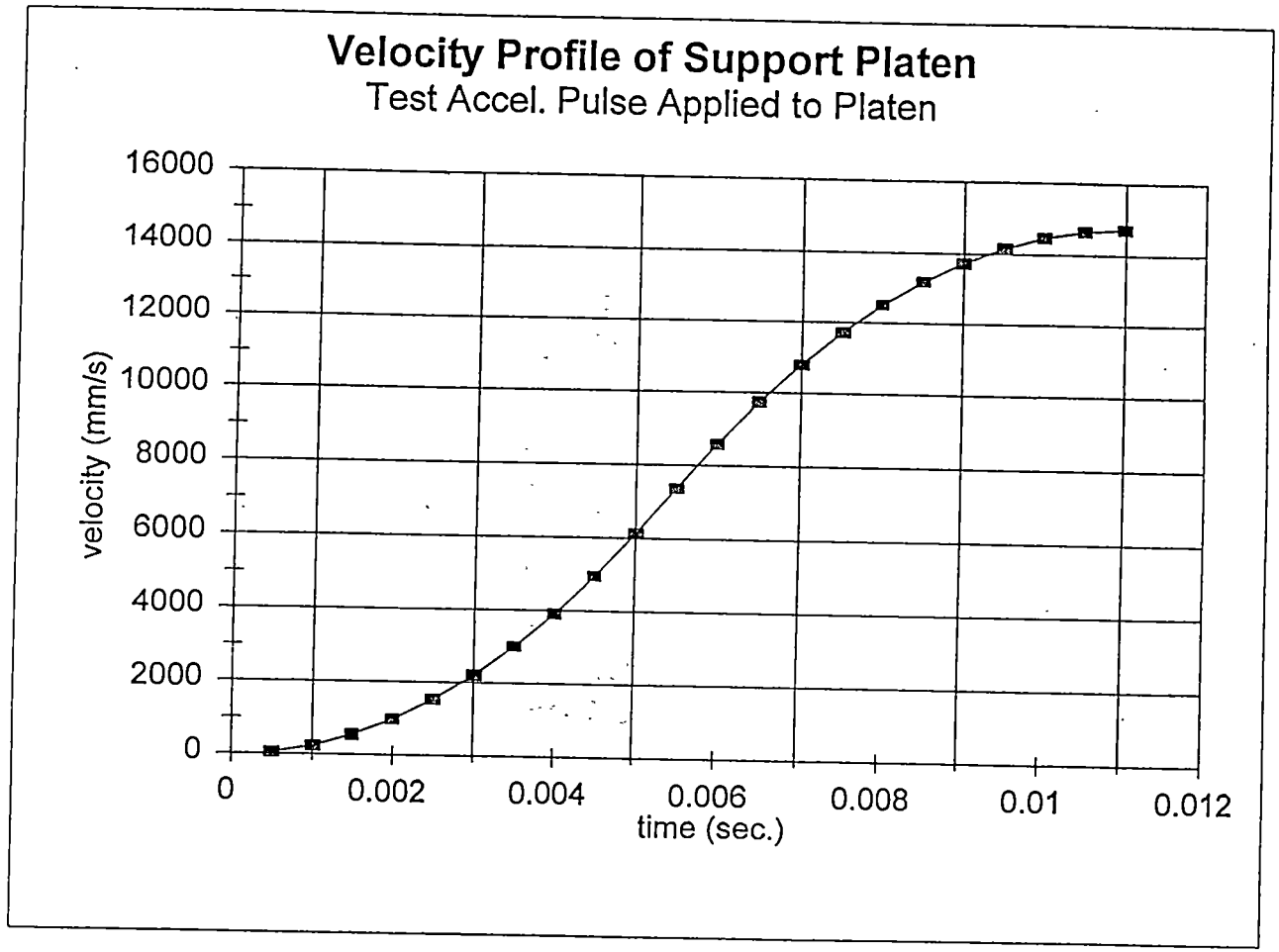


Figure 5.16 Velocity profile assigned to support platen.

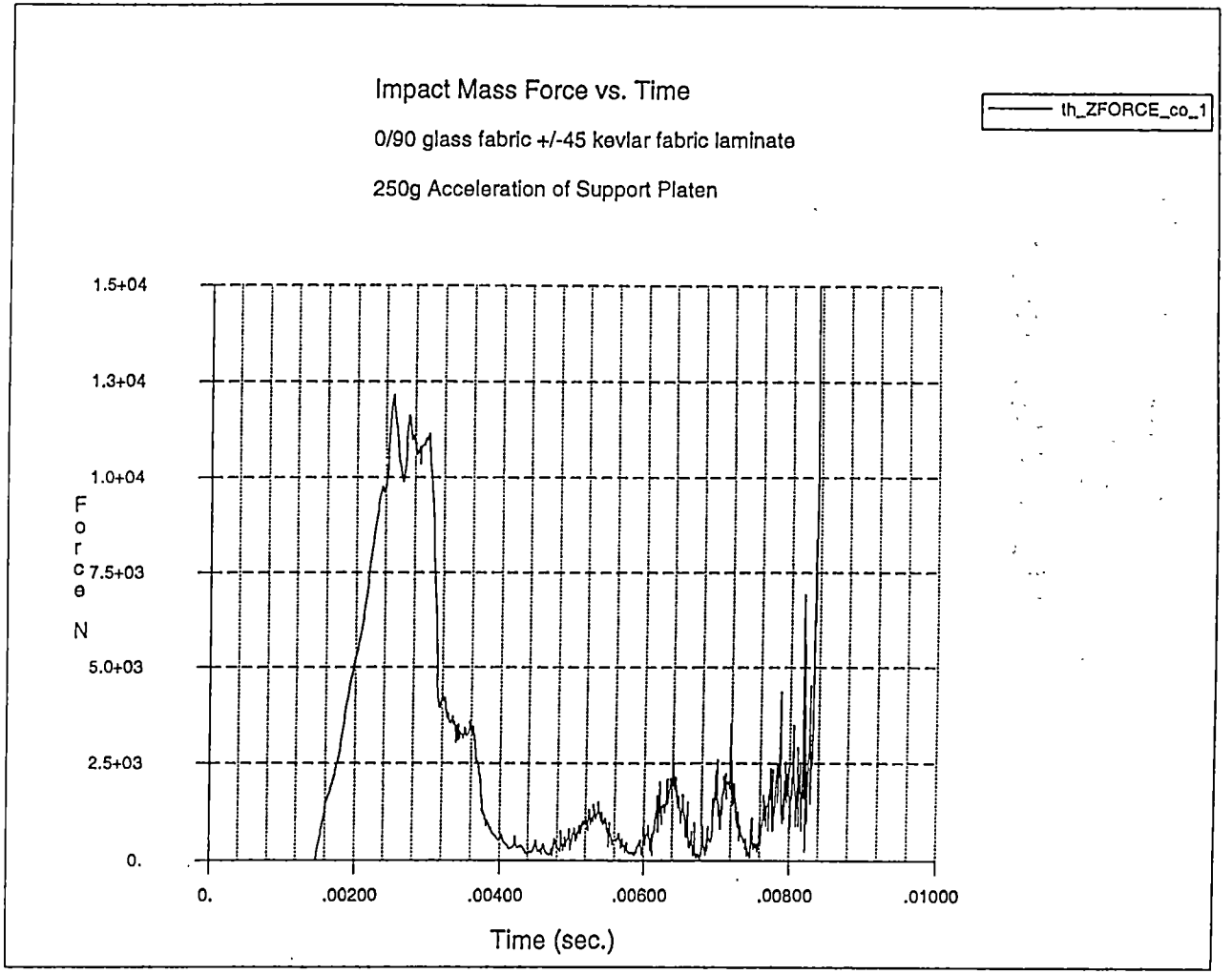


Figure 5.17 Impact force time history of planar specimen with base acceleration.

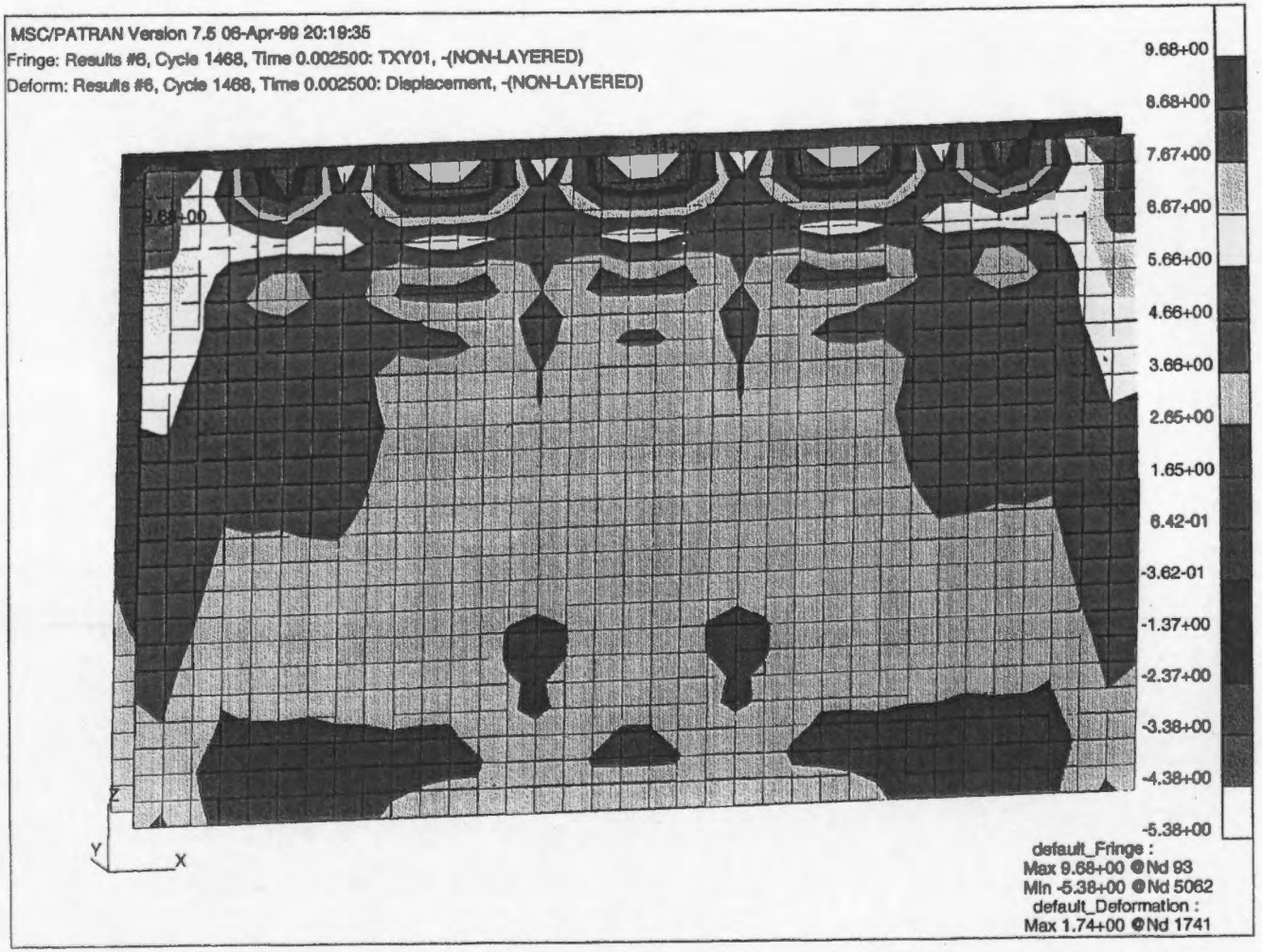


Figure 5.18 Kevlar lamina stress distribution at 2.5 ms for planar geometry specimen with base acceleration.

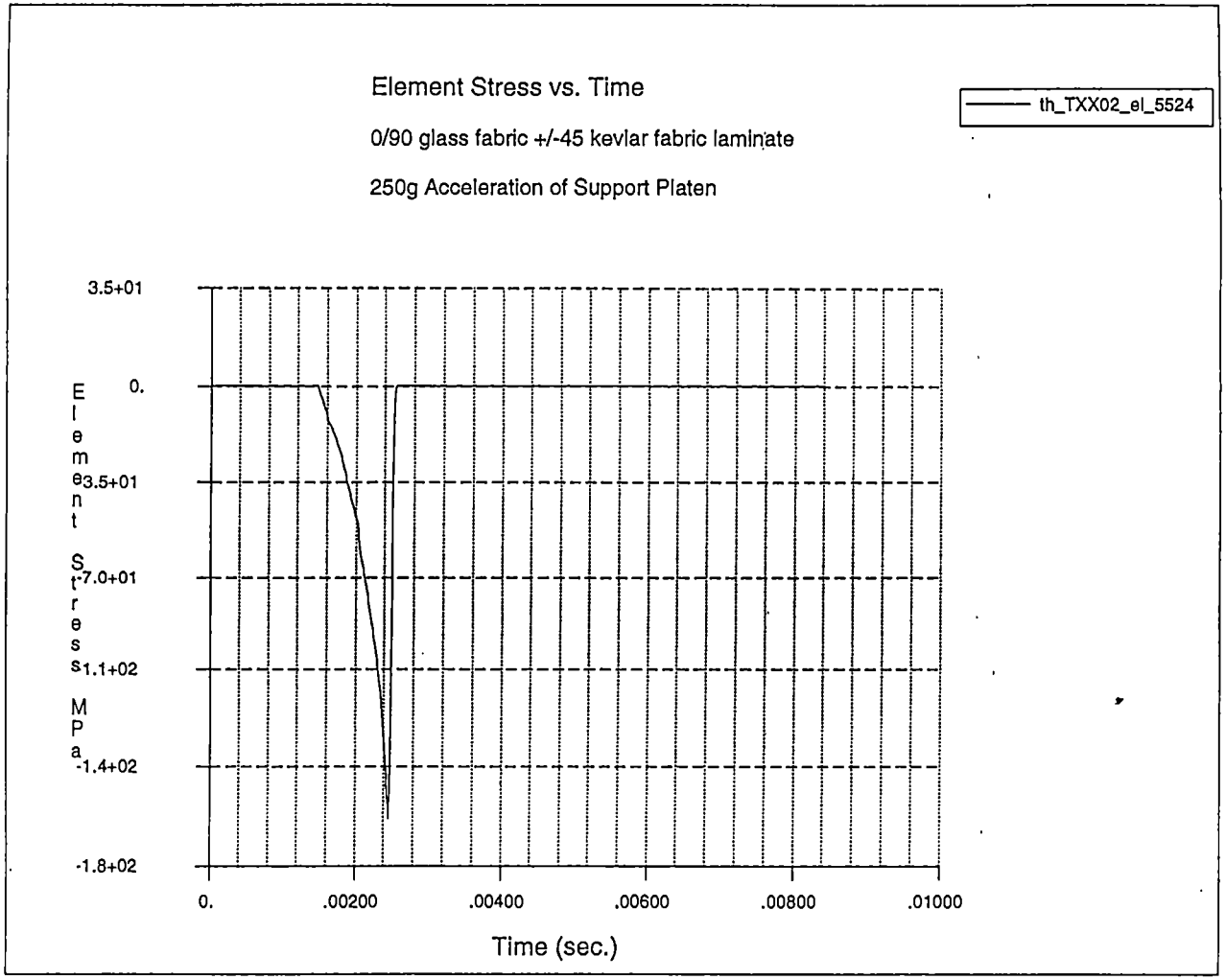


Figure 5.19 Stress time history of element at impact mass interface for planar geometry specimen with base acceleration.

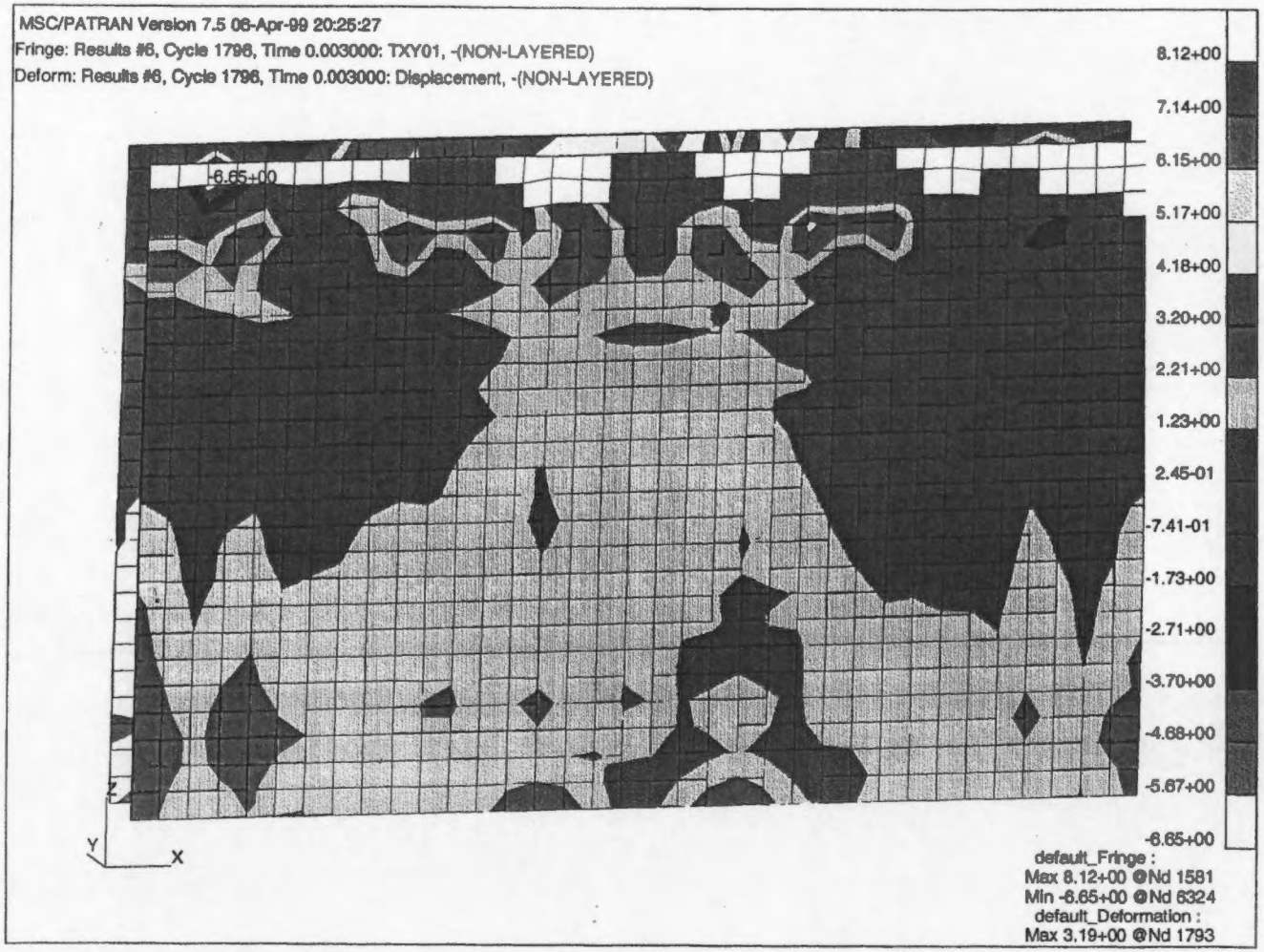


Figure 5.20 Kevlar lamina stress distribution at 3 ms for planar geometry specimen with base acceleration.

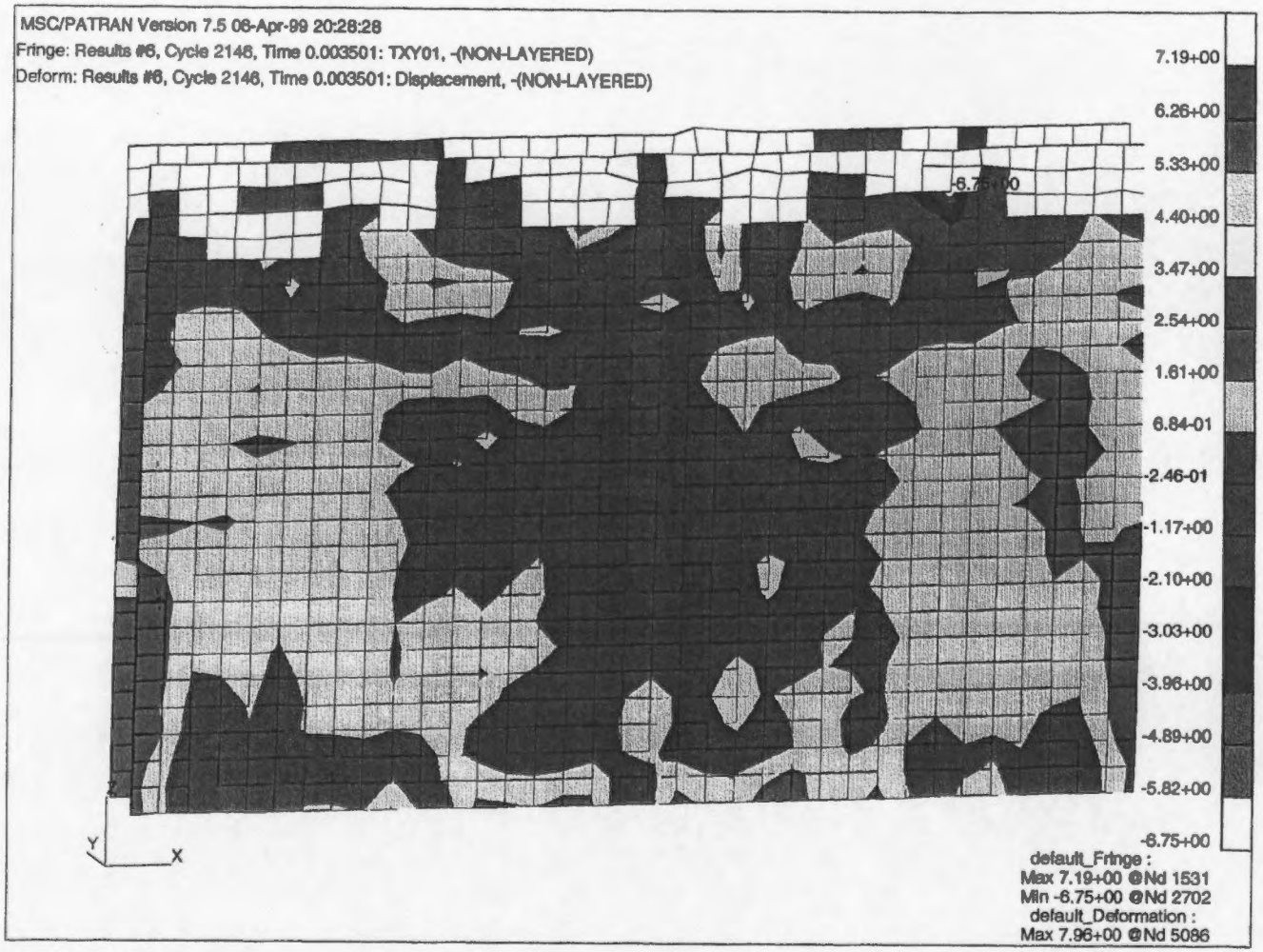


Figure 5.21 Kevlar lamina stress distribution at 3.5 ms for for planar geometry specimen with base acceleration.

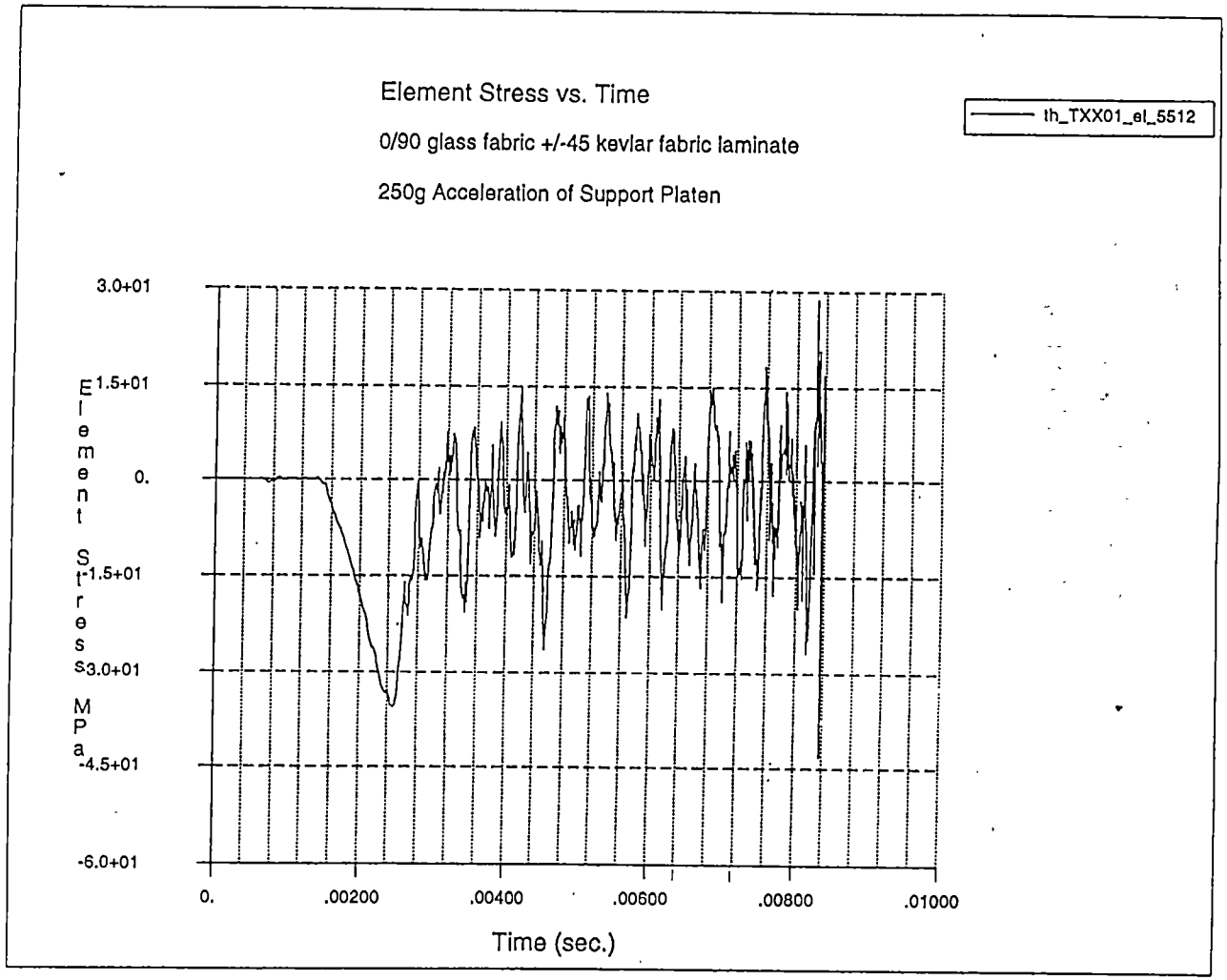


Figure 5.22 Stress time history of element in mid-section of planar geometry specimen with base acceleration.

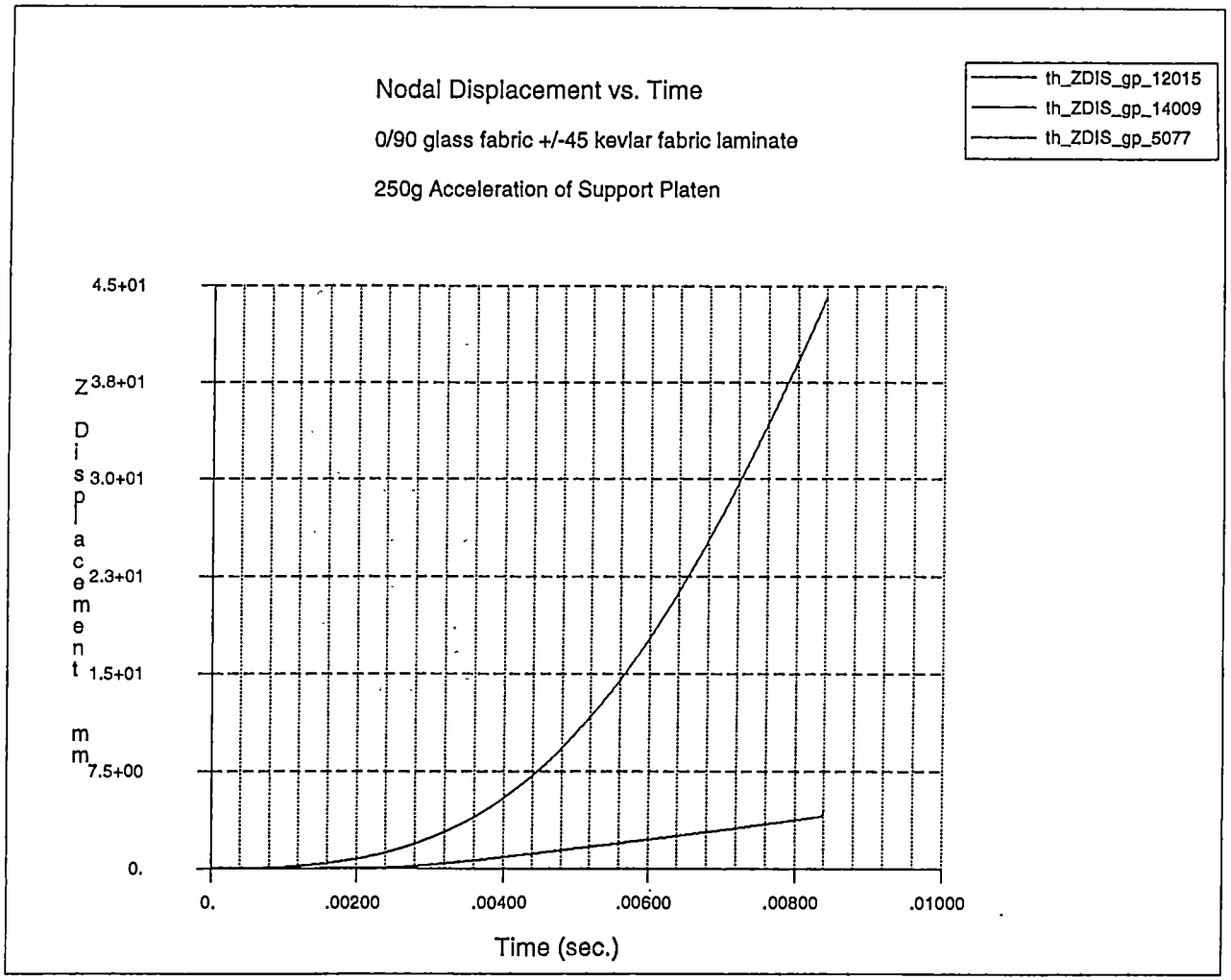


Figure 5.23 Displacement time history of support platen and impact mass of planar geometry specimen with base acceleration.

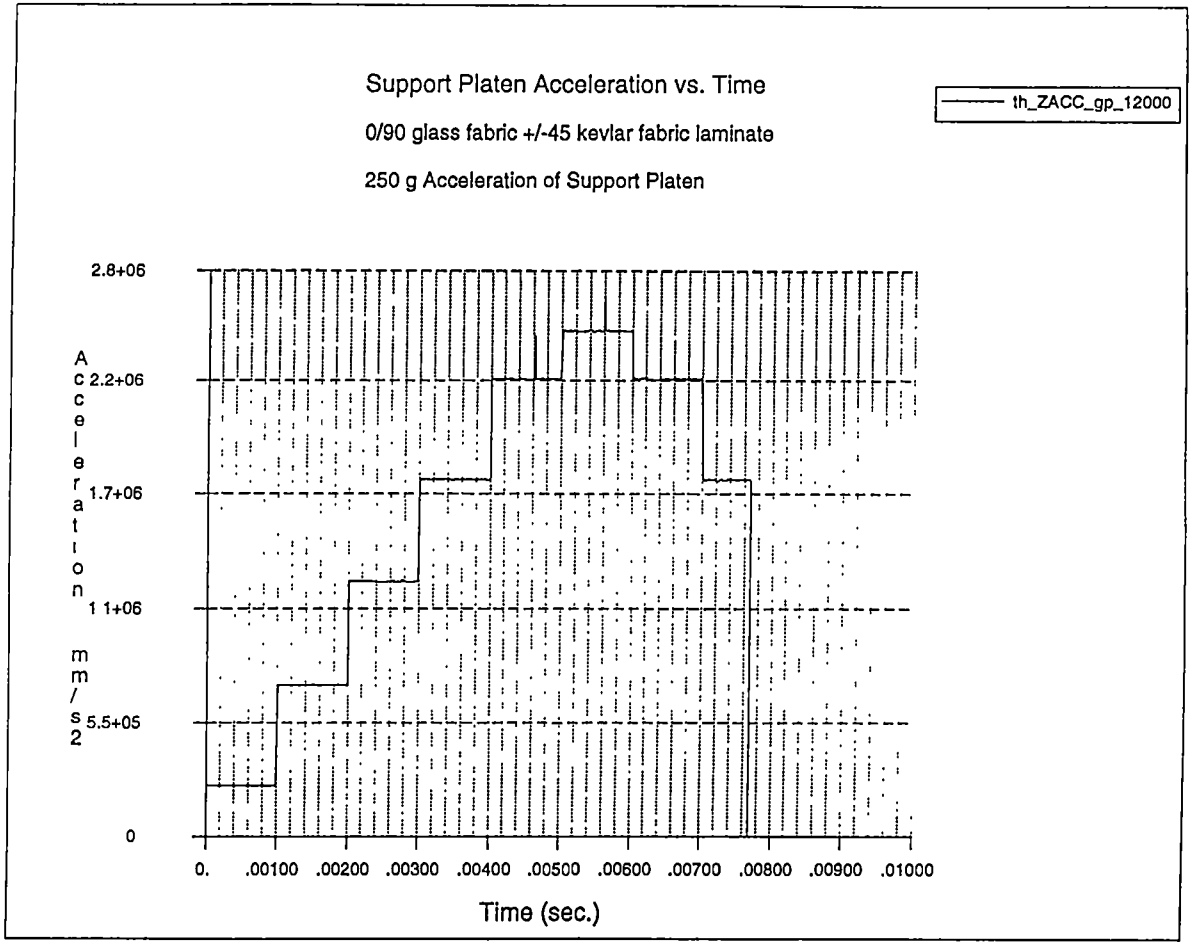


Figure 5.24 Support platen acceleration time history for base acceleration.

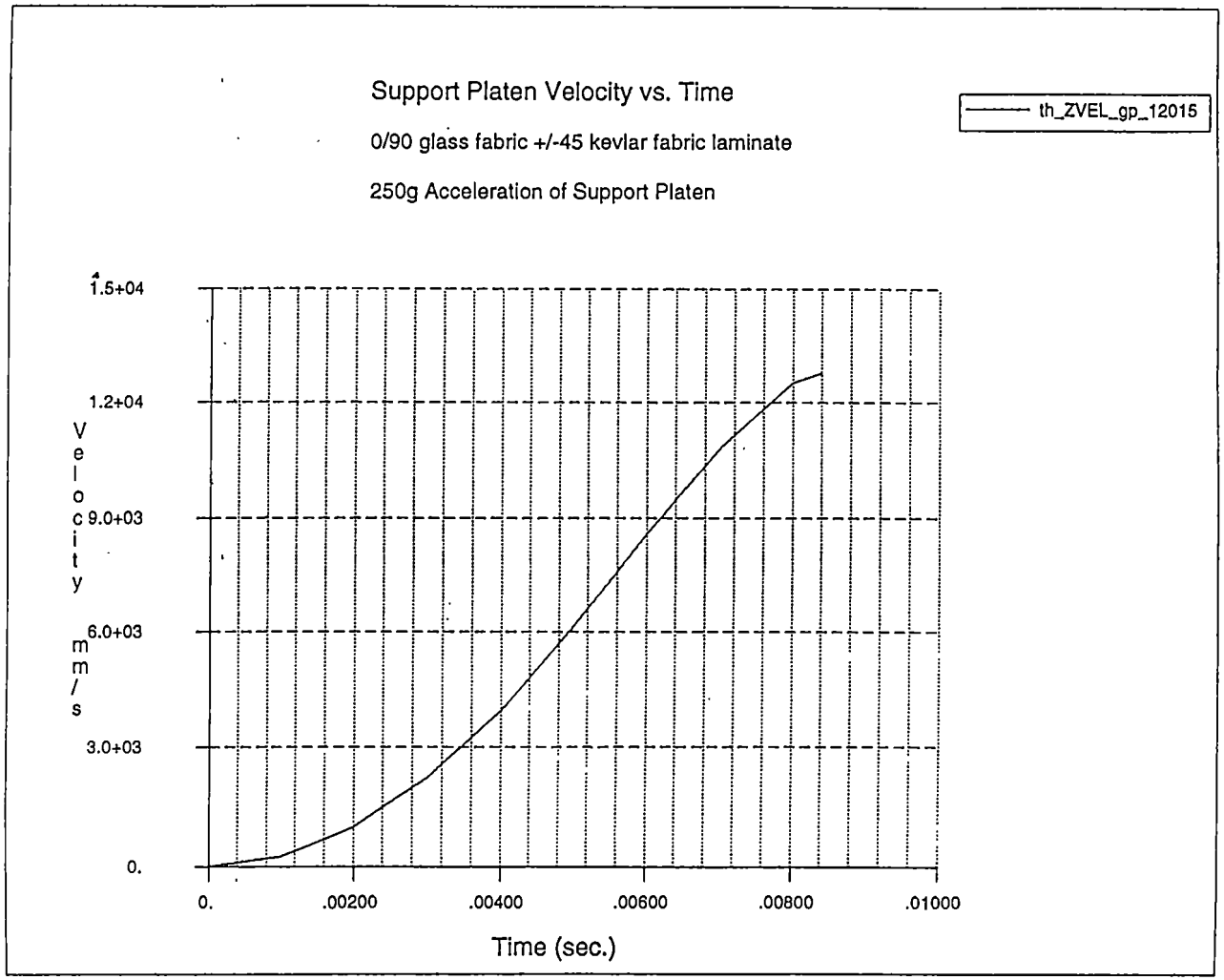


Figure 5.25 Support platen velocity time history for base acceleration.

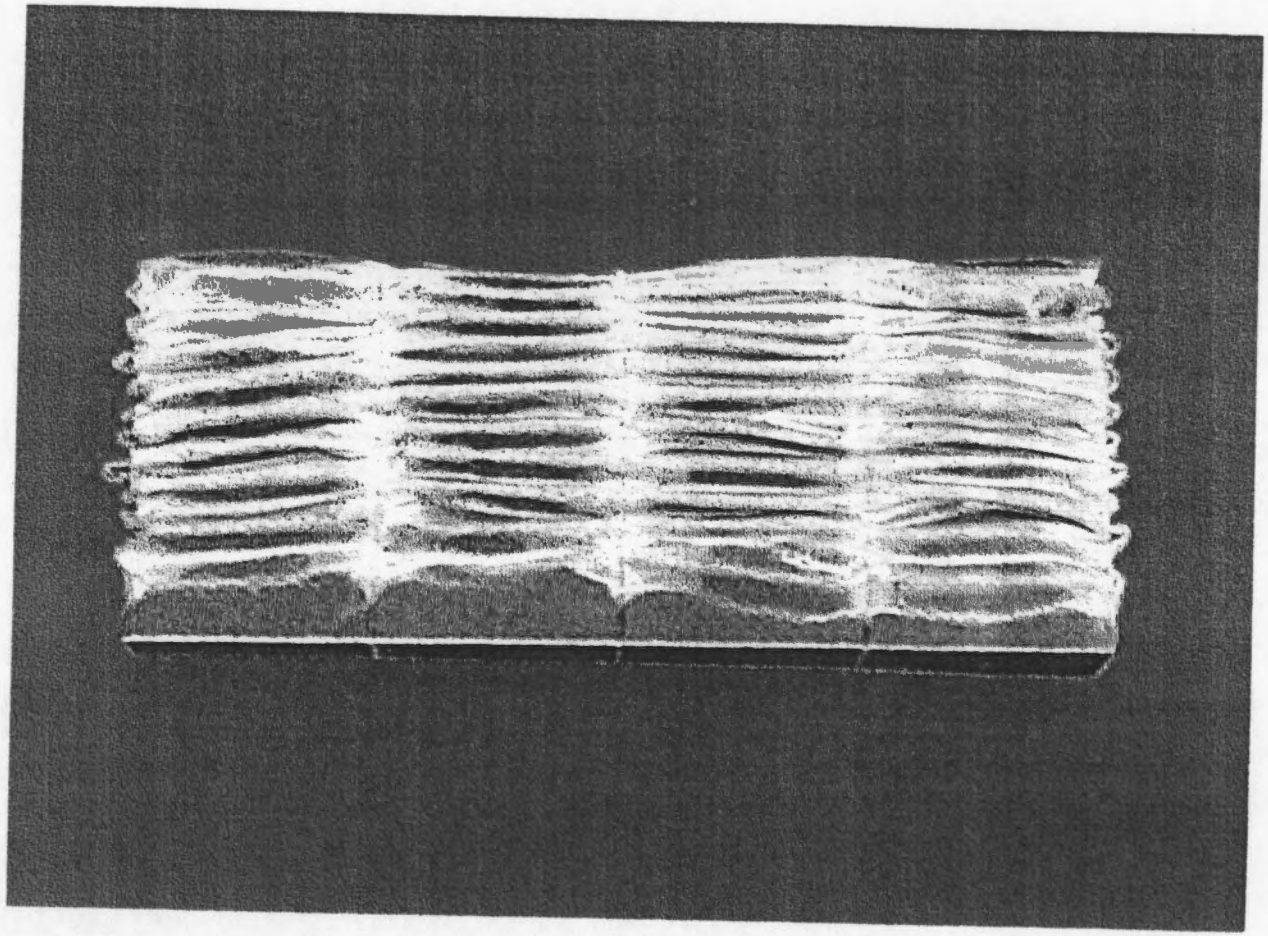


Figure 5.26 Test specimen crushing pattern.

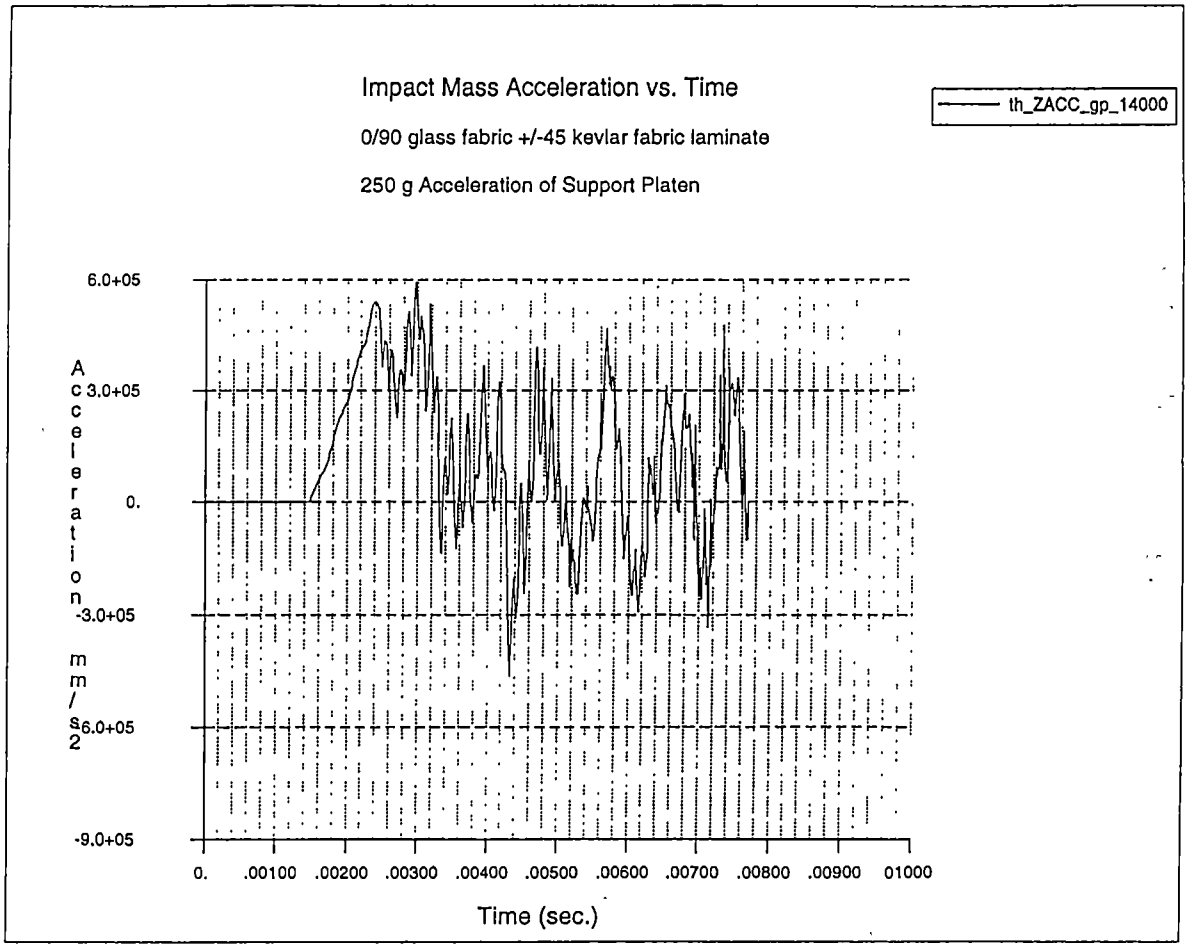


Figure 5.27 Impact mass acceleration time history for planar geometry with base acceleration.

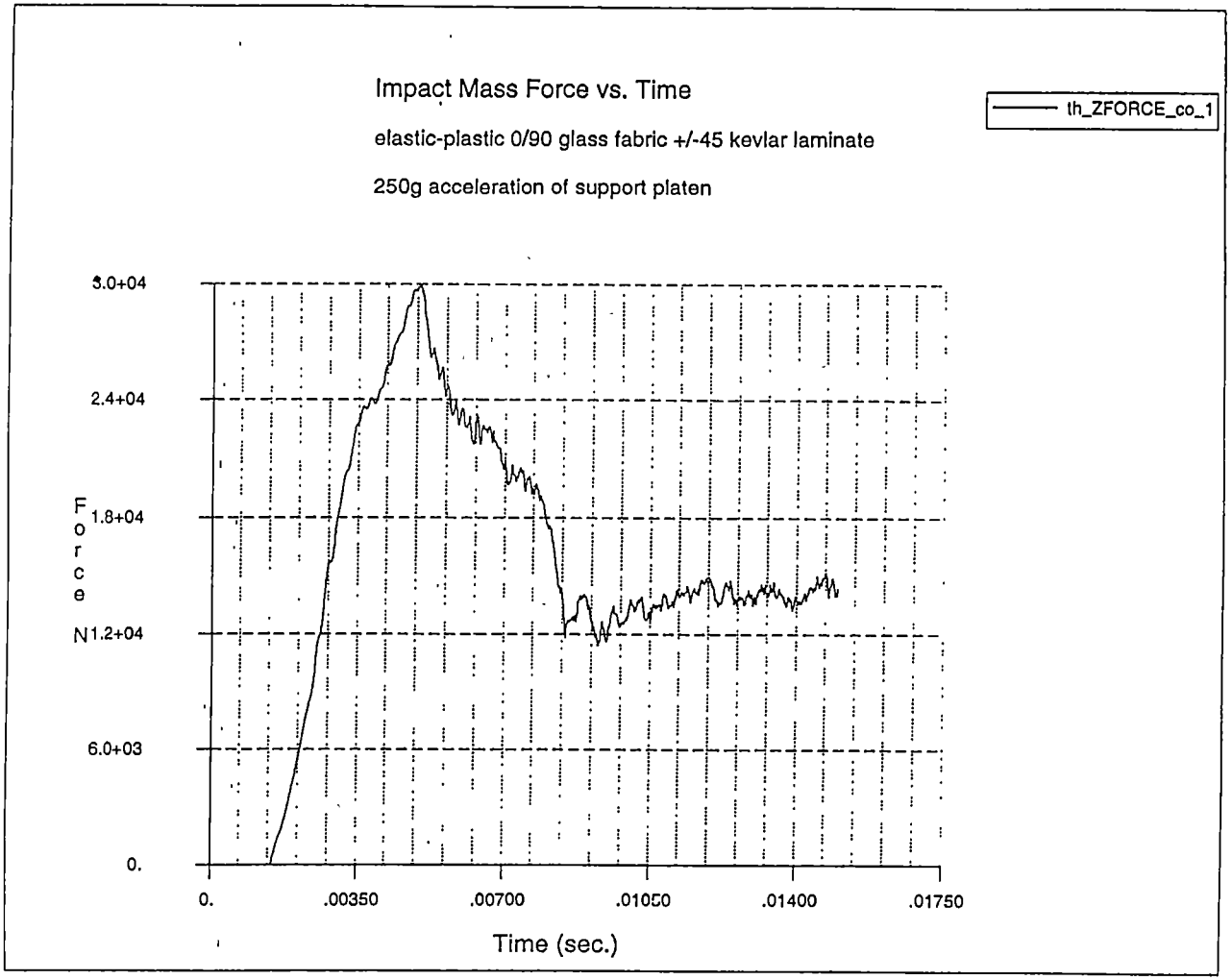


Figure 5.28 Impact force time history for specimen with elastic-plastic lamina, planar geometry and base acceleration

VITA

Brett Starr was born in Greensboro, North Carolina on January 30, 1961. He attended schools in the public school system of Guilford County, North Carolina, where he graduated from Southeast Guilford High School in June, 1979. He entered North Carolina State University at Raleigh in August of 1979. In May of 1984, he received the Bachelor of Science in Mechanical Engineering. He worked in industry with Volvo-GM Heavy Truck Corporation in Greensboro, North Carolina and attended graduate level classes at North Carolina Agricultural and Technological University from time to time. In January of 1997, he became a full-time student in the Master's Program at the University of Tennessee Space Institute working under a NASA Space Grant. He received a Master's degree in Engineering Science in May 1999.